Stony Brook University

Temporal fidelity and functional dynamics in functional MRI time-series analyses

A Dissertation Presented

by

Daniel James DeDora

to

The Graduate School

in Partial Fulfillment of the

requirements

for the degree of

Doctor of Philosophy

in

Biomedical Engineering

Stony Brook University

May, 2015

Stony Brook University

The Graduate School

Daniel James DeDora

We, the dissertation committee for the above candidate for the

Doctor of Philosophy degree, hereby recommend

acceptance of this dissertation.

Dr. Lilianne Mujica-Parodi – Dissertation Advisor
Associate Professor, Department of Biomedical Engineering

Dr. Terry Button - Chairperson of Defense
Associate Professor, Department of Biomedical Engineering

Dr. Helmut Strey
Associate Professor, Department of Biomedical Engineering

Dr. Lawrence Wald
Associate Professor, Department of Radiology
A.A. Martinos Center for Biomedical Imaging
Massachusetts General Hospital

This dissertation is accepted by the Graduate School

Charles Taber

Dean of the Graduate School

Abstract

of the Dissertation

Temporal fidelity and functional dynamics in functional MRI time-series analyses.

by

Daniel James DeDora

Doctor of Philosophy

in

Biomedical Engineering

Stony Brook University

2015

Functional magnetic resonance imaging (fMRI) has revolutionized the study of the human brain by allowing researchers and clinicians to map neural function at fine spatial resolutions. Modern fMRI acquisition and analytic techniques are beginning to uncover the network-scale dynamics of meso-circuits within the brain, which could lead to enhanced treatments or prevention of psychiatric and neurological illnesses. However, artifact and noise potentially compromise the validity of dynamic analyses. Here, we evaluate and utilize dynamic fMRI signals to advance the study of the human brain. The dissertation comprises three parts: a human study, a phantom study, and a combined human-phantom study. First, we use novel analyses and modeling techniques to define a brain meso-circuit associated with threat evaluation. We show that the inferior frontal gyrus (IFG) is significantly dysregulated in anxiety patients, and use causal modeling to reveal aberrant circuitry between the IFG, ventromedial prefrontal cortex, and amygdala during processing of ambiguous threat. Second, we prototyped (designed, manufactured, and validated) a dynamic phantom that enables the rigorous evaluation of the temporal fidelity of fMRI time-series with respect to controlled dynamic inputs. The phantom comprises concentric cylinders containing agarose gels whose magnetic susceptibilities are spatially varying; a novel pneumatic motor and fiber optic feedback system are coupled with a microcontroller to produce precisely timed changes in fMRI signal within predefined regions of the phantom. We validate the phantom by demonstrating biomimetic response functions and motion artifact-free output fMRI time-series. Third, we combine human and phantom data from three separate fMRI scanners to aid in the development of a novel measure of signal to noise for resting-state studies, deemed *signal fluctuation sensitivity* (SFS). We first use the phantom to develop and test SFS on data with known inputs, and compare SFS with classical temporal SNR (tSNR). We then validate SFS using human resting-state data, and demonstrate advantages over

tSNR. Taken together, the three elements of this dissertation advance fMRI state of the art, with broad implications for clinical neuroimaging.

To my God, and to my wife Caroline, my parents, and sisters. I would be nowhere without their unfailing support.

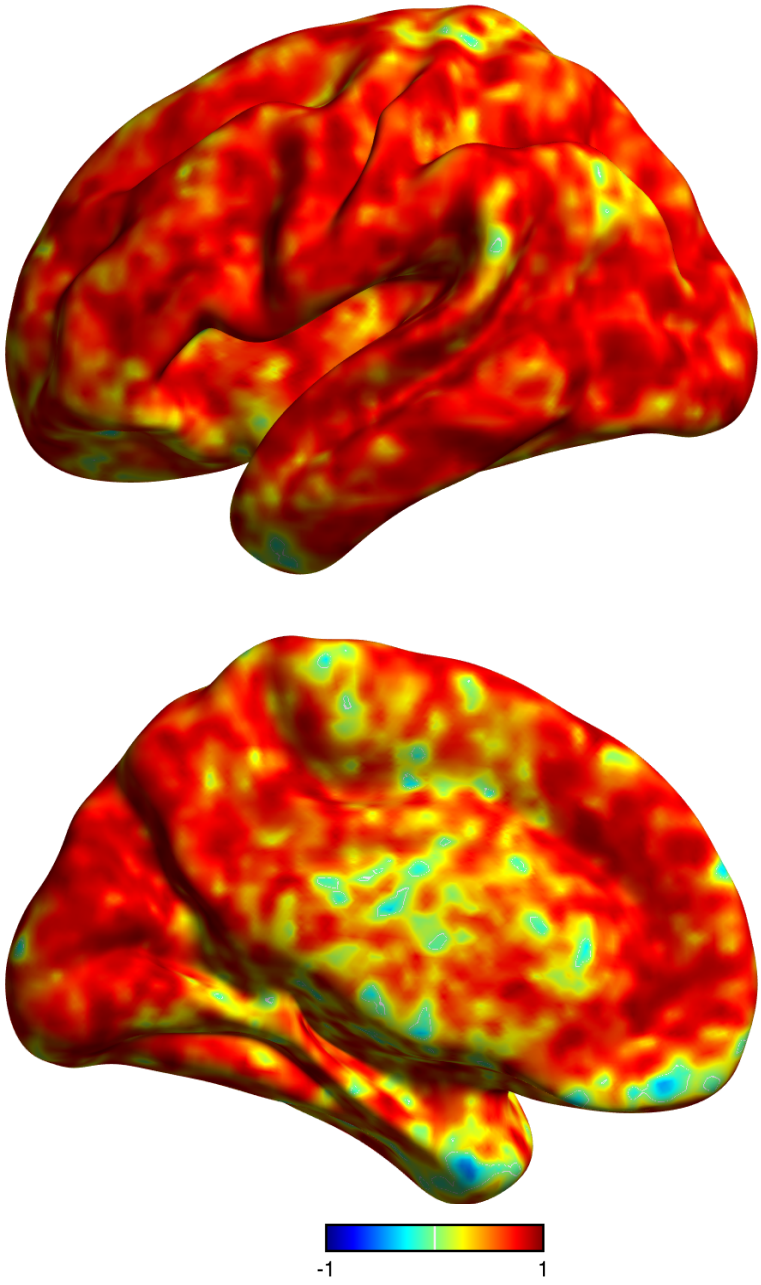

Frontispiece: Our novel measure of signal fluctuation sensitivity (SFS) in functional MRI is robustly predictive of neural synchrony (ReHo) in humans. Scale bar represents correlation between SFS and ReHo in 12 human subjects during a task-free scanning paradigm.

TABLE OF CONTENTS

LIST OF FIGURES

LIST OF TABLES

CHAPTER 1

1. Background and Introduction

Recent years have seen unprecedented investment in brain research, with the Human Brain Project aiming to simulate the human brain using supercomputers ($1.2 billion in European funds), the Brain Research through Advancing Innovative Neurotechnologies (BRAIN) project aiming to develop new and innovative technologies towards mapping brain activity ($100 million in US funds), and the Human Connectome Project aimed at producing an openly accessible map of functional and structural connectivity in humans ($40 million in US funds). These massive multicenter undertakings are fundamentally transforming our understanding of the brain. These projects are designed to couple computational techniques with modern imaging methods to offer valuable insight into the function and regulation of neural systems. When applied to functional MRI, however, computational techniques are sensitive to non-neural contributions from physiological noise and scanner noise. This dissertation focuses on the functional dynamics and fidelity of fMRI signal.

The aim of the following chapter is to describe the current state of the art in functional magnetic resonance imaging (fMRI). We begin with a survey of MRI, followed by an introduction to fMRI. This subsection includes brief discussions of neurobiological activity underlying fMRI signal changes, acquisition techniques, preprocessing pipelines, and sources of artifact. These topics set the stage for a review of what the authors believe to be the entirety of the available literature on functional MRI phantoms.

1.1 Magnetic Resonance Imaging

First developed by Paul Lauterbur (Lauterbur 1973), magnetic resonance imaging is often the tool of choice for the generation of images that map internal anatomy. Magnetic Resonance Imaging (MRI) utilizes the differential concentrations of hydrogen molecules in biological tissues to generate non-invasive images with high resolution. MRI works by sensing radiofrequency (RF) emissions following excitation under the influence of a large magnetic field and a combination of smaller gradients (Brown, Perthen et al. 2007). The MRI machine contains a uniform main field B_0, which is typically on the order of 1.5-7 Telsa (T) for modern imaging systems. Protons *precess* with a frequency (Larmor frequency) that is proportional to the magnetic field surrounding them. Three gradients are produced within the field (x, y, and z), which modify the local magnetic field and alter the Larmor frequency for slice-selection, the phase for phase encoding, and the frequency for frequency encoding. In summary, the main field is modulated as a function of local gradients. The change in each of these magnetic fields allows the localization of magnetic signal, while magnetic susceptibility differences between tissues allows contrast. The longitudinal and spin-spin relaxation constants of a tissue are deemed T_1 and T_2, respectively. A Fourier transform of these emissions produces images that detail the underlying tissues. MRI is now used by clinicians and researchers worldwide for an array of applications; these include cardiac imaging (Jabbour, Ismail et al. 2011, McLellan, McKenzie et al. 2011, Metzner, Kivelitz et al. 2011, Petryka, Misko et al. 2011, Thavendiranathan, Liu et al. 2011), tumor detection (Jaffar, Ain et al. 2011, Li, Padhani et al. 2011, Matsumura, Aoki et al. 2011, Nakanishi, Chuma et al. 2011), brain function mapping (Josephs and Henson 1999, Friston

2009, Radulescu and Mujica-Parodi 2009), diffusion weighting (Barbaro, Vitale et al. 2011, Rheinheimer, Stieltjes et al. 2011, Yuan, Wang et al. 2011), soft tissue damage (Brash, Foster et al. 1999), and intestinal imaging (McRobbie, Moore et al. 2007, Fruehauf, Menne et al. 2011, Haans, de Zwart et al. 2011), among others.

1.2 Functional MRI

For two decades, functional MRI (fMRI) has been an indispensible tool at the forefront of neuroimaging. fMRI utilizes the paramagnetism of deoxygenated blood to indirectly identify and map temporal changes in brain activity. This is called blood oxygen level dependent (BOLD) imaging (Ogawa, Lee et al. 1990), and frequently utilizes the echo-planar imaging sequence to measure $T2^*$ relaxation (Bruning, Seelos et al. 1999) (see below for EPI explanation). Briefly, when neurons in a region of the brain are activated, they quickly absorb available oxygen, resulting in an "initial dip" in MR signal due to the decreased relative susceptibility of a small group of neurons (see controversy regarding this dip (Renvall and Hari 2009)). The brain then sends a flood of freshly oxygenated blood to the area, which results in a signal increase (Buxton, Wong et al. 1998). After the cessation of activity, the brain returns to resting state (though there may be a post-stimulus undershoot, which is again controversial (Renvall and Hari 2009)). This neurobiological sequence – dip, spike, dip, rest - is known as the hemodynamic response. fMRI data is then analyzed statistically (see *1.3.4 - statistical analysis* for a brief overview of these steps) over experimental groups, brain regions of interest, or conditions (or all three). For illustrative purposes, results of fMRI are typically superimposed on a structural image (**Figure 1.1**). Naturally, many pulse sequences and reconstruction algorithms exist that are not discussed here. However, this section serves to introduce the reader to the space.

1.2.1 Echo Planar Imaging

Echo planar imaging is a common form of functional MRI (DeLaPaz 1994). After the scanner issues a slice-selective pulse (proportional to the Larmor frequency of the slice of interest), the scanner must fill a 2D matrix known as *k*-space using information obtained through frequency and phase encoding. In contrast to typical gradient echo imaging, where one line of k-space is filled per repetition time (TR), here a single excitation pulse is followed by a full filling of k-space through the alternation of powerful gradients; the scanner traces a continuous waveform through K-space. EPI images can be created very quickly (each slice can be produced in as little as 20ms), capturing the temporal dynamics of the hemodynamic response. Because EPI is a variant of gradient-echo imaging, the T_2 relaxation time of a material is sensitive to static field inhomogeneities. This shortens the apparent T_2, and is subsequently known as T_2^*.

1.2.2 Spiral Imaging

Another popular type of functional imaging is spiral imaging. Spiral imaging is similar to EPI; however, sinusoidal gradients are used instead of the rectangular shifts in EPI. This results in a filling of K-space starting from the center and spiraling outwards. While this is less taxing on the hardware (more gradual gradient changes), it requires significant post-processing to transform the circular K-space to a typical Cartesian coordinate system (Huettel, Song et al. 2004). Thus, our focus will be on echo-planar imaging.

1.2.3 Multiband and Parallel Imaging

Recently, several sophisticated image acquisition and reconstruction algorithms have enabled considerable advances in functional imaging. Though what follows are not all *pulse sequences* per se, these algorithms allow for considerably speedier acquisition times and are therefore worthy of discussion. Many of these methods allow the user to acquire fewer lines along the phase-encode direction of k-space, thus improving scan time.

Sensitivity encoding (SENSE) utilizes *a priori* knowledge of the acquisition area in a phased array coil. The coil must be SENSE-enabled, which refers to slight variances in coil sensitivity along the phase-encode direction. This method requires a calibration scan but allows the user to acquire fewer phase-encode lines in k-space. SENSE addresses the aliasing inherent in undersampled k-space by solving a linear system of equations synthesized from two images and their respective coil sensitivities (McRobbie, Moore et al. 2011). mSENSE is a slight modification that trades the acquisition of a calibration scan for additional lines of k-space. Artifacts can occur with this method when the field of view does not contain the full region of interest; this results in a kaleidoscope-type effect known as "hot-lips."

Simultaneous acquisition of spatial harmonics (SMASH) uses combinations of array coil sensitivities to create "virtual" phase encoding. Similar to SENSE, this method reduces the number of phase encoding steps. However, this method requires very specific coil designs with known sensitivities. Auto-SMASH acquires additional phase-encoded lines of k-space during acquisition, and solves a linear system of equations to fill the remaining k-space. VD-Auto-SMASH further reduces artifact but requires more lines of k-space to be acquired; however, suboptimal calibration of element sensitivities leads to poor reconstructions. Thus, a derivative of VD-AutoSMASH is Generalized Autocalibrating partially parallel acquisitions (GRAPPA). GRAPPA uses some spatial information inherent in the components of the headcoil array to replace some of the spatial encoding with gradients; however, it uses a sum of squares method to enhance the reconstruction (Griswold, Jakob et al. 2002). For a review of each of these techniques, see (Blaimer, Breuer et al. 2004)

1.2.4 Preprocessing Overview

An inherent limitation of fMRI is that signal changes are typically on the order of only a 1-3% percent; the magnitude of the inherent noise is also 1% percent, which complicates data analysis and interpretation. Thus, a lengthy set of preprocessing procedures nearly always precedes the analysis of fMRI data.

The preprocessing pipeline in fMRI is extensive. Research groups typically utilize popular preprocessing packages, including *FSL, AFNI, Free Surfer, BrainVoyager* and *SPM*. The steps in preprocessing will be described as in (Huettel, Song et al. 2004). This section is meant to be introduction, and is by no means exhaustive.

Slice time correction - Each volume is acquired rapidly in EPI; however, each slice in a volume does represent a slightly different time point. For example, if the sampling rate is 2 (TR = 2000ms), and 50 slices are acquired within that two-second window, then the first and last slice can potentially be acquired nearly two full seconds apart. Given the temporal resolution of the hemodynamic response, critical changes in signal could occur within this window. Interleaving

slice acquisitions is often used to mitigate these time differences (though it is necessary for parallel imaging purposes as well). First, slice acquisition time correction is performed. This usually includes a modification of the predicted hemodynamic response as well as an interpolation of the results to account for slight differences in signal timing.

Motion Correction - Head motion is a pervasive problem in fMRI, since slight motions (a few mm) can result in large fluctuations in signal. These fluctuations are nonlinear and often result in spurious spatial and temporal correlations in data (Power, Barnes et al. 2012). Cortical surfaces and certain tissue interfaces are often most vulnerable to these types of motion, since small movements can introduce tissue with different properties into a voxel or cluster (Huettel, Song et al. 2004). Typically, the first strategy for motion correction is called coregistration; it ensures that the brain is in the same spatial location in each image. Realignment uses a combination of three dimensional rotations and translations to coregister each volume to an initial image; a least squares approach is used to minimize the differences between successive images (Friston, Ashburner et al. 1995, Friston, Williams et al. 1996, Bullmore, Brammer et al. 1999). Once alignment is complete, spatial interpolation is performed to calculate the theoretical values of signal within the voxel that would have been measured without head movement. This routine is not sufficient to remove motion artifacts, however (see *Motion* section).

Geometric distortion correction - These distortions are usually caused by static field inhomogeneities. The current method to correct for distortion is called bias-field estimation; this technique estimates inhomogeneities based on the acquired set of images (including the structural image). The American College of Radiology has a certified phantom designed to measure geometric fidelity, which will be covered in a later section.

Normalization - This allows the user to map low-resolution functional images to high-resolution structural images - often Talairach's image, which is a standard in fMRI. Gross features, such as the center sulci and ventricles, are mapped onto each other to rescale the image.

Filtering and smoothing - Filtering and smoothing are used to remove random noise. Sources of noise in fMRI will be covered below, but these sources include physiological (heart rate, breathing, movement) and scanner-related (instabilities) noise. fMRI data is often high-pass filtered to remove underlying trends, and is sometimes band-pass filtered to remove trends as well as high-frequency noise (Kruggel, von Cramon et al. 1999). The application of Gaussian kernels to spatially smooth fMRI data is often used to improve signal detection and to better identify regions of activity. Smoothing kernels are typically between 4-8 mm wide. This assumes that noise is random and uncorrelated, such that averaging between voxels enhances signal and cancels out noise. In practice, however, this is not an entirely valid assumption.

1.3 Sources of Noise in fMRI

fMRI analyses are subject to numerous sources of artifact and noise. Here, we briefly describe these noise sources and their effect on analyses. For the purposes of this dissertation, we focus on scanner and equipment related noise sources. For an in-depth discussion on the topic, the reader is directed to an excellent review by Greve and colleagues (Greve, Brown et al. 2013).

1.3.1 Thermal Noise

Thermal noise is the result of Brownian motion of charged carriers within a substrate. Ions, being charged particles, create small magnetic fields as they move. These small magnetic fields are

picked up by the MR-scanner. In general, thermal noise can be modeled by homoscedastic Gaussian random noise (Greve, Brown et al. 2013) whose amplitude is guided by coil loading (Triantafyllou, Hoge et al. 2005), and is an independent *additive* noise to BOLD fluctuations (assuming bandwidth is fixed)(Wald 2012). While smoothing, averaging, and filtering are typically utilized to remove thermal noise post-hoc, thermal noise is not perfectly temporally uncorrelated (Triantafyllou, Polimeni et al. 2011). Indeed, colored noise has long been observed in static phantoms (Zarahn, Aguirre et al. 1997).

1.3.2 Scanner Instabilities

Scanner instabilities encompass a fairly broad subset of noise in functional MRI. Instabilities are multiplicative instrument-induced noise sources that influence the k-space trajectories, RF pulses, and slice select pulses during a scan (Greve, Mueller et al. 2011). Fluctuations in resistive shim currents, RF gain or phase, receiver amplifier gain or phase, and gradients can underlie these artifacts (Greve, Mueller et al. 2011). Some controversy exists over whether or not these fluctuations are exacerbated in modern scanning paradigms, as scanners are subject to increasingly demanding scan protocols (Greve, Mueller et al. 2011, Mikkelsen and Lund 2013). Much fMRI research operates under the assumption of minimal scanner instability (Triantafyllou, Hoge et al. 2005), which is consistent with existing reports where physiological and background noise constitute at least 95% of the variance in an fMRI experiment (Greve, Mueller et al. 2011). Additionally, recent studies estimate that thermal noise and scanner instabilities account for approximately 25% of drift effects observed in fMRI.

In contrast to these reports indicating the fairly innocuous effect of scanner instabilities and thermal noise, other recent studies suggest significant differences in scanner performance between scanners. Our very recent work found significant differences in the spectral signatures of two healthy groups of age- and gender-matched participants (Rubin, Fekete et al. 2013). Inter-scanner reliability is consistently lower than intra-scanner reliability (Friedman and Glover 2006); by some estimates, inter-scanner reproducibility hovers around 10% (Friedman, Stern et al. 2008). It is clear that proper quality assurance and calibration routines should be strictly followed, but whether this approach is enough to ensure precise and accurate fMRI results is still controversial.

1.3.3 Physiological Noise

Unlike thermal noise, physiological noise is *multiplicative* and scales with field strength (Kruger, Kastrup et al. 2001). Physiological noise is an umbrella term for a subset of noise sources stemming from natural physiological processes, including heart rate and breathing.

Functional MRI is sensitive to changes in the concentration of deoxygenated hemoglobin in the blood. The beating heart sends a rush of freshly oxygenated blood to the brain, and thereby produces a pulsatile fluctuation in fMRI signal (Weisskoff, Baker et al. 1993). This heart-rate based fMRI fluctuation is often faster than 1 Hz. When fMRI experiments utilize a sampling rate of < 0.5 Hz ($TR < 2$), heart rate effects get aliased into lower frequencies (Greve, Brown et al. 2013). Heart rate can be tracked with MR-compatible electrocardiogram, allowing regression of heart rate-related variables during preprocessing.

Breathing presents a two-pronged source of noise. First, breathing introduces fluctuations in deoxygenated blood flow to the brain, modifying fMRI signal similarly to heart rate; in this case, the fluctuation is on the order of 0.3 Hz. As with heart rate, it is possible to track breathing

with an expansion belt and implement a regressor during preprocessing. Second, breathing introduces a small amount of motion. Images stretch and compress with each breath, causing partial volume and spin history effects (Greve, Brown et al. 2013) (motion will be covered in the next section). Finally, breathing creates a shift in the main field at the head, leading to distortions (Raj, Anderson et al. 2001).

Physiological noise has been well studied. Several groups have found that physiological noise is a dominant source of fMRI variance at moderate to high field (≥ 3T) (Kruger, Kastrup et al. 2001, Triantafyllou, Hoge et al. 2005, Hutton, Josephs et al. 2011) and low resolution, while thermal noise becomes more prominent at high resolution and low field (Triantafyllou, Hoge et al. 2005). The ratio of physiological noise to thermal noise grows as flip angle increases and as greater array coils are used (Triantafyllou, Polimeni et al. 2011). Many software algorithms and modeling approaches have been produced to remove physiological noise from fMRI time-series, including principal component approaches (Bullmore, Rabe-Hesketh et al. 1996, Hansen, Larsen et al. 1999), independent component approaches (McKeown, Jung et al. 1998, McKeown, Makeig et al. 1998, McKeown and Sejnowski 1998, Beckmann and Smith 2004), canonical correlation analyses (Churchill, Yourganov et al. 2012, Churchill and Strother 2013), and the well-known RETROICOR method (Glover, Li et al. 2000). It is critically important to include physiological noise in simulations to avoid bias (Welvaert and Rosseel 2012). For a review of physiological noise in resting-state human imaging, see (Birn 2012, Birn, Cornejo et al. 2014).

1.3.4 Motion-related noise

Motion-related noise is one of the most persistent and difficult noise sources to deal with. As an object moves, it interacts with the gradients along each dimension. This interaction changes the relaxation properties of the substrate, and thus, influences the measured fMRI signal. If an object is moving between imaging slices and is re-excited prior to relaxing fully, the new Larmor frequency will both a function of the current field strength (which is a function of the gradients and position) as well as the previous Larmor frequency. This is known as the *spin history effect*, and can be modeled as an autoregressive moving average model (Friston, Williams et al. 1996).

Realignment of images is the most frequency used method for partial correction of movement (Friston, Ashburner et al. 1995). However, realignment does not fully remove these artifacts. Often, researchers will also regress motion and a second order term – including its square or its derivative (Rubin, Fekete et al. 2013). The analysis of stimulus-driven tasks is further complicated by task-correlated motion (Bullmore, Brammer et al. 1999); this type of motion is common in "active" tasks, such as a game, or in tasks that elicit emotion or surprise. This creates a problem because regression of motion can also remove neural signal. Regression can also create spurious activations due the presence of outliers (Freire and Mangin 2001).

Motion of the head does not affect all voxels uniformly. It was previously shown that motion during resting-state results in decreased long-range correlations and increased short-range correlations (Power, Barnes et al. 2012). There does not seem to be a simple, linear relationship between motion and fMRI signal. Thus, scrubbing (or censoring) of affected images has been proposed (Power, Barnes et al. 2012). Filtering and spike correction can also improve motion correction algorithms (Jo, Gotts et al. 2013). For a detailed review of motion-artifact related preprocessing routines, see (Power, Schlaggar et al. 2015).

1.4 Calibration and Quality Assurance

As discussed above, many sources of noise influence fMRI images: patient motion, magnetic field inhomogeneities (particularly with gradient echo images), signal drift, aliasing, scanner variability (particularly with functional imaging), signal dropout at air-tissue interfaces, signal distortion from fat, blood flow, peristaltic motion, cardiac motion, phase wrap-around, Gibb's artifact, zipper artifact, and others (McRobbie, Moore et al. 2007). Though many of these sources of artifact are caused specifically by patient physiology, many are a direct result of equipment shortcomings. Thus, tight calibration and quality assurance procedures are necessary to ensure optimal MRI function.

There are various ways to optimize MRI function. Ensuring the proper MRI environment can help to prevent many problems before they occur. Following installation of an MR machine, shimming optimizes the uniformity of the MRI (McRobbie, Moore et al. 2007). Nonetheless, quality assurance is performed to ensure optimal signal to noise (SNR), uniformity, linearity, resolution, slice parameters, contrast to noise ratios (McRobbie, Moore et al. 2007). Quality assurance protocols are performed using a *phantom*, which is an inorganic object that produces a desired MR signal.

The American College of Radiology (ACR) requires a standard phantom for accreditation, which most QA protocols for clinical MRI use today (Radiology 2005). The ACR MRI phantom (**Figure 1.2**) is a sealed cylinder filled with approximately 300 mL of an electrolyte solution; it contains various internal structures to perform quality assurance protocols – for details, see (Radiology 2005). This phantom is used to optimize the following seven parameters: 1) geometric accuracy, 2) high-contrast spatial resolution, 3) slice-thickness accuracy, 4) slice-position accuracy, 5) image intensity accuracy, 6) percent-signal ghosting, and 7) low-contrast object detectability (Radiology 2005). These optimization procedures help ensure high-quality MR images. However, despite their obvious utility for structural MRI, static phantoms fall short in the functional realm of neuroimaging.

Modern functional imaging facilities utilize similar phantoms for ACR accreditation. These phantoms are static in the temporal domain. They do not allow a researcher to assess the fidelity of small signal changes. Accordingly, several research groups have developed phantoms capable of producing functional MRI signal with predictable temporal dynamics; these are used to ensure that a known input creates a consistent signal output. These phantoms, sometimes called *dynamic phantoms*, will be the focus of the remainder of this section.

1.4 Dynamic Phantoms

Four groups have published designs for functional MRI phantoms capable of producing simulated BOLD signal. Three utilize inner circuitry to produce small magnetic fields, and the fourth is a simple two-compartment cylinder that is hand-operated. The most notable fMRI phantom is the SmartPhantom.

1.4.1 SmartPhantom

The SmartPhantom is a patented device used to create simulated BOLD data (Cheng, Zhao et al. 2004, Friedman, Zhao et al. 2004, Cheng, Zhao et al. 2006, Zhao, White et al. 2006). The device was designed to allow for inter-scanner and intra-scanner quality control and calibration experiments. Additionally, it could be used for the comparison of modern analysis software. It is designed to be scanned as part of a routine maintenance procedure, and fits snuggly into the headcoil.

The SmartPhantom comprises a combination of three RC circuits and a larger LC circuit with switch-based voltage sources to induce controllable magnetic fields within a large, square coil (Cheng, Zhao et al. 2004, Friedman, Zhao et al. 2004, Cheng, Zhao et al. 2006, Zhao, White et al. 2006). The coil is embedded within a cylinder of hydrogel, which functions as the region of interest. When a magnetic field is induced within the phantom, the $T2^*$ of the surrounding hydrogel is modified, and signal is enhanced. The equation governing signal enhancement, as derived from Biot-Savart law by the authors, is:

$$enhl = \sqrt{1 + (\frac{q}{R(t) + Z_0})} - 1$$

where *R(t)* is the resistance of the circuit as a function of time, which is modified by the user. Z_0 and q are constants associated with the device and scanner (Cheng, Zhao et al. 2006). The phantom is remotely controlled, and can simulate the hemodynamic response. The authors claim that a relatively uniform activation area of approximately 14 cm^3 can be produced with their device, which is comparable to commonly imaged brain regions (Cheng, Zhao et al. 2006).

The SmartPhantom has been used for various experimental purposes, including an inter-scanner reproducibility study (Friedman, Zhao et al. 2004). The authors compared a Siemens 1.5T Sonata and a GE Signa Excite 1.5T, both with quadrature head coils; they used four different flip angles, and four signal enhancement levels. They found that the GE had more scanner noise, and that the machines had small but noticeable differences in signal change. This study suggested that, as the authors had predicted, scanner performance was not identical. Because analysis depends on minute effect sizes amidst large amounts of noise, these differences would undoubtedly be significant for studies with small numbers of participants. The SMARTPHANTOM has also been used to present a new method for improving the derivation of the hemodynamic response function (Li, Reza et al. 2007). The authors presented a method to measure and correct for the aliasing of high-frequency noise into lower frequencies in the fMRI signal.

1.4.2 fMRI Reference Phantom

The need to correct for within-scan signal drift suggests that *a priori* calibrations may not suffice for functional studies (Renvall, Joensuu et al. 2006, Renvall 2009). Knowing this, a reference phantom was developed, designed to be scanned *simultaneously* within research paradigms. By simulating brain responses during a functional study, changes in signal strength due to dynamic field inhomogeneities and other unexpected effects can be quantified and regressed from subject scan data.

The reference phantom works via the same principle as the SmartPhantom. A circuit is embedded in a hydrogel, and current is used to produce magnetic fields; these fields can simulate BOLD response within an fMRI (Renvall, Joensuu et al. 2006, Renvall 2009). Most importantly, the reference phantom is a small rod shape, which can be scanned beside the subject in the headcoil. This phantom was most recently used to evaluate the controversial "post stimulus undershoot" in the absence of physiological effects (Renvall and Hari 2009). The authors found that *transients* occur when fMRI signals change sharply, and conjecture that this effect could be scanner-based and not physiological. This finding highlights just one of many uses of dynamic phantoms.

1.4.3 Two-compartment Gel Phantom

Utilizing only hydrogels and plexiglass, this phantom is the only truly MR-compatible design available (Olsrud, Nilsson et al. 2008). The phantom has two compartments, each filled with a specific concentration of doped-agarose gel. Between TRs, the operator slides the phantom between the "active" and "inactive" regions, which produces BOLD contrast. The principle is based on the following equation:

$$PSC = \frac{TE}{(T_2^*)^2} \Delta T_2^* \bullet 100[\%]$$

where percent signal change is dependent on the change in T_2^* value, as well as the echo time. The author published a proof-of-concept study to show that differential agarose concentrations can produce physically simulated fMRI signal changes.

1.4.4 Trace ion MRI Phantom

The most recent dynamic phantom design was published in June 2014 (Qiu, Kwok et al. 2014). Qiu et. al. developed a phantom containing small parallel electric plates within propylene carbonate solutions. When an electric field is applied, the polar solvent forms ion currents; these ion currents create dephasing in magnetic fields perpendicular to the main field. The authors were able to control the fMRI signal within a single slice, but the wiring creates noticeable distortion in the images.

1.5 Conclusion

These phantom designs establish several methods of creating on/off signal changes in fMRI. However, each of these phantoms suffers from one of two key issues – (1) presence of magnetic materials, including wires and plates that cause signal artifact, or (2) inability to produce complex input signals over multiple slices. The utility of a dynamic phantom has grown even greater in recent years, as dynamic analyses relying on precise temporal fidelity replace more traditional functional localization studies. Therefore, the need for an MRI-compatible and automated phantom still exists.

Chapter 1 Figures and Captions

Figure 1.1: An example fMRI statistical map.

Functional MRI of the left amygdala during a masked-fear detection protocol (Carlson, Greenberg et al. 2010).

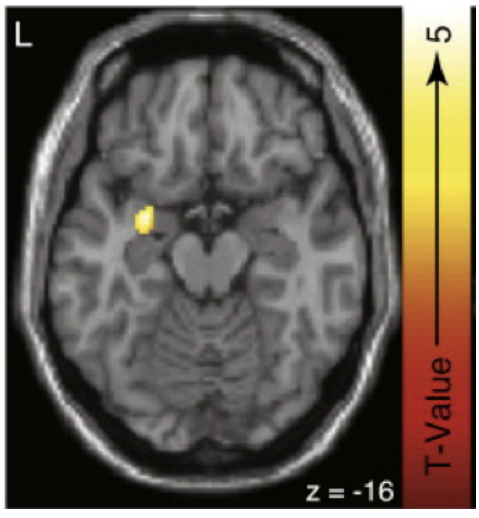

Figure 1.2: The ACR MRI phantom.

a) Cross section showing various structures, including a lipid-containing section, and hole-pair arrays. b) Longitudinal section of the phantom (American College of Radiology).

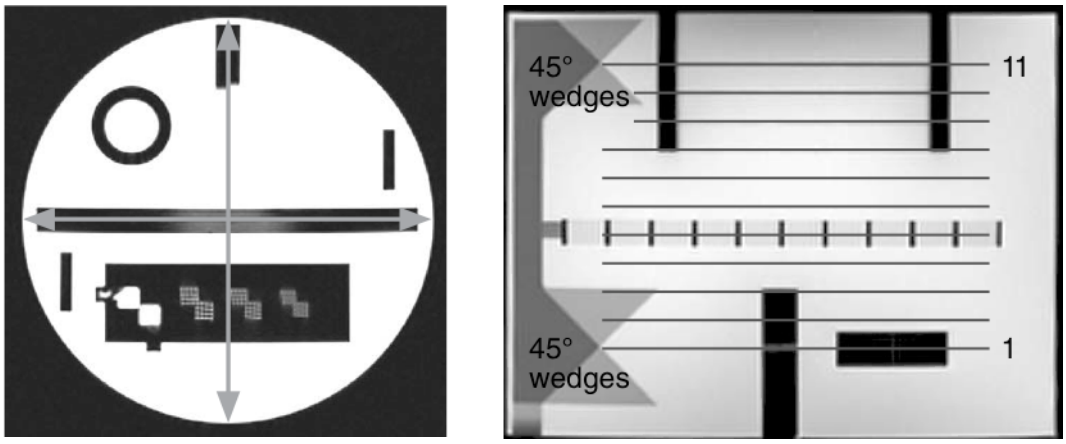

CHAPTER 2

2. Clinically anxious patients show disrupted feedback between inferior frontal gyrus and prefrontal-limbic control circuit.

Preface

Portions of this chapter have been reproduced from:

Daniel James DeDora, J. Cha, S. Nedic, J. Ide, T. Greenberg, G. Hajcak, L.R. Mujica-Parodi, "Clinically anxious patients show disrupted feedback between inferior frontal gyrus and prefrontal-limbic control circuit.", *Under review, Journal of Neuroscience*

The authors listed in the above manuscript have contributed towards the data reported in this chapter.

2.1 Introduction

Anxiety disorders have been linked with flawed evaluation of threat (Greenberg, Carlson et al. 2013, Cha, Carlson et al. 2014), in which innocuous stimuli elicit neurobiological and behavioral fear responses. This hypersensitivity to threat may be driven by diminished recruitment of the lateral prefrontal cortex during cognitive and emotional tasks (Bishop, Duncan et al. 2004, Bishop 2009, Strawn, Bitter et al. 2012). The inferior frontal gyrus (IFG) is a subregion of the lateral prefrontal cortex that plays an important role in the regulation of emotion and attention (Aron, Fletcher et al. 2003, Ochsner and Gross 2005, Depue, Curran et al. 2007, Sagaspe, Schwartz et al. 2011, Ochsner, Silvers et al. 2012, Vanderhasselt, Kuhn et al. 2012), including modulation of the threat response (Fitzgerald, Angstadt et al. 2006, Eippert, Veit et al. 2007). Previously, we showed that IFG (Brodmann's Area 45) reactivity to fearful faces positively correlated with suppression of the amygdala responses, and negatively correlated with trait anxiety in healthy individuals (Mujica-Parodi, Korgaonkar et al. 2009). Later, we quantified the functional dynamics of the IFG in trait anxious individuals with power spectrum scale invariance (PSSI) (Tolkunov, Rubin et al. 2010), a control systems-derived measure of circuit-wide regulation. PSSI showed that individuals with greater trait anxiety exhibited IFG functional dynamics that shifted away from optimal regulation ('pink noise,' see Radulescu and Mujica-Parodi 2014). However, the underlying basis for the dysregulation is under-determined, as dysregulatory dynamics can result either from stronger chaotic excitatory inputs or weaker negative feedback or both (Radulescu and Mujica-Parodi 2014). Recently, we observed the same pattern of aberrant IFG functional dynamics in a high sensation-seeking group of first-time skydivers with poor threat-evaluation (Mujica-Parodi, Carlson et al. 2014). The commonality in the IFG results across the two extreme ends of the anxiety spectrum in healthy individuals, both sharing deficits in threat-evaluation, raised the question of whether our (Mujica-Parodi, Korgaonkar et al. 2009, Radulescu and Mujica-Parodi 2014) and others' (Aron, Fletcher et al. 2003, Bishop, Duncan et al. 2004, Ochsner and Gross 2005, Fitzgerald, Angstadt et al. 2006, Depue, Curran et al. 2007, Eippert, Veit et al. 2007, Bishop 2009, Sagaspe, Schwartz et al. 2011) initial view of the IFG as simply an inhibitory component of the negative feedback loop regulating emotion might be incomplete.

Here, we focus on clarifying three critical aspects of the IFG's role within the prefrontal-limbic control circuit responsible for threat evaluation, with the aim of better informing our previous results, as well as better interpreting the region's role across the emotion literature. First, do our trait anxiety results (aberrant IFG dynamics) continue to hold when we move to clinical anxiety? Second, if so, does the IFG provide the direct inhibitory component of the prefrontal-limbic control system, as we and others initially suggested, or does it function in a distinct (perhaps evaluative) capacity within the circuit, as suggested by our later findings and the wider, non-affective, fMRI literature on that area? Third, do the aberrant dynamics first observed in trait anxiety reflect hyper-excitatory function and/or weaker regulation across the circuit?

To address these three questions, we further analyzed data on a fear generalization task that we have previously shown to be capable of probing subtle features of threat disambiguation in clinical anxiety (Greenberg, Carlson et al. 2013, Cha, Carlson et al. 2014). For this study, we recruited medication-free individuals with clinical anxiety (GAD) and age- and gender-matched controls to take part in a fear-generalization paradigm (Greenberg, Carlson et al. 2013), which included stimuli that were threat-ambiguous due to their perceptual similarity to a conditioned

stimulus. Our prior work explored traditional activation-based measures in the context of fear generalization (Greenberg, Carlson et al. 2013, Cha, Carlson et al. 2014). Here, we build upon this work: we first use PSSI to test for dysregulatory functional dynamics along the entire time-series; then use functional and structural connectivity analyses, including stochastic dynamic causal modeling, to further interpret our results.

2.2 Methods

2.2.1 Study Design

This data set includes 57 participants (M_{age} = 22.3, *SD* = 4.5, Table 1), who took part in a fear generalization task while being scanned. Of these, 32 were patients with Generalized Anxiety Disorder and 25 were healthy controls (HC). There is a significantly higher occurrence of anxiety disorders in females than males (McLean, Asnaani et al. 2011); thus, we tested only females for the study to avoid potentially uneven sample sizes due to lack of male participants. This study was approved by the Stony Brook University Institutional Review Board; all participants provided informed consent.

2.2.2 Diagnoses

Clinical diagnoses were performed in two steps: informal clinical interview, and a structured clinical interview. Diagnoses were based on DSM-IV Axis I Disorders (American Psychiatric Association. and American Psychiatric Association. Task Force on DSM-IV. 2000, First, Spitzer et al. 2002). The control group was cleared of Axis I diagnoses, while the patient group was diagnosed with Generalized Anxiety Disorder (GAD); 17 of the 32 patients were diagnosed with comorbid GAD and Major Depressive Disorder (MDD). All participants were free from psychiatric medication for at least six months leading up to the experiment; additional exclusion criteria included presence of another major psychiatric illness such as bipolar disorder, alcohol or substance dependence, and schizophrenia. All participants completed several self-report questionnaires, including the Mood and Anxiety Symptom Questionnaires (MASQ)(Watson, Weber et al. 1995), presented in **Table 2.1**.

2.2.3 fMRI Task

After screening and consenting in accordance with a protocol approved by the Stony Brook University Institutional Review Board, participants read written instructions for the entire study. The fear generalization task was administered inside the fMRI scanner. Before the task, a voltage level was set for each participant to a level that was "uncomfortable but not painful" and was delivered to the left forearm (Constant Voltage Stimulator STM 200; Biopac Systems). Instructions for the task were then provided again verbally. Participants were told that a mid-sized rectangle (conditioned stimulus; CS) indicated a 50% probability that they would receive a subsequent electric shock but that shocks would never follow rectangles of greater or lesser size. Following the instruction, we administered a *conditioning phase*. This included five presentations of the CS with the shock (i.e., 100% probability) and a single presentation of each generalized stimulus (GS) in a pseudo-random order with inter-stimulus intervals of 4 –10 s. A *generalization phase* immediately followed. The fear generalization task (**Figure 2.1**) consisted of the presentation of an initial fixation screen (a white cross on a black background), followed by a 2 s stimulus presentation. For the CS, a red rectangle was paired with 500 ms of electric shock with a partial reinforcement schedule of a 50% delivery probability, 1500 ms after the cue onset. For GS, we used six red rectangles with systematically varying widths (i.e., ±20%, ±40%,

and ±60%) without shock. Each GS was pseudo-randomly presented 15 times, and the CS was presented 30 times: 15 with shock and 15 without shock, for a total of 120 trials. Trials were flanked with inter-stimulus intervals ranging from 4 to 10 s with a white fixation crosshair on a black background. Task duration was 15 minutes and 24s.

2.2.4 MRI Data Acquisition

We scanned participants with a 3T Siemens Magnetom Trio scanner within the Social, Cognitive, and Affective Neuroscience center at Stony Brook University. We acquired a total of 440 T_2*-weighted echo planar images with an oblique coronal angle and TR = 2100ms, TE = 23ms, flip angle = 83º, matrix = 96 × 96, FOV = 224 × 224mm, slices = 37, and slice thickness = 3.5mm. For structural scans, T_1-weighted images were acquired with the following parameters: TR = 1900 ms, TE = 2.53, flip angle = 9°, FOV = 176 × 250 × 250 mm, matrix = 176 × 256 × 256, and voxel size = 1 × 0.98 × 0.98 mm. Diffusion Tensor Imaging (DTI) was collected in a separate session. We used the following parameters to collect DTI: TR = 5500 ms, TE = 93 ms, FOV = 220 × 220 mm, matrix = 120 × 220 × 220, voxel size = 1.7 × 1.7 × 3.0 mm, EPI factor = 128, slices = 40, slice thickness = 3 mm, bandwidth = 1396 Hz/pixel, and GRAPPA acceleration factor = 2. The series included two initial images acquired without diffusion weighting and with diffusion weighting along 40 non-collinear directions (b = 800 sm^{-2}).

2.2.5 fMRI Analyses

2.2.5.1 Overview:

Standard task-based activation results for this study, showing neural correlates of fear generalization in GAD, have already been reported (Greenberg, Carlson et al. 2013, Greenberg, Carlson et al. 2013); here, we focused on identifying key features of circuit regulation using systems-based analyses across the entire time-series. First, we examined circuit efficiency of the negative feedback loop using *power spectrum scale invariance (PSSI)* β-signatures (Rubin, Fekete et al. 2013) from the fear generalization fMRI data. Autocorrelation provided complementary information, identifying timescales for feedback. Next, we tested our hypothesis that disrupted corticolimbic regulation of negative affect (quantified by PSSI β-signatures) in the GAD group was linked to altered corticolimbic connectivity (Radulescu and Mujica-Parodi 2014), using three techniques. As a first step towards defining connectivity associated with β-signatures, we used *psychophysiological interaction (PPI) analysis* to identify regions of interest (ROI). We then applied *stochastic Dynamic Causal Modeling (sDCM)*, defining prefrontal (IFG, vmPFC) ROIs from previously-established connectivity analyses (Greenberg, Carlson et al. 2013, Cha, Greenberg et al. 2014), and the amygdala from a standardized atlas. Finally, we estimated integrity of the major corticolimbic white matter pathway—the uncinate fasciculus—using *diffusion probabilistic tractography*, and tested for a relationship between fiber integrity of the UF and IFG β-signatures.

2.2.5.2 Preprocessing:

We performed standard preprocessing procedures for fMRI, including slice time correction, motion correction, normalization, and smoothing with a 6 mm FWHM Gaussian kernel in SPM8 (www.fil.ion.ucl.ac.uk/spm). In addition, our preprocessing procedures included detrending and regression of global signal, cerebral spinal fluid, white matter, and six degrees of motion (Rubin, Fekete et al. 2013).

2.2.5.3 Power Spectrum Scale Invariance:

Using methods previously optimized by our group for fMRI (Rubin, Fekete et al. 2013), we estimated PSSI β from each FFT-transformed time series S(*f*) as per $S(f) \propto f^{-\beta}$. Power spectrum densities were computed from preprocessed EPI images on a voxel-wise basis and plotted on a log-log scale. We computed the slope of the linear fit (β) within a frequency window of 0.01-0.1 Hz using least squares fitting; this range of frequencies has previously been shown to obey a power-law model (He, Zempel et al. 2010, He 2011). Consistent with other groups, as well as our more recent publications using PSSI, here we used preprocessed time-series without taking the derivative and reported −β to simplify interpretation of correlations by having PSSI represented by positive numbers. Thus, β = 0 represents a power spectrum with maximum entropy (*white noise*), and increasing β represents greater persistence (which can be due either to diminished excitatory inputs or tighter homeostatic constraint over the system via negative feedback (Radulescu and Mujica-Parodi 2014)). Group differences in β-signatures were examined using voxel-wise t-tests. Independent variables included group and subject, while individual β images were used as dependent variables. To rule out head motion related artifacts on β-signatures (Rubin, Fekete et al. 2013), we confirmed no group differences in movement (e.g., absolute maximum translation, maximum rotation, mean translation, mean rotation) (two-sample t-test, *p*'s > .3). We then tested for correlations between PSSI values and MASQ anxiety subscales in MATLAB (The Mathworks Inc., Natick, MA, USA).

2.2.5.4 Autocorrelation Function:

To aid in the circuit-wide interpretation of PSSI, we also computed the temporal autocorrelation function (ACF) of preprocessed blood oxygen level dependent (BOLD) time-series. Negative feedback loops produce outputs in the form of damped oscillations, as feed-forward (excitatory) and feedback (inhibitory) components work in series (i.e., with some lag) to establish homeostasis. Closed-loop systems with greater negative feedback have more 'memory' within their time-series, as outputs not only reflect inputs, but also previous outputs. The ACF reflects the correlation of a signal with itself at different time lags, and thus provides more detailed information about the speed at which feedback occurs. Here, we modeled the ACF as a decaying exponential function with mean lifetime parameter τ(s), the system's 'memory' (the amount of time a signal maintains an association with past and future values). A time-series from a system with stronger feedback exhibits greater persistence/memory and therefore longer mean lifetimes τ(s), while a time-series from a system under perturbation and no feedback exhibits greater chaos (*white* noise) with a τ(s) close to zero seconds.

PSSI and ACF are related via the Wiener-Khinchin theorem, which states that the Fourier transform of the ACF is equivalent to the power spectral density, with which PSSI is computed. The ACF augments PSSI analysis in two ways: (i) the autocorrelation is a function of time, and its mean lifetime can be expressed in units of seconds, making it more easily interpretable than PSSI β-signatures (which are expressed as ∂(log(power))/∂(log(frequency))), and (ii) model fit is improved compared with PSSI, partially owing to the use of least squares fitting in log-log space in PSSI (Clauset, Shalizi et al. 2009).

We estimated voxel-wise ACF using the Econometrics Toolbox implemented in MATLAB R2010a. We then fit an exponential function of the form $y = ae^{-bx}$ to the first 9 (lag = 8) points of each voxel's ACF using the nonlinear least-squares fitting method as implemented in the Curve Fitting Toolbox within MATLAB R2010a. We chose to model eight lags (16.8 seconds at TR = 2.1s) because the canonical hemodynamic response function spans 16 seconds post stimulus (Miezin, Maccotta et al. 2000); this duration was found to allow for full relaxation

of ACF signal (see **Figure 2.2c**). Here, b values are related to the mean lifetime decay of a signal, τ(s), through the relation $\tau = 1/b \times TR$. Group differences in gray matter voxel-wise b values were examined using the same general linear model approach and t-contrasts in SPM as in the PSSI group differences analysis. Finally, ACF b values were converted to mean half-life τ for interpretation. Notice that the size of τ determines the rate of decay of ACF, with lower τ signifying faster decay (more randomness/lower β) and higher τ signifying slower decay (more persistence/higher β). The entire procedure was limited to gray matter voxels in order to reduce computational time associated with nonlinear fitting. It is important to differentiate the temporal autocorrelation of a time-series reported here and the autocorrelation of the residuals following GLM or similar analyses; the latter refers to temporal pre-whitening of a signal, a technique frequently used to satisfy the assumption of independence of errors in linear models (Woolrich, Ripley et al. 2001).

2.2.5.5 Dynamic Causal Modeling:

Based upon prior simulations (Radulescu and Mujica-Parodi 2014) and empirical studies (Anderson, Zielinski et al. 2013), we postulated a close relationship between β-signatures and corticolimbic connectivity. We tested this using dynamic causal modeling (DCM). Our ROIs within the corticolimbic circuit were defined from a synthesis of our present results, our previous work with anxiety patients, as well as human and animal published literature of corticolimbic connectivity. We therefore chose the *inferior frontal gyrus* based on strong group differences in β–signatures identified here with PSSI (see *Results*), the *left vmPFC* based on previous analyses of the fear generalization task, which showed a subset of this region to track gradients associated with perceptual similarity to the CS (Greenberg, Carlson et al. 2013, Cha, Greenberg et al. 2014), and the *right amygdala* for its established role in fear conditioning (LeDoux 2003).

To define ROIs for DCM, we first explored IFG-seeded effective connectivity during fear generalization and its association with β-signatures using psychophysiological interaction (PPI) analysis (Friston, Buechel et al. 1997), focusing on the vmPFC and amygdala. A seed region was defined post-hoc from the group differences in β-signatures within the left IFG. A representative time-series was extracted from the IFG by applying a 6 mm-radius sphere centered at the peak β-signature group difference and deconvolved with the hemodynamic response function (HRF). This time-series was multiplied by a regressor for all GS minus baseline, and then reconvolved with HRF. This procedure generated one interaction term representing IFG functional coupling during all GS, as well as individual interaction terms for each condition. The interaction terms were entered into a separate model containing three regressors: the IFG time-series by "all GS vs. baseline" interaction, "all GS vs. baseline", and the unmodulated IFG time-series. We entered the demeaned IFG β-signatures as a regressor and group as a regressor of no interest in a second level (group) general linear model in order to account for the group difference in the IFG β. We tested for correlations between IFG β and functional coupling for the “all GS” condition within the left vmPFC and right amygdala. We corrected for multiple comparisons using a cluster-extent approach, AFNI 3dClustSim, and adjusted a ROI-specific α level ($\alpha = .025$) according to the number of ROIs (2) to achieve a corrected α level of 0.05. We also performed an exploratory voxel-wise analysis to assess the relationship between IFG-seeded effective connectivity and IFG β-signatures across the whole brain.

We then used dynamic causal modeling (DCM) (Friston, Harrison et al. 2003) to test various directional models of the circuit and to evaluate the relationship between the causal connectivity and IFG β-signatures. As a method, DCM identifies directed connectivity among

the nodes; hidden underlying neural populations are modeled from measured hemodynamic activity, and a system of differential equations is constructed to best explain the given behavior. Bayesian model selection (BMS) is used to select the most likely model from a set of user-defined models. Traditional DCM models the inputs of an experimental design; stimuli are treated as perturbations within a system, while stochastic DCM (Daunizeau, Friston et al. 2009) relies on the modeling of hidden inputs. Given that PSSI is a task-agnostic measure of dynamic regulation of a control system, in which stochastic inputs are assumed, stochastic DCM was better suited than standard DCM in identifying consistent models for PSSI results.

As in the PPI analyses, our regions of interest for the DCM were the *left IFG*, *left vmPFC*, and *right amygdala*. The IFG was defined by the PSSI differences between patients and controls reported here – a 6 mm sphere at [MNI: -52, 20, 6]; the vmPFC was defined by the present PPI results, using a 6 mm sphere at [MNI: -10, 40, -16]; given the strong habituation effect we previously reported (Greenberg, Carlson et al. 2013) within this context, and the lack of PPI-specific correlations with IFG β, the right amygdala was defined by the AAL atlas. The regions of interest were defined uniformly across subjects. Time series for DCM were obtained by using SPM8 to compute the first principal component of the time series from all voxels inside each of the three regions of interest, and were adjusted for the effects of interest contrast as specified in 1st level GLM (where GS60±, GS40±, GS20±, CS_P, CS_U, and US onsets were used to define conditions of interest). We tested four models (Fig. 8) that differed in terms of their endogenous connections, including (1) a *fully-connected model* (bilateral endogenous connections between each of the three regions), (2) a model in which *both amygdala and vmPFC modulate the IFG*, (3) a model in which *the IFG has bidirectional connections to both the vmPFC and the amygdala*, and (4) a model in which *the IFG modulates the vmPFC and in which the vmPFC modulates the amygdala*. Each model consisted solely of intrinsic connections (no modulatory influences were tested) (Almeida, Versace et al. 2009, Li, Friston et al. 2014). We used the standard DCM pipeline in SPM8. BMS was used to determine the highest likelihood model from the given model set. We then extracted the individual connectivity strengths from the highest likelihood model and explored whether IFG PSSI was associated with this connectivity.

2.2.5.6 Measurement of Fiber Integrity:

We hypothesized that structural connectivity within the corticolimbic network would be associated with abnormal IFG β-signatures in participants with GAD. To this end, we investigated the relationship between IFG β-signatures and the integrity of the major corticolimbic white matter pathway previously implicated in anxiety disorders (Kim and Whalen 2009, Westlye, Bjornebekk et al. 2011, Hettema, Kettenmann et al. 2012): the *uncinate fasciculus* (UF). We used standard preprocessing steps in FMRIB's Diffusion Toolbox)(www.fmrib.ox.ac.uk/fsl): after skull stripping, we performed corrections for head motion and eddy-currents via reference volume registration. Diffusion tensor parameters, such as fractional anisotropy, were calculated by fitting a tensor model (DTIFIT) in FDT. Finally, for probabilistic tractography, crossing fibers were modeled using Bayesian Estimation of Diffusion Parameters Obtained using Sampling Techniques in FMRIB Diffusion Toolbox (Behrens, Berg et al. 2007). As described previously (Cha, Greenberg et al. 2014), we reconstructed the entirety of the UF using a global tractography approach, TRACULA (Yendiki, Panneck et al. 2011). From the reconstructed UF (i.e., posterior distribution maps) in each individual, average

fractional anisotropy (FA) values (per hemisphere) were derived. We then tested for correlations between IFG β-signatures and FA of the UF.

2.2.5.7 Summary of Statistics:

Group differences in β-signatures were examined using voxel-wise two sample t-tests. Independent variables included group and subject, while individual β images were used as dependent variables. To minimize bias, group differences in ACF b-values were examined using the same general linear model approach and t-contrasts in SPM as in the PSSI group differences analysis. Pearson's correlation was used to test for an association between IFG β-signatures and MASQ-GDA anxiety subscales, connection strengths from DCM, as well as FA of the UF. Partial correlations were used to control for confounding effects, as noted.

2.3 Results

2.3.1 Inferior frontal gyrus functional dynamics are more random in GAD.

Compared with HC, patients with GAD exhibited IFG β signatures that were significantly closer to white noise ($\beta_{controls} = 0.45 \pm 0.21$; $\beta_{GAD} = 0.28 \pm 0.18$; **Figure 2.2a, b**) at ROI corrected $p < 0.05$ (peak $t(55) = 4.46$; peak $p = 0.00002$). Furthermore, the mean autocorrelation lifetime τ(s) of IFG activity was significantly reduced in patients vs. controls at corrected $p < 0.05$ ($\tau_{controls} = 2.88$s, $\tau_{patients} = 2.50$s; peak $t(55) = 4.12$; peak $p = 0.00007$; **Figure 2.2c**). These results indicate greater randomness of the IFG BOLD time series in patients with GAD compared with HC, an index of either stronger excitatory chaotic inputs or weaker constraints imposed by negative (inhibitory) feedback within the system(Radulescu and Mujica-Parodi 2014). We found no significant differences between patients with GAD and those comorbid with major depressive disorder ($p = 0.43$, two-sample t-test).

We then tested for an association between IFG β and anxiety symptom measures. We extracted subject-wise average β-signatures from a sphere (radius = 6 mm) centered on the peak voxel within the IFG and found that IFG β was negatively associated with self-reported anxiety, as measured by MASQ GDA ($r = -0.39$, $p = 0.004$; Pearson's correlation; **Figure 2.3**). This effect was robust to differences in both group and self-reported depression (MASQ GDD) (partial correlation, controlling for group and MASQ GDD subscale, $r = -0.29$, $p = .04$), and was not specific to either patients or controls (Pearson's correlation, group-wise, p's > 0.15). These findings suggest that IFG β-signatures map onto individual variability in anxiety across a broad continuum of anxiety levels.

2.3.2 Inferior Frontal Gyrus β-signatures correlate with effective connectivity between prefrontal and limbic regions.

We used dynamic causal modeling (DCM) to examine the neurobiological circuitry underlying observed β-signature differences in the IFG of patients vs. controls. As motivated by previous work (Greenberg, Carlson et al. 2013, Cha, Greenberg et al. 2014), our ROIs for DCM included: the *inferior frontal gyrus*, *left vmPFC*, and *right amygdala*.

We first used PPI analysis to define ROIs whose connectivity with the IFG (modulated by generalization stimuli) is associated with IFG β-signatures. We found a significant positive relationship between IFG β signatures and IFG connectivity with the left vmPFC (**Figure 2.4**, **Table 2.2**); IFG connectivity with the amygdala showed no significant association with IFG β-signatures. We also found positive associations between IFG β-signatures and IFG-seeded

connectivity (modulated by GS) with the *ventrolateral prefrontal cortex*, *bilateral caudate*, and the *bilateral mid-temporal lobes* at corrected p's < 0.05 (**Figure 2.4, Table 2.2**). No group differences in IFG-seeded functional connectivity were observed (p's > 0.1) in any of these regions.

Using dynamic causal modeling, we tested four models, which represented a synthesis of the present results as well as our previous empirical and modeling work highlighting the roles of the IFG (Tolkunov, Rubin et al. 2010, Mujica-Parodi, Carlson et al. 2014), vmPFC (Cha, Greenberg et al. 2014), and amygdala (Tolkunov, Rubin et al. 2010, Radulescu and Mujica-Parodi 2014). Bayesian model selection indicated that the fully connected model best supported the empirical results; this model consisted of bidirectional endogenous causal connectivity between the three ROIs (**Figure 2.5**, **Table 2.3**). We found significant correlations between IFG β-signatures and vmPFC→IFG connectivity (r = 0.37, p = 0.007) and IFG→vmPFC connectivity (r = 0.43, p = 0.001); here, greater positive bidirectional connectivity with the vmPFC was associated with less randomness in left IFG time-series. The correlation between IFG→vmPFC and vmPFC→IFG connectivity was significant (r = 0.95, p < 0.001), indicating a highly reciprocal relationship. BMS selected the fully connected model for both patients and controls, and there were no group differences in connection strength for any of the six connections (two-sample t-test, p's >> 0.1). Inter-node connection strengths ranged from -0.005 Hz (L. vmPFC → R. Amygdala) to 0.06 Hz (L. IFG → R. Amygdala), and all connection probabilities reached significance within the DCM construct (connection probability ≅ 1) — consistent with values cited in the literature (Ma, Steinberg et al. 2014).

2.3.3 Inferior Frontal Gyrus regulation (PSSI) correlates with fiber integrity of the prefrontal-limbic white matter pathway.

Finally, we tested whether the observed β-signatures were associated with integrity of the major white matter pathway connecting the IFG with subcortical regions. We found a significant positive relationship between FA (fiber integrity) of the UF and IFG β signatures (r = .30; p = .03; **Figure 2.6**). White matter integrity did not significantly correlate with anxiety or depression subscales (p's > 0.7), though we previously reported a trend towards higher FA in controls than patients within this dataset (Cha, Greenberg et al. 2014). Nonetheless, this effect was significant after controlling for the effects of group, anxiety (MASQ-GDA), and depression (MASQ-GDD; r = 0.28, p = 0.05).

2.4 Discussion

We found that aberrant IFG dynamics replicated results that we first identified for trait anxiety (Tolkunov, Rubin et al. 2010) in both clinical anxiety and with anxious symptoms identified by the MASQ (suggesting an anxiety spectrum approach to be appropriate), and that this shift in functional dynamics was associated with altered functional and structural corticolimbic connectivity within the circuit comprising the IFG, vmPFC, and amygdala. Specifically, IFG functional dynamics were strongly associated with bidirectional interactions with the vmPFC, while the vmPFC exhibited inhibitory causal influence upon the amygdala, a well-established excitatory node within the corticolimbic network (LeDoux 2003).

Using modeling and simulations, we previously showed that dynamics for a node within a negative feedback loop become more random, or 'white,' under two conditions: *when excitatory inputs are strengthened*, or *when negative feedback is weakened* (Radulescu and Mujica-Parodi

2014). Our previous GLM analyses (Cha, Carlson et al. 2014, Cha, Greenberg et al. 2014), as well as current PSSI and DCM, provide converging evidence specifically for the latter, and support a role for the IFG that is indirectly inhibitory (via interactions with the vmPFC, which inhibits the amygdala) rather than directly inhibiting the amygdala. This structure is consistent with non-human primate tracing, which shows extensive anatomical connections from the IFG to the vmPFC, which in turn innervates to and from subcortical limbic areas (Barbas and Pandya 1989). In our task, we employed fear conditioning to induce fear to a particular stimulus (CS), and then presented stimuli across a gradient of perceptual similarity to that stimulus; these ranged from identical (CS) to clearly distinct (± 60%), with more ambiguous stimuli in between. We previously showed that, for health individuals, both the vmPFC and ventral tegmental area (VTA) closely track the gradient of perceptual similarity to the CS. The VTA is strongly activated to the CS, and becomes gradually less activated as cues show greater dissimilarity to the CS (Cha, Carlson et al. 2014). In contrast, the vmPFC follows the opposite pattern, showing strongest activation to the cue most dissimilar to the CS (± 60%), and becomes gradually less activated as cues show greater similarity to the CS (Greenberg, Carlson et al. 2013). These patterns are consistent with the VTA's role reinforcement learning in response to positive or—in the present case—negative reward (Cha, Carlson et al. 2014, Hennigan, D'Ardenne et al. 2015), and also suggests that the vmPFC's role must be primarily inhibitory (Motzkin, Philippi et al. 2015)(i.e., the 'brakes' are off when the cue indicates alarm, but are activated in direct proportion to the likelihood that the cue is deemed 'safe'). This interpretation of the GLM analyses is supported by our current DCM results **(Table 2.3)**, which indicated that the only negative effective connectivity observed was from the vmPFC to the amygdala.

But how does the brain decide what is 'safe' with respect to perceptually ambiguous threat? Here, the IFG seems to be playing a key role. Looking at a spectrum of threat assessment that included 137 individuals, across three independent studies (N=57 for our current study of clinical anxiety, N=50 for our study of trait anxiety (Tolkunov, Rubin et al. 2010), and N=30 for our study of 'reckless' risk-takers (Mujica-Parodi, Carlson et al. 2014)), we observe a clear inverted-U pattern for Brodmann's Area 45, a subset of the IFG. Individuals at the *center* of the threat assessment spectrum (showing accurate perception of threat: *physiologically* in anticipation of jumping out of a plane, *behaviorally* in classifying faces with ambiguous affect, as well as *emotionally* with self-reported low trait anxiety in non-dangerous contexts) showed IFG regulation in the 'pink-noise' range, which our simulations show to occur when a control system includes optimal feedback (Radulescu and Mujica-Parodi 2014), and which our DCM results in the current study linked with strong bi-directional connectivity to the vmPFC. However, individuals at both *ends* of the spectrum (exceptionally anxious and exceptionally reckless) showed circuit-wide dysregulation localized most strongly to the IFG, with 'white-noise' dynamics. Individuals at each end of the spectrum would appear to be opposites of one another (our clinically anxious sample identified threat where it did not exist, whereas our reckless sample failed to identify threat where it did exist), yet the most prominent feature that they both had in common was a failure to accurately assess ambiguous threat. The fact that both ends of the spectrum also shared in common an IFG disconnected to the rest of the prefrontal-limbic circuit suggests that the IFG's role in fear inhibition is indirect: providing disambiguation of ill-defined stimuli, which informs the (inhibitory) vmPFC. Our interpretation is consistent with our DCM results, which provide evidence for a fully connected (closed-circuit) model, with the altered IFG dynamics found in anxious patients most strongly reflecting interactions between the IFG and vmPFC—but not between the IFG and amygdala, or between the vmPFC and amygdala.

The dissociation of roles within the circuit is also supported by the wider human neuroimaging literature. A Neurosynth (www.neurosynth.org) meta-analysis of 272 fMRI studies of 'fear' alone implicate the vmPFC (Z=4.67; x=0, y=44, z=2) but not the IFG; while 94 fMRI studies of 'ambiguous' cues alone implicate the left IFG (Z=4.68; x=46, y=32, z=10) but not the vmPFC. Indeed, the IFG is most commonly implicated in ambiguity not only of fear (Bach, Seymour et al. 2009), but also of semantics (Bozic, Tyler et al. 2010, Rodd, Johnsrude et al. 2012). It thus seems to play a more general role in the evaluation and disambiguation of stimulus *meaning,* a function that is impaired in anxious patients who may live in a state of constant alarm because they do not distinguish well between cues that genuinely signal threat, from those that do not (Lissek, Biggs et al. 2008, Lissek, Rabin et al. 2009, Lissek, Rabin et al. 2010, Greenberg, Carlson et al. 2013, Cha, Carlson et al. 2014).

2.5 Chapter 2 Figures and Tables

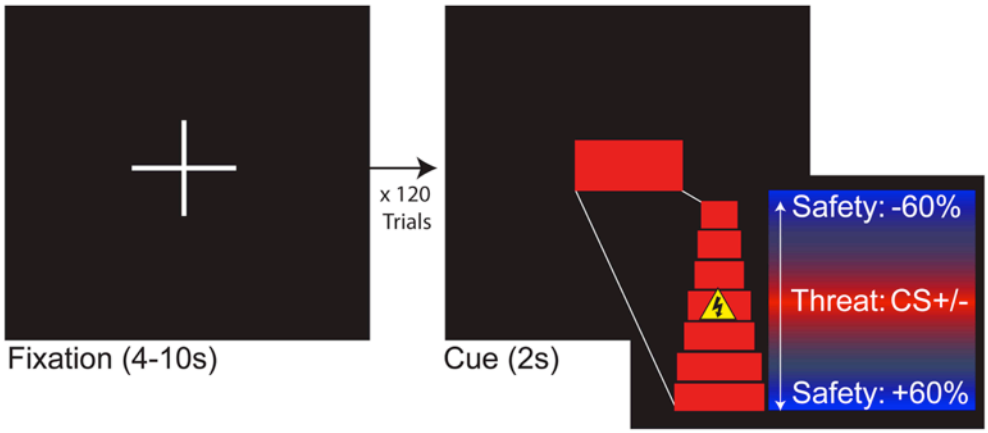

Figure 2.1: Fear Generalization Task.

Participants (N = 57; n = 32 patients with generalized anxiety disorder, GAD) were instructed that they would be shown a red rectangle, which would be paired with a 50% probability of electric shock to the forearm (conditioned stimulus, CS). During fear conditioning, participants viewed five pseudorandom presentations of the CS, paired with a shock each time, and six alternative stimuli (generalization stimuli, GS), which varied systematically in width from the CS (±20%, ±40%, ±60%) and indicated no shock (conditioning phase, not shown). The fMRI task proceeded the conditioning phase. During the task, there were 15 pseudo-random presentations of each stimulus, resulting in 120 total trials; the task employed a 4-10s (jittered) inter-stimulus interval with fixation cross and 2s stimulus presentation. GS were grouped by similarity to CS (i.e., ±20 were analyzed as one condition, as were ±40 and ±60).

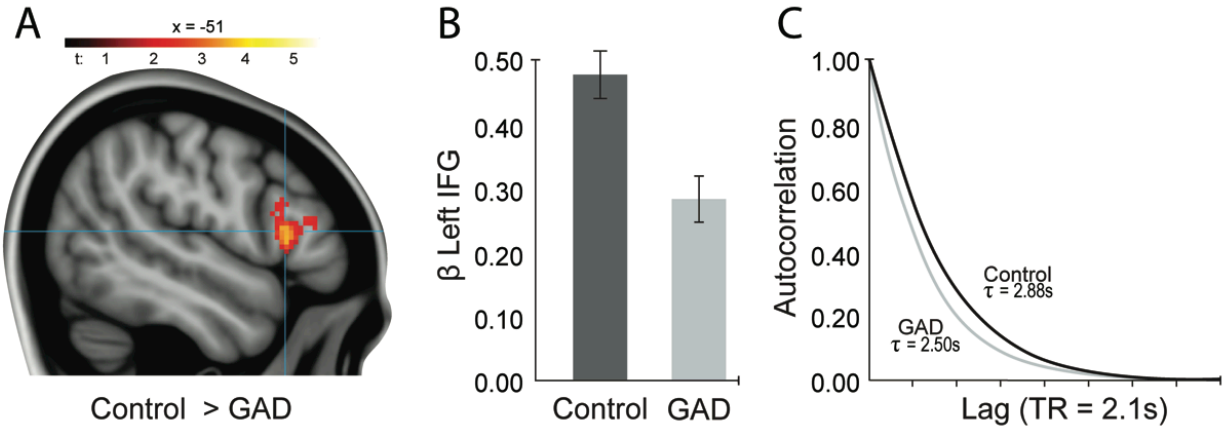

Figure 2.2: Prefrontal Functional dynamics are altered in GAD.

During fear generalization, patients with Generalized Anxiety Disorder (GAD) showed functional dynamics within the inferior frontal gyrus (IFG) that were significantly more random (uncontrolled) than those of healthy controls. We quantified dynamics by power spectrum scale invariance β signatures, which provide the slope of time-series fit to a power-law, as well as autocorrelation lifetime τ, which indicates temporal range of time-series' self-similarity—a measure of memory due to negative feedback within the system. ***(A, B)*** Patients with GAD showed power spectrum scale invariance significantly closer to white noise (β=0) within the IFG ([MNI: -52 20 6]; p(uncorrected) = 2×10^{-5}; cluster extent = 57 voxels; p(corrected) < .001). ***(C)*** Patients with GAD exhibited significantly shorter τ than controls ([MNI: -54 18 18]; p(uncorrected) = 7×10^{-5}; cluster extent = 57; p(corrected) < 0.001) for the same region.

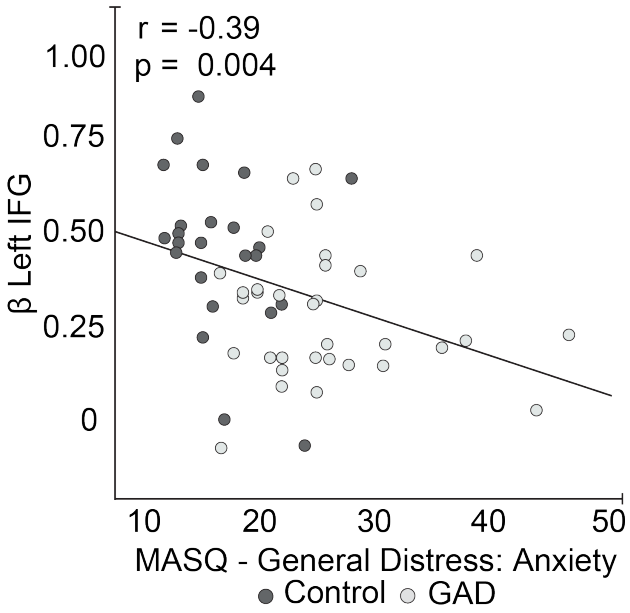

Figure 2.3: Functional dynamics in the IFG are predictive of anxiety.

Power-law β-signatures of the inferior frontal gyrus (IFG) were negatively correlated with self-reported anxiety measures (Mood and Anxiety Symptom Questionnaires (Watson, Weber et al. 1995), General Distress: Anxiety (MASQ-GDA)), an effect that was not specific to either patients diagnosed with Generalized Anxiety Disorder or healthy controls alone (p's > 0.15). This effect remained significant after controlling for both group and depression (MASQ-GDD; r = -0.29, p = 0.04).

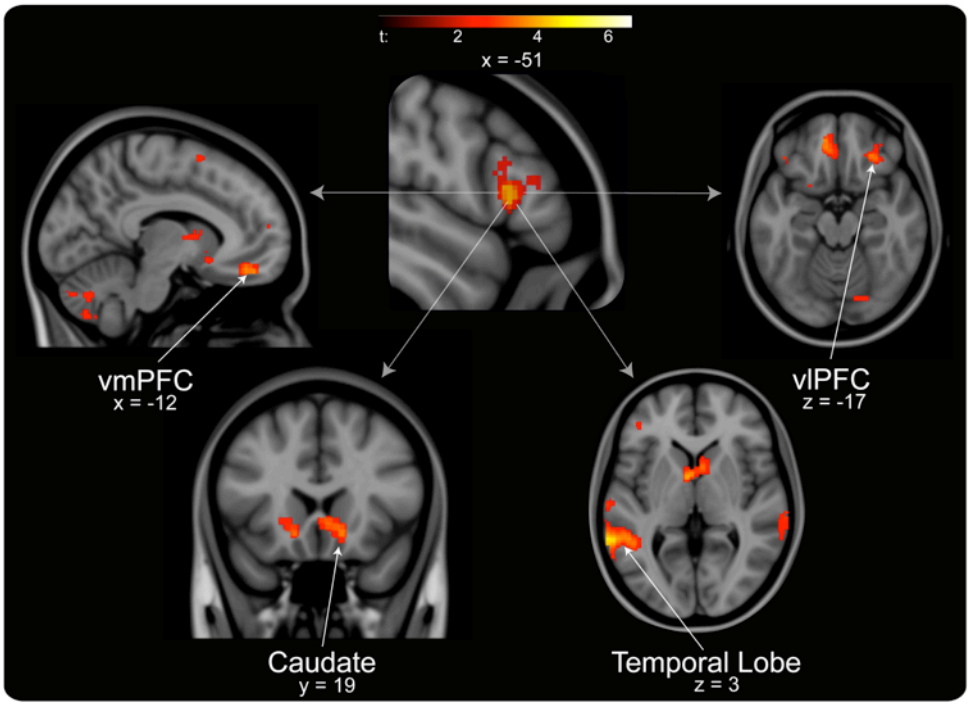

Figure 2.4: Correlation between inferior frontal gyrus (IFG) PSSI β-signatures and effective connectivity modulated by generalization stimuli (GS).

Using psychophysiological interaction analyses, we found that IFG β-signatures significantly correlated with the GS-induced IFG connectivity with the ventromedial and ventrolateral prefrontal cortices (vmPFC and vlPFC), caudate, and temporal lobe.

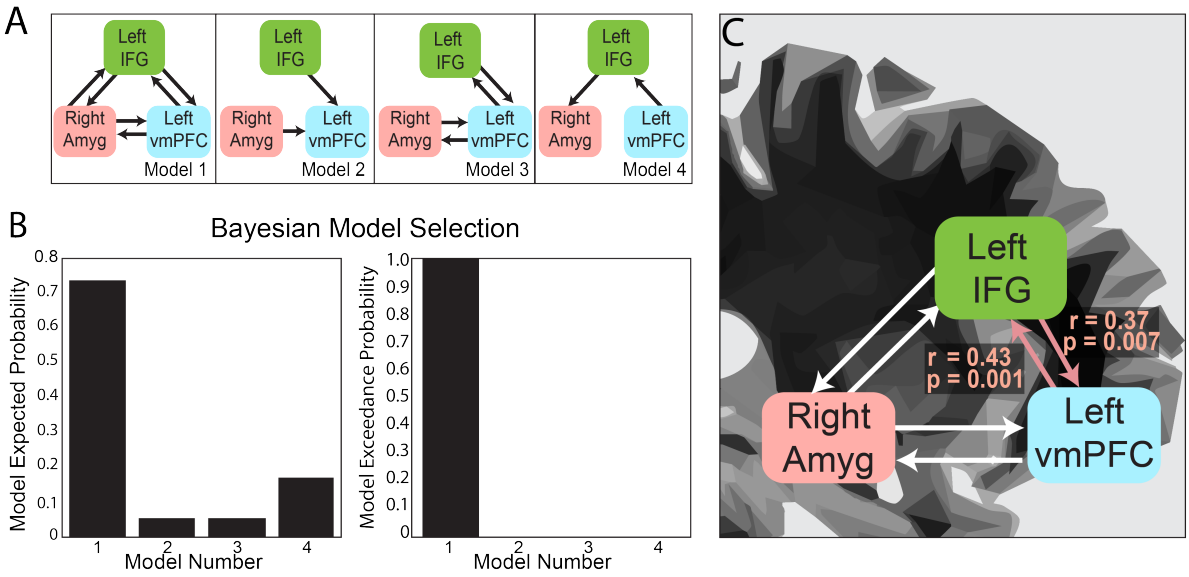

Figure 2.5: Dynamic causal modeling suggests altered connectivity underlies functional dynamics.

Stochastic dynamic causal modeling (DCM) suggests a circuit consisting of the inferior frontal gyrus (IFG), ventromedial prefrontal cortex (PFC), and amygdala during fear generalization. ***(A)*** Model space. ***(B)*** In Bayesian model selection, Model 1 (a fully connected model) showed the greatest expected probability and exceedance probability. All connections within tripartite model 1 were significant (connection probability ≅ 1). ***(C)*** Individual variability in bidirectional connectivity between the IFG and vmPFC significantly correlates with IFG β-signatures. See Table 3 for connection strengths.

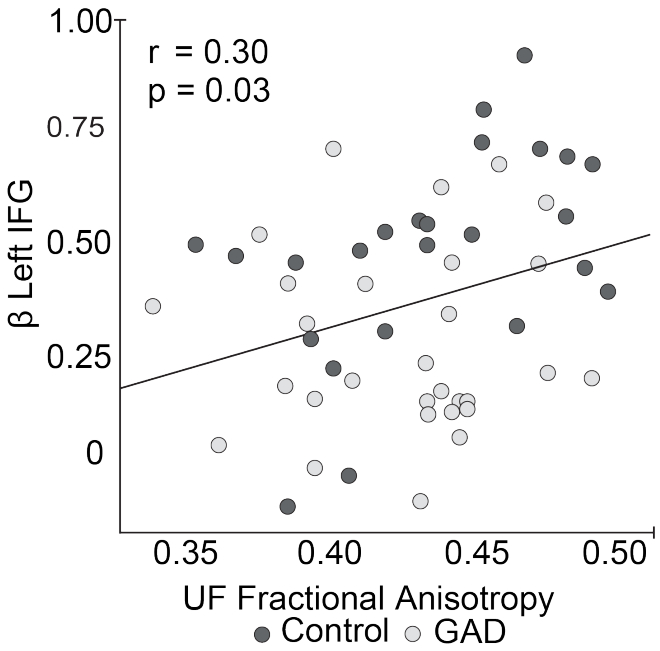

Figure 2.6: Functional dynamics correlate with structural connectivity.

β-signatures of the inferior frontal gyrus (IFG) significantly correlate with the integrity of a major white matter tract in the corticolimbic circuit, the uncinate fasciculus (UF). We used diffusion tensor imaging and an automated tractography approach (TRACULA) to compute the fractional anisotropy (a proxy for white matter integrity) of the UF. This effect remains significant after controlling for the effects of group, anxiety (MASQ-GDA), and depression (MASQ-GDD; $r = 0.28$, $p = 0.05$).

Table 2.1 Demographic and Clinical Data for Patients with Generalized Anxiety Disorder (GAD) and Healthy Controls (HC).

Group	GAD	HC	*t* Value	*p* Value
Age (SD)	22.3 (5.2)	21.5 (5.2)	0.63	.58
Weight	130.0 (18.8)	142.2 (27.0)	1.93	.06
MASQ[1] GDA[2]	26.5 (7.4)	16.8 (4.1)	5.73	< .0001
MASQ DD[3]	35.5 (12.1)	17.9 (3.6)	6.81	< .0001
MASQ AA[4]	28.8 (9.2)	20.8 (3.9)	4.03	.0002
MASQ AD[5]	76.0 (15.4)	53.3 (11.6)	6.01	< .0001

[1] Mood and Anxiety Symptom Questionnaires (MASQ)(Watson, Weber et al. 1995), [2]General Distress Anxiety Subscale, [3]Distress Depression, [4]Anxious Arousal, [5]Anhedonic Depression.

Table 2.2 Power-law β-signatures within the IFG are positively associated with functional coupling.

		Peak		MNI		
Region	**Extent**	***p*(unc)**	***p*(cor)**	**x**	**y**	**z**
L. Temporal Lobe	659	1×10^{-6}	<.001	-66	-46	4
R. Temporal Lobe	210	3×10^{-4}	<.001	66	-40	-4
R. Caudate	143	8×10^{-6}	<.001	-4	2	4
L. ventromedial PFC	125	4×10^{-5}	<.005	-10	40	-16
R. ventrolateral PFC	97	7×10^{-5}	<.01	28	34	-18

Table 2.3. DCM connectivity

DCM connection strengths for a fully connected tripartite model, consisting of the inferior frontal gyrus (IFG), ventromedial prefrontal cortex (vmPFC), and amygdala. All connections are significant within the DCM construct (connection probability ≅ 1). No group differences in any connection strength were found (p's > 0.1).

Connection			Strength (Hz)
L. IFG	→	L. vmPFC	0.02
L. IFG	→	R. Amygdala	0.06
L. vmPFC	→	L. IFG	0.02
L. vmPFC	→	R. Amygdala	-0.005
R. Amygdala	→	L. IFG	0.03
R. Amygdala	→	L. vmPFC	0.01

CHAPTER 3

3. The development and validation of a dynamic phantom for fMRI

Preface

Portions of this chapter have been reproduced from the provisional patent application:

Daniel James DeDora, H.H. Strey, L.R. Mujica-Parodi, "A dynamic phantom for fMRI." *Provisional patent, in filing.*

The authors listed in the above manuscript have contributions towards the data reported in this chapter.

3.1 Introduction

Functional magnetic resonance imaging is a well established method of studying cognition (Luk, Green et al. 2011), emotion (Ochsner, Silvers et al. 2012), and disease (L, D et al. 2012). fMRI signal changes generally comprise a combination of three components: 1) changes in oxygenated and deoxygenated blood following neural activity (the hemodynamic response), 2) physiological noise sources, including heartbeat, breathing, and motion, and 3) scanner instabilities. Novel fMRI methods are typically validated with human imaging data. However, human data lack a "ground truth," in that fMRI methods attempt to interpret an *output* (changes in fMRI signal) without direct knowledge of the *input* (i.e., neural-activity-triggered hemodynamics). With the continued development of sophisticated acquisition (parallel imaging) and analysis techniques (complexity and connectivity), the need to tease apart the separate components of fMRI signal has grown considerably in recent years. While a great deal of attention has been devoted to the study of physiological noise in fMRI (Triantafyllou, Hoge et al. 2005, Triantafyllou, Hoge et al. 2006, Barry, Klassen et al. 2008, van Houdt, Ossenblok et al. 2010, Triantafyllou, Polimeni et al. 2011, Birn 2012, Lutti, Thomas et al. 2013), the study of scanner instabilities has received considerably less attention. Meanwhile, significant scanner-related differences within multi-center datasets have been well documented (Friedman, Glover et al. 2006, Friedman, Stern et al. 2008, Rubin, Fekete et al. 2013). These reports demonstrate the need for further study of scanner instabilities and their influence on the fidelity of dynamic fMRI signals.

One strategy to address the gap between fMRI input and output is to use simulations. Simulations of blood-oxygen-level-dependent (BOLD) fluctuations, scanner instabilities, and eddy currents can be used to better understand and test the ability of analysis techniques to dissociate neural activity from noise (Drobnjak, Gavaghan et al. 2006, Erhardt, Allen et al. 2012, Radulescu and Mujica-Parodi 2014). While simulations offer a wide breadth of applications, oversimplification of complex processes (Renvall and Hari 2009) and fragmentation of model parameters (Erhardt, Allen et al. 2012) can bias models. Another strategy to address the input-output gap in fMRI has been the development of physical fMRI phantoms. A standard fMRI phantom is a sphere of water or doped liquid, allowing an operator to study stability of an fMRI signal over time (Zarahn, Aguirre et al. 1997). These phantoms are suitable for both simple calibration and quality assurance routines. However, these phantoms cannot be used to study to degree to which dynamic input signals are captured by the fMRI, and therefore are of limited used in this context.

Thus, several groups have developed functional MRI phantoms capable of dynamically changing fMRI signal intensity to mimic BOLD signals. These phantoms produce a known, dynamic, BOLD-like signal and experience scanner instabilities in the absence of physiological noise, therefore allowing the dissociation of scanner noise and BOLD. Most of these designs utilize current-carrying wire, capable of distorting small areas of the magnetic field surrounding a gel (Cheng, Zhao et al. 2006, Renvall, Joensuu et al. 2006, Li, Reza et al. 2007, Renvall 2009, Renvall and Hari 2009) or polarized hydrocarbon (Qiu, Kwok et al. 2014). BOLD phantoms have been utilized to correct for aliasing when estimating the hemodynamic response functions in human data (Li, Reza et al. 2007), and in the study of transient fMRI signals (Renvall and Hari 2009). While these designs offer flexibility and well-controlled fMRI signal changes, they utilize conductive materials widely known to be MR-incompatible; this is especially true at high fields. Furthermore, magnetic field distortions vary spatially as a function of r^2, lending uncertainty to results. According to these shortcomings, Olsrud et al. (Olsrud, Nilsson et al. 2008) developed a

simple fMRI phantom utilizing agarose gels; in this study, a transversely divided cylinder was filled with two calibrated agarose gels with slightly different concentrations and, thus, different relaxation constants. The divided cylinder was placed within a larger, homogeneous cylinder containing a single agarose gel, and was slid back and forth between two positions by hand. While successful in creating changes in fMRI signal, this phantom lacked automation and required the removal of motion-corrupted images. Therefore, there remains a need for an automated, fully MR-compatible dynamic phantom that is capable of complex inputs.

Accordingly, we describe the development and validation of a novel dynamic BOLD phantom for fMRI. The phantom is fully automated, contains only plastics and agarose gels, and produces a relatively large activation area spanning multiple slices. We validate the phantom by exploring potential artifacts, presenting representative time-series, and utilizing a trigger-averaging routine to extract a physically simulated hemodynamic response.

3.2 METHODS

3.2.1 Engineering constraints

A dynamic phantom has been designed with the following engineering constraints, as determined by thorough literature review:

i) Production of controlled and versatile fMRI signal (i.e., capable of producing complex waveforms).
ii) Full fMRI compatibility - no circuitry, metals, or paramagnetic materials.
iii) Full automation for precise reproducibility – removing sources of human error.
iv) Inexpensive to fabricate and mass-produce for widespread adoption.
v) Modular design – for design flexibility and easy upgrades.

3.2.2 Design strategy

Olsrud et al. (Olsrud, Nilsson et al. 2008) developed a hand-cranked phantom to show that dynamic fMRI signal could be achieved by sliding different concentrations of agarose gels in and out of a region of interest. The magnetic susceptibility of agarose gels is concentration dependent (Christoffersson, Olsson et al. 1991, Cheng, Zhao et al. 2004, Ebrahimi, Swanson et al. 2010), and this created changes in T2* within a given voxel or region. Utilizing this premise, we designed, fabricated, and validated a novel dynamic phantom for fMRI. This new dynamic phantom is fully automated, capable of complex waveforms, and contains no paramagnetic materials.

The dynamic phantom is composed of calibrated agarose gels housed within two concentric cylinders. The outer cylinder contains a "baseline" gel, while the inner cylinder is longitudinally divided with both (*i*) a baseline gel matching the outer cylinder and (*ii*) an "active" gel with slightly lower concentration of agarose. The longitudinally divided inner cylinder produces dynamic fMRI signal via rotation about its long axis. We developed a novel fMRI-compatible pneumatic motor to drive rotation of the inner cylinder, while the outer cylinder remains motionless. Position of the inner cylinder is continuously monitored with a fiber optic feedback system, and the device is operated from the fMRI control room with a microcontroller. Compressed air drives rotation of the inner cylinder, and monitoring of the phantom occurs through plastic fiber optic cables, which run between the scanner and control room.

Thus, the dynamic phantom is comprised of two main systems: 1) the scanned phantom, consisting of two concentric cylinders and supports, a plastic gearbox, tubing, and fiber optic cables, and 2) the control unit, consisting of a microcontroller, compressor, and circuit board. The description of the design will be broken down within these two systems and their interface. **Figure 3.6** details phantom operation in its entirety.

3.2.3 Agarose Gels and materials justification

We first fabricated calibrated agarose gels for precise control of T_2^* production (**Figure 3.1**). Agarose was chosen as a contrast medium because of its relative ease of use, flexibility in preparation, and temporal stability. The use of agarose in phantom construction has been validated throughout the literature, and it is shown to be homogenous with respect to MR relaxation properties (Christoffersson, Olsson et al. 1991, Olsrud, Nilsson et al. 2008). First, we measured the relaxation properties of agarose gels (**Figure 3.1**) at various concentrations. Consistent with the literature, we found that agarose exhibits grey matter-like T2* relaxation properties at concentrations between 2-3%. Thus, to be consistent with prior work, the outer cylinder was filled uniformly with 2.27% agarose. The inner cylinder was filled with 2.21% and 2.27% agarose gels. No dividing materials were used, i.e., the gels were in direct contact. These concentrations were chosen to closely match previous agarose phantom work (Olsrud, Nilsson et al. 2008), but with the goal of creating more biologically feasible fMRI signal changes of 1-2%. Gels were degassed with a vacuum chamber.

3.2.4 Phantom Housing

We used AutoCAD (AutoDesk, Inc) to design a cylinder-within-cylinder phantom (**Figure 3.2**). The inner cylinder contains four compartments, divided longitudinally (in contrast to the traverse compartmentalization of Olsrud (Olsrud, Nilsson et al. 2008), as in **Figure 3.3**). All custom phantom parts were printed with a Makerbot 3D printer with "natural" color polylactic acid filament (Makerbot, Inc, Brooklyn, NY). The volume of the outer cylinder was 600 mL, while the volume of the inner cylinder was 150mL.

3.2.5 Control and automation

To achieve automated rotation of the inner cylinder, we designed and fabricated a fully fMRI compatible pneumatic motor system. The motor consists of a compressor, valves, manifold, tubes, dual fans, and a gearbox. An air compressor is placed in the control room of the fMRI center; input pressure is set to 40 pounds per square inch at 1.9 cubic feet per minute. Plastic tubing guides the compressed air through a splitter and into two Arduino® controlled solenoid valves (Sparkfun, CO). Compressed air leaves the two independent valves and is guided through two tubes into the scanner bed.

Finally, the compressed air is released from the pairs of tubes via pneumatic connectors, resulting in high velocity airflow. Depending on which valve is open, this airflow powers one of two fans; these fans are coupled to a gearbox and spin in opposing directions. The dual fan setup allows the gearbox to be driven in either direction and also allows precise braking. The rapid rotation of the fans is stepped down and torque is increased via five 3:1 compound gears, resulting in a step down ratio of 243:1. The gearbox ultimately interfaces with the inner cylinder and optical interruption disk to produce pneumatically controlled rotation. The outer cylinder does not rotate.

3.2.6 Fiber optic feedback

We designed a fiber-optic feedback system using plastic fiber-optic cables, an LED light source, a photodiode, and an interrupter disc (**Figure 3.4**). An Arduino microcontroller powers a high-powered 10 mm LED (Spark Fun, CO), which is coupled with a 1.5 mm diameter fiber optic cable (Thor Labs, NJ). The first cable guides light from the LED source within control room to the scanner bed through a waveguide. The fiber optic cables are positioned opposite each other and spaced 5mm apart, such that as the phantom rotates, the interrupter disk (3mm thickness) will intermittently block light transmission between the two cables. The second fiber optic cable receives light and is fed back to a photo-diode on the microcontroller. As the interrupter disc spins, the photo-diode receives differential intensity readings. The microcontroller then displays the interruption count as a live feed at each TR. Prior to each fMRI scan, the device performs a self-calibrating procedure to ensure optimal position encoding regardless of ambient light. The interrupter disc has 60 teeth, corresponding to ~6^{o} of rotation per interrupt. Empirical testing with the phantom shows that the phantom is capable of traversing between 0.5 and 1.5 interruptions per TR, with one interruption being average.

3.2.7 Arduino microcontroller and fMRI communication

TR signals are sent to the Arduino via USB input from the fMRI. To properly calibrate the phantom rotation and avoid motion artifacts in regions of interest, we ran a simple EPI acquisition (TR = 2, TE = 30ms, 25 slice) where the phantom began rotation just after the start of each TR, and examined each slice for motion artifacts. As shown in **Figure 3.5**, severe motion artifacts occur when the phantom is rotating during or before a slice is acquired, whereas slices acquired before the phantom rotates within a TR contain considerably less artifact. Therefore, if the phantom is programmed to begin rotation towards the end of a TR (after a sufficient number of slices have been acquired) and to stop rotation *just before* the next TR, motion artifacts are negligible (see *Results*). Empirical testing with this design suggests that the phantom should begin rotation 650ms prior to each TR, and stop ~100ms before the TR. Thus, for TR = 2s, the dynamic phantom begins rotation at 1350ms and ends at 1900ms.

3.2.M8 Arduino software

The dynamic phantom is controlled with an Arduino Mega ® (www.Arduino.cc). All software was developed in-house. The phantom can operate in three distinct modes: 1) stimulus-driven, 2) guided, and 3) rest.

In **stimulus-driven mode**, the user enters onsets and "amplitudes" of each stimulus. The phantom is programmed to respond to the onset of a "stimulus" by mimicking a simple hemodynamic response function (**Figure 3.3**), with a gradual rise and fall over ~16 seconds. Thus, when the phantom receives an input, it begins rotation towards a designated "amplitude," which corresponds directly to an interrupt number. When the stimulus-specific amplitude is reached, the phantom begins returning to baseline. If another stimulus is received during this cycle, the phantom begins rotation towards the new amplitude. In this way, the dynamic phantom is capable of producing biomimetic fMRI time series.

In **guided mode**, the user enters a desired interruption destination for each TR. The phantom will receive a new instruction (interrupt number) at each TR. This mode is useful for the production of specific time-series, such as a pink-noise time-series.

In **rest mode**, the phantom is used to measure baseline noise levels in the absence of BOLD-like signal. The culmination of these features is a flexible and modular architecture

through which the phantom can be easily made to perform a wide variety of experimental designs.

3.2.8 Experimental paradigm

For this report, the phantom was programmed to follow a simple stimulus-driven paradigm during a series of five-minute scans. We implemented an event-related stimulus-driven design, which consisted of seven "stimuli" separated by 40 seconds each. We chose a simple event-driven paradigm to optimize our acquisition for the analysis of trigger-averaged responses.

3.2.9 Acquisition parameters:

The dynamic phantom was scanned in a 3T Siemens Trio scanner with a 12-channel headcoil at the Stony Brook University SCAN Center in Stony Brook, NY. The acquisition parameters used closely matched our recent work (Greenberg, Carlson et al. 2011, Greenberg, Carlson et al. 2013, Cha, Carlson et al. 2014, Mujica-Parodi, Carlson et al. 2014) - TR = 2000ms, TE = 30ms, flip angle = 83^{o}, matrix = 96 × 96, FOV = 224 × 224mm, slices = 31, and slice thickness = 3.5mm. The DICOM images were converted to 4D NifTi.

3.2.10 Statistical analysis:

We took several steps to validate our dynamic phantom datasets. First, we examined our data for the presence of motion artifacts. "Active" voxels were explicitly designed to produce significant task-specific standard deviations, compared with non-active voxels. Therefore, when examining for motion artifacts, we used a custom script to remove "active" voxels by setting a strict correlation threshold ($r > 0.25$) between raw time series and phantom inputs (optical interrupter reading); we then used binary masks and rank-sum tests to test for differences in standard deviation between non-active inner (moving) and outer (stationary) cylinder voxels.

We extracted several time series from each scan using custom MATLAB software tools. We tested for parametric correlations between phantom input (interruptions from Arduino) and output (fMRI time-series). As a final validation measure, we employed a simple trigger averaging code to "active" voxels, located along the gel-gel interfaces, to demonstrate hemodynamic-response-like signal changes. Where noted, data were band-pass filtered between 0.01 and 0.1 Hz (Rubin, Fekete et al. 2013).

3.3 RESULTS

3.3.1 Calibrated gels

Development of a phantom useful for functional MRI requires calibration of agarose gels for T_2^* relaxation values similar to that of brain matter. We scanned four concentrations of standard agarose gel (**Figure 3.1**), as well as three concentrations of high-strength agarose (1.0%, 2.0%, 3.0%) to evaluate relaxation time of each. Each sample was scanned at TEs increasing in intervals of approximately 10ms from 47ms to 140ms. Short TEs were found to elicit highest signal to noise ratios. We found that we could achieve predictable T_2 relaxation within the range of brain matter (~50-60 ms) (Olsrud, Nilsson et al. 2008) with concentrations of standard agarose between 2.2-2.8%. High strength agarose was found to be difficult to clear of bubbles (which cause image artifacts); therefore, standard agarose was used for our phantom.

3.2.2 Motion artifact mitigation

As an initial proof of concept, we sought to test whether motion artifacts could be avoided via precisely timed rotation of the phantom. First, we explored time-series resulting from our preliminary tests, as described in *Methods* and presented in **Figure 3.5.** After calibrating phantom rotation and acquiring event-driven data, we extracted two representative slices of interest from our phantom volume (slices 6 and 7). Due to the interleaved odd-first slice acquisition, slice 7 was acquired prior to rotation, while slice 6 was acquired post-rotation. For slice 7, rank sum tests between inactive inner cylinder voxels and outer cylinder voxels revealed no significant differences in standard deviation of the signals (SD_{outer} = 13.5, SD_{inner} 14.75, p = 0.894). As expected, slice 6 showed significantly higher standard deviations in the inner cylinder than both the outer cylinder (SD_{inner} = 15.39, SD_{outer} = 13.1, $p < 1 \times 10^{-9}$) and inner cylinder from slice 7 ($p < 1 \times 10^{-3}$). Thus, we showed no evidence for motion artifacts in slices acquired before rotation.

3.2.3 Time-series analysis

Next, we explored phantom data for activated voxels. We extracted time series from within gel-gel interfaces (expected to show activation), as well as time-series from between interfaces and the outer cylinder (not expected to show activation). Results for slice 7 are demonstrated in **Figure 3.7**. As expected, we found that phantom inputs (interrupt readings) were significantly correlated with fMRI data at gel-gel interfaces; these areas displayed signal voxel percent signal change (computed as (Max(X) – Min(X))/Mean(X)) of between 3-7%. Between slices 5 and 12 (excluding slices at the top and bottom edges of the phantom), a total of 3,352 voxels demonstrated correlations ($r > 0.25$) with phantom inputs.

3.2.4 Mimicking the hemodynamic response

As a demonstration of the practical applications of the present dynamic phantom, we sought to test whether the dynamic phantom could produce realistic physical simulations of the biological hemodynamic response function (HRF). If so, the phantom could be used to optimize scan parameters (for example - TR, SMS factor) for the extraction of HRFs in the absence of physiological variables, which are known to reduce intra and inter-scanner reproducibility (Friedman, Stern et al. 2008). We employed a trigger averaging routine to extract the average response function of the phantom following a “stimulus” in stimulus-driven mode. As predicted, the phantom produced a realistic HRF, shown in Figure 3.8.

3.4 DISCUSSION

3.4.1 Summary

This methods paper detailed the development and validation of a dynamic BOLD phantom for fMRI. This phantom is completely MR-compatible, fully automated, and is capable of producing complex inputs to mimic biological hemodynamics. To validate the dynamic phantom, we explored both active and inactive time-series from the inner cylinder, as well as inactive outer cylinder time-series. Finally, we demonstrated a biomimetic hemodynamic response produced with the phantom.

F4.2 Materials and design

We used undoped agarose gels to produce BOLD-like signal changes. Doping these gels could help tailor both T_1 and T_2 relaxation times for specific uses (Olsrud, Nilsson et al. 2008). Additionally, other hydrogels or similar materials may be suitable for use within the dynamic

phantom. For example, poly(dimethylsiloxane) (PDMS) can also be calibrated for specific relaxation properties (Dreiss, Cosgrove et al. 2007).

We developed a custom MR-compatible motor to drive rotation of the phantom. This motor allows for precise rotation in either direction. If necessary, greater flexibility could be afforded by modifying the number of gears and their ratios. Furthermore, inclusion of a geneva mechanism could grant phantom operators an exact amount of rotation per pulse.

Phantom rotation is monitored continuously through an interrupter disc. We chose a 1.5mm diameter fiber optic cable to ensure sufficient illumination was attained with our LED and photodiode setup. The spacing between the teeth of the interrupter disc was designed to closely match the diameter of the fiber optic cable used, ensuring full interruption. Thus, finer control of the phantom could be achieved with a combination of reduced fiber-optic cable diameter and interruption tooth size. Furthermore, the interrupter disc could be replaced with a continuously variable translucent color wheel, which would allow the phantom to be tracked continuously by color.

3.4.3 Mitigation of motion artifacts

The phantom produces BOLD-like signal changes by moving differentially calibrated agarose gels in and out of a volume of interest. In fMRI studies, motion is considered a significant source of noise; many previous studies report reduced connectivity in populations less likely to remain still during fMRI scanning – children, the elderly, and the mentally ill (Power, Schlaggar et al. 2015). Many methods for motion correction have been presented, including standard coregistration, regression (Rubin, Fekete et al. 2013), and removal of affected images (Power, Barnes et al. 2012). Indeed, the hand-cranked fMRI phantom developed by Olsrud et al. (Olsrud, Nilsson et al. 2008) required the removal of images during which movement occurred.

The phantom avoids motion artifacts in regions of interest by precisely timing its rotation to begin 650ms before the onset of a TR, and finish before TR onset. This strategy allows most of the phantom to be imaged without motion-artifacts. Indeed, we found no significant differences between inner and outer cylinder standard deviations in slices acquired before rotation; as expected, significantly higher standard deviations were found in the inner cylinder during slices acquired after rotation onset. It is also important to note that inner cylinder voxels outside of the gel-gel interface that contain air pockets or gel inhomogeneities may experience larger standard deviations than the outer cylinder, due to the passing of these impurities through voxels-of-no-interest. Thus, it is critically important to properly degas phantom cylinders and to ensure gel homogeneity during development of a rotation phantom.

Despite our present focus on avoiding motion artifacts, it should certainly be noted that this phantom is capable of producing motion-related artifacts for the continued study of motion in fMRI signal. For example, the phantom can be programmed to periodically rotate out of sync with fMRI pulses, causing single- or multi-frame motion artifacts (spikes) at designated times within a study. This type of data could significantly improve current models of motion in fMRI (Drobnjak, Gavaghan et al. 2006).

3.4.4 fMRI signal production

At the single-voxel level, we found that the dynamic phantom produced maximum percent signal changes (PSC) of 5% with agarose concentrations of 2.21% and 2.27%. This represents a high but biologically feasible level (Olsrud, Nilsson et al. 2008). fMRI time-series, however, are

typically represented as an average across a region-of-interest. This phantom design utilizes partial volume effects (see **Figure 3.2**) to achieve variable PSC, ranging from nearly 0% (if slightly less than half of the inner cylinder is used as an ROI) to up to 5%. In this way, a wide range of biologically and analytically relevant PSCs are produced.

Here, the phantom was programmed to simulate a hemodynamic response following a virtual "stimulus." The extracted response function closely mirrors the biological hemodynamic response, especially after filtering. The post-stimulus undershoot appearing in the filtered response function is an artifact of filtering, and not an observation of fMRI "transients" discussed by Renvall et al. (Renvall and Hari 2009); here, we found no evidence of transients following changes in fMRI signal. We suggest two possibilities for this. First, the agarose phantom may produce changes in fMRI signal too slowly to reproduce this type of signal artifact. However, the biological hemodynamic response is also slow as compared to neural activity, so speed of fMRI signal change is unlikely to influence transient signal production. Second, the Maxwell coils in Renvall's fMRI phantom could interact with fMRI in unforeseen ways, perhaps briefly storing and releasing small charges in response to rapidly changing RF fields within the headcoil. Further study with the agarose phantom will shed light on this issue.

3.4.5 Important points on phantom design

We gleaned several important lessons from our experiments with this phantom. First, the phantom must be placed perpendicular to the imaging gradient to avoid slice-based signal artifacts. Second, the phantom is particularly sensitive to inhomogeneities and imperfections in the agarose gel. Third, shaking of the fMRI during scanning may induce slight motion artifacts on their own, adding a source of variance to the data. Thus, the phantom should be secured within the headcoil.

3.4.6 Advancements made in SAII.

This report comprised several advancements in the field of fMRI device development, the most notable of which are discussed below.

3.4.6.1 Development of a pneumatic motor.

One of the most challenging parts of a building the first completely MRI compatible dynamic phantom was developing a pneumatic motor. The current design was developed under the following constraints:

1. Full MRI compatibility (plastics/glass only).
2. Precise control and flexibility in operation.
3. Enough torque to rotate a phantom filled with agarose gel.
4. Minimal air pressure requirement - 20-30 PSI max.

Our current design utilizes 3D printed fans and gearing to allow for dual rotation directions and precise motor control. Our phantom is capable of starting to rotate from a stop quickly, and is capable of nearly instant braking using the dual fan system.

Our design is not the only MRI compatible motor on the market. Several years ago, a pneumatic motor was developed for fMRI that utilized sequential and precisely controlled stepper "levers" (Stoianovici, Patriciu et al. 2007). Pneumatic activation of each of these levers in sequence allowed rotation of the motor. However, this motor is considerably more complex than our motor. Additionally, many robot-actuators for MR-guided surgeries are available

(Fischer, Iordachita et al. 2008, Tokuda, Song et al. 2012), which offer considerably more precision. However, our design offers considerably greater simplicity and cost-effectiveness than the current market options.

3.4.6.2 Development of fMRI compatible position encoding system.

In addition to a pneumatic motor, we had to develop a method of tracking the position of the phantom at any given time. Using 3D printing, fiber optics, a high-power LED, and a photodiode in conjunction with an Arduino microprocessor, we constructed a closed-loop position feedback system. The system calibrates itself to ambient lighting conditions, performs a position calibration based on a strategically placed double-interrupt, and proceeds to track the motion of the phantom continuously. The position encoding software was written in Arduino, and can be found in the appendix.

3.4.6.3 Mitigation of motion artifact with precise rotation timing.

In September, 2011, an NIH R21 grant was filed by our group. Reviewers of the dynamic phantom claimed that severe ghosting and motion artifact would plague the design. Our reviewers were correct in that continuous rotation and rotation prior to slice acquisition caused motion artifacts (FIGURE). However, our group was able to mitigate these through precise rotation timing. The potential implications of this discovery are significant. Motion correction algorithms generally examine motion time-series from SPM through a thresholding mechanism. When the magnitude of motion is greater than 3mm or 3^{O}, either the volume is discarded (as in "scrubbing" (Power, Barnes et al. 2012)) or the entire subject is removed from analysis for "excessive motion." Timing of the motion within the imaging volume is typically neglected.

However, the phantom data suggest that when *reasonable* motion of the subject takes place, only slices acquired after the motion took place but before the next volume acquisition are affected. In other words, when studying motion artifacts, it is important to identify the timing *and* extent of motion within a volume. This possibility is beyond the scope of the present work, but further research could address this shortcoming of fMRI.

3.4.7 Potential limitations of the dynamic phantom.

A shortcoming of our present design is that our fiber optic feedback and positioning system is relatively coarse. The interruption disk fins are 2.5mm thick and separated by 2.5mm, meaning that the phantom must travel an angular distance of 5 mm to get from one interruption to the next. This distance requires several TRs to traverse, resulting in coarse-grained "input" curves. This could be addressed in a straightforward manner with a more advanced fiber optic system.

Similarly, the phantom is only capable of creating BOLD-like signal changes as a function of rotation time and speed between TRs; i.e., the phantom can create signal changes only according to the number of degrees it can rotate within the 500ms rotation window. In other words, the phantom is limited in signal changes to a range of *S(max) – S(min)* and it may take several TRs of rotation to change from one extreme to the other. This limitation can be addressed during analysis by restricting the size of the region of interest (ROI) – a smaller region of interest will see more dramatic changes on average compared to a larger region of interest. Additionally, voxels nearer to the interface between gels will see considerably more abrupt changes than those further from the interface.

Another shortcoming of the design is the presence of air pockets in the agarose gel. These pockets create large signal distortions in our images. When paired with motion of the inner

cylinder, this creates areas of artifact, where air travels in and out of a voxel. This shortcoming can be addressed with better degassing during the gelling process.

Despite the many advantages of a rotation phantom design, the rotation phantom produces simulated BOLD signal in a somewhat biologically-irrelevant manner; i.e., the human brain produces fMRI signal changes by changing the local concentrations of oxygenated vs. deoxygenated blood through flow, whereas the phantom produces changes through rotation of two gels. A phantom that properly modeled the activity of the human brain would be useful for the continued development of vasculature-BOLD models (Uludag, Muller-Bierl et al. 2009), among other uses (arterial spin labeling, diffusion tensor imaging, etc).

Finally, the dynamic phantom was limited in size by the surface area of the 3D printer used to prototype the device. A larger outer cylinder (in all directions) would increase the stability of the signal and increase biomimetic capabilities. Additionally, the phantom comprises just a single type of gel, whereas the brain comprises three major tissue types – gray matter, white matter, and cerebrospinal fluid. Incorporation of different materials into the outer cylinder could help enhance the biomimickry of the phantom. Additional incorporation of geometric features, as well as more tightly defined geometries, could help the phantom be used for spatial resolution measures simultaneously with temporal measures.

3.4.8 Conclusion

This chapter comprised the fabrication and validation of an automated, compartmentalized, programmable rotation phantom for fMRI that is capable of producing predictable and reproducible fMRI signal. This project required a combination of 3D printing, open-source electronics, C++ software, a fiber optic feedback system, and agarose gels. The completion of this chapter will serve to enable researchers to answer the fundamental question, "*when physiological noise is removed, to what extent do the fMRI scanner and subsequent data analyses capture the fidelity of an input signal?"* In the final chapter, we use the phantom to begin answering this question.

3.5 Figures and captions

Figure 3.1: Calibrating agarose gels for fMRI contrast.

(A) and (B) show agarose gels at 1.5, 2, 2.5, and 3.0% w/w, at TE = 47ms (A) and 140ms (B). (C) T_2 vs agarose %. The T_2 of grey matter is ~45ms, corresponding to [agarose] ≈ 2.75%. Based on these results and prior work, we decided to use 2.27% agarose for baseline, and 2.21% for the "active" state.

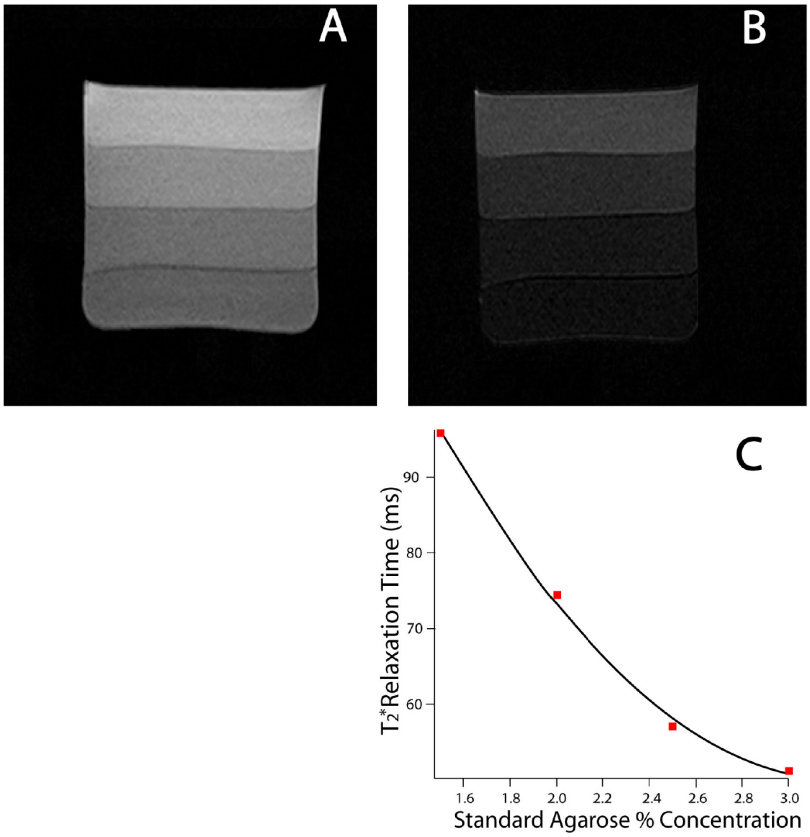

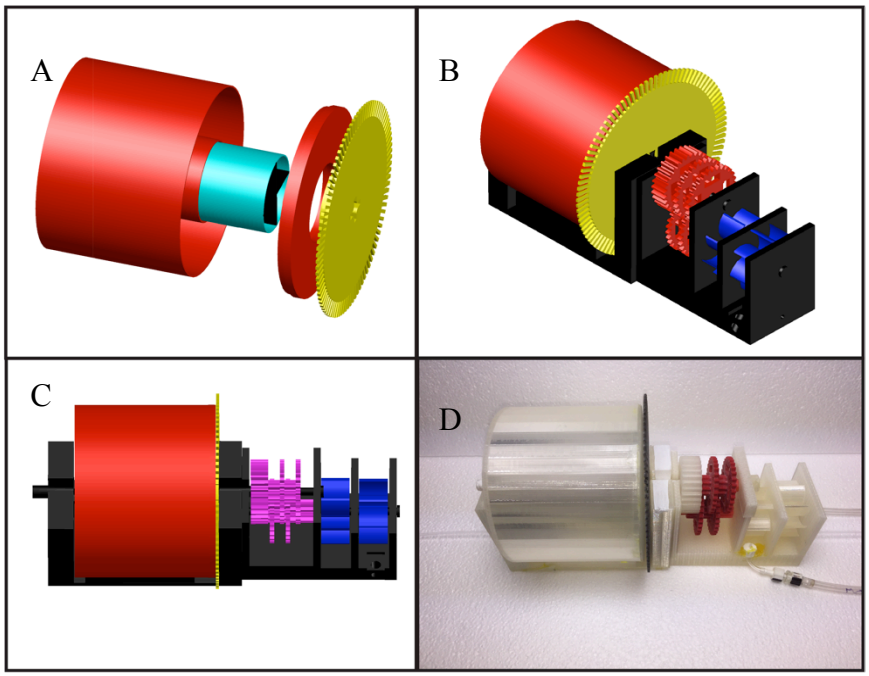

Figure 3.2: Design of the dynamic phantom.

The dynamic phantom is the first automated agarose gel phantom capable of producing dynamic fMRI signal without the use of any metallic components. The phantom comprises a concentric dual cylinder **(A)** design. The inner cylinder is divided longitudinally into four compartments and filled with two calibrated agarose gels with slightly different concentrations. The outer cylinder contains a uniform agarose gel. The inner cylinder interfaces with a pneumatic motor **(B)** and **(C)**, comprising 3D printed fans and gears. Compressed air enters the scanner through tubing **(D)** and drives the fans, which face opposing directions and allow both bidirectional rotation and precise braking. The fans are coupled with a custom 243:1 gearbox, which produces torque necessary to rotate the phantom. An interrupter disk is coupled to the inner cylinder. Plastic fiber optic cables face each other on either side of the interrupter disc. Light from an LED in the control room leaves the first fiber optic cable, enters the second fiber optic, and is guided back to a photodiode. The interrupter disk interrupts the light as the phantom rotates, allowing for position tracking.

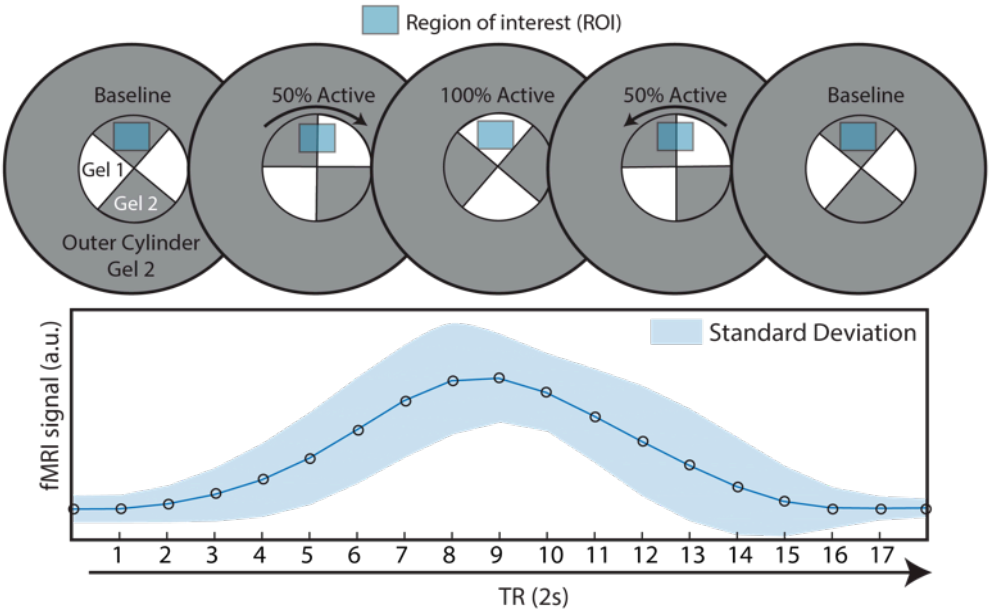

Figure 3.3: Phantom production of pseudo-BOLD.

(top) Conceptual representation of pseudo-BOLD signal production mechanism, and empirically measured signal change **(bottom)**. Automated and precisely timed rotation of the phantom between two calibrated agarose gels within a region-of-interest produces smoothly varying hemodynamic response-like signal changes. Here, agarose gel concentrations were 2.21% (gel 1) and 2.27% (gel 2). Data shown are extracted from a simple event-driven design via trigger averaging with an 18 TR window. Region of interest is a 3 x 3 voxel square.

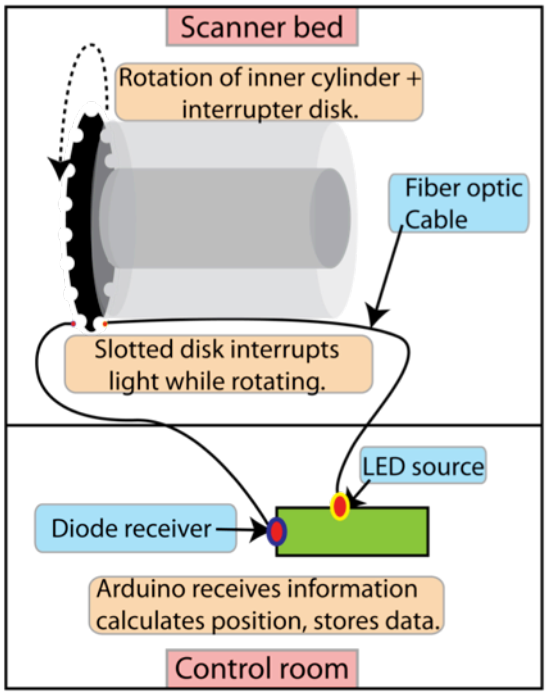

Figure 3.4: Interrupter system.

The smaller inner cylinder (dark gray) is physically linked to the interrupter disk (black). The interrupter disk contains slots, which interrupt the flow of light through fiber optic cables placed on either end of the disk at the bottom of the phantom. The light originates from an LED on the Arduino. Fiber optic cable carries the light from the source, through the interrupter system, and eventually to the diode receiver. This setup allows the Arduino to encode relative position as a function of interruptions.

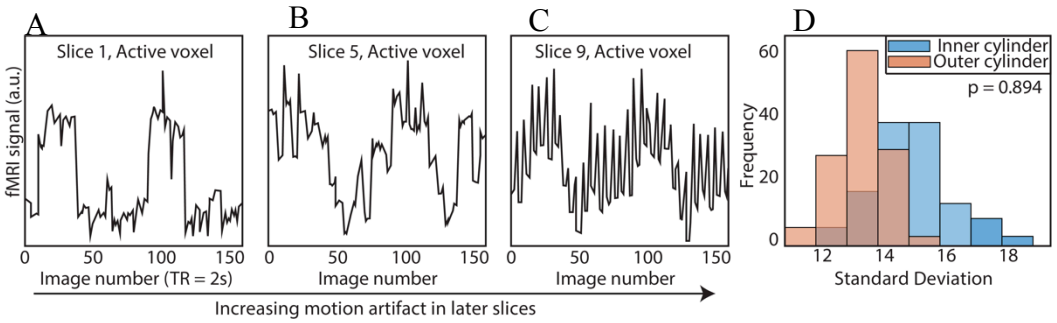

Figure 3.5: Motion artifacts during rotation vs. slice.

The dynamic phantom rotates between 3-6^{o} between TRs. Rotation is coupled with TR acquisition through a microcontroller, and is tightly controlled with a brake. For demonstration purposes, we show here that slices acquired before rotation **(A)** are subject to considerably less spiking than slices acquired during rotation **(B)** and after rotation is completed **(C)**. Accordingly, we optimized our rotation/braking scheme such that inner cylinder voxels contain no significant differences in standard deviation for slices of interest (rank sum test)**(D)**.

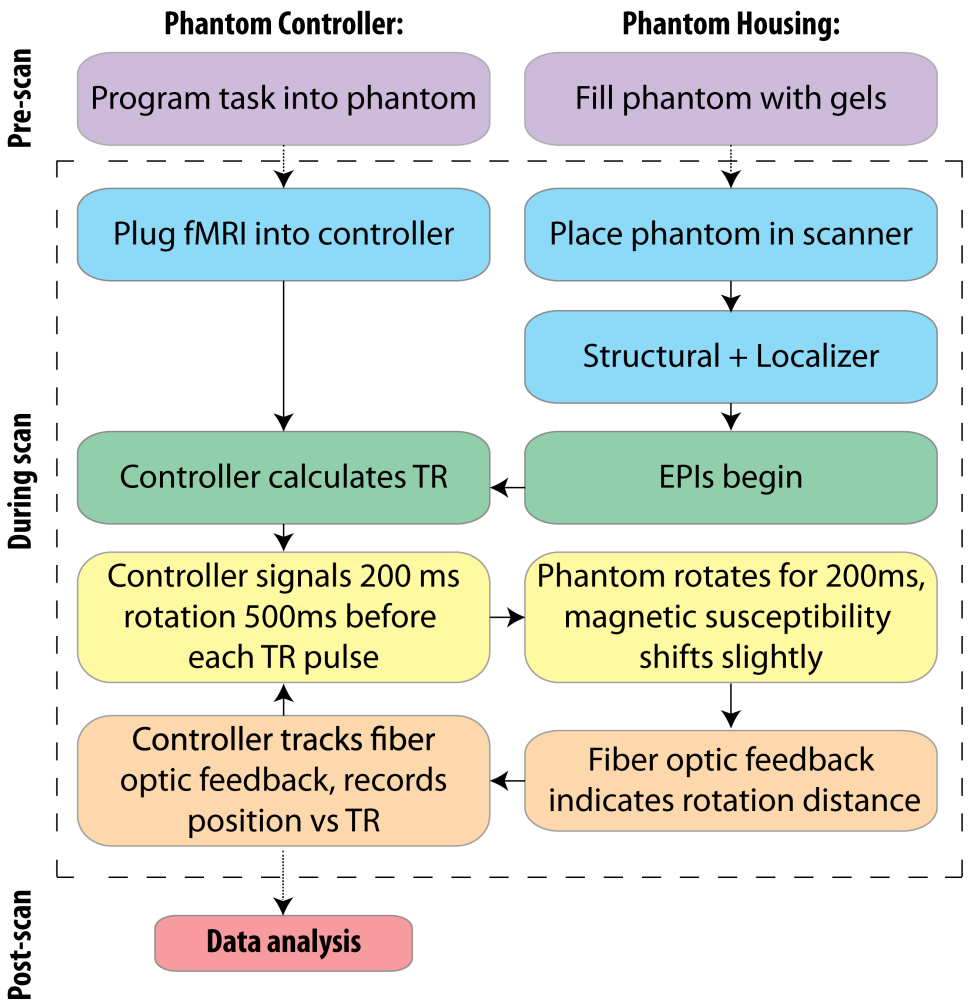

Figure 3.6: Flowchart for the phantom's operation.

Within-scanner (right) and control-room (left) based functions are separated for clarity.

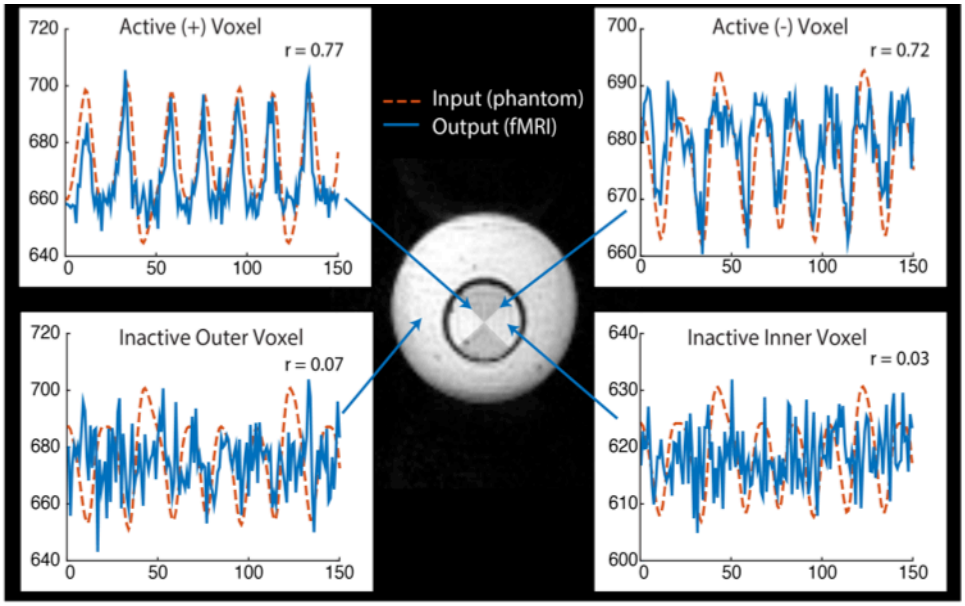

Figure 3.7: Dynamic phantom data acquisition.

The inner cylinder of the phantom rotates back and forth between TRs, producing signal changes at the gel-gel interfaces **(top panels, left and right)**. Voxels distant from the interfaces and within the static (non-rotating) outer cylinder experience uncorrelated scanner noise **(bottom panels, left and right)**.

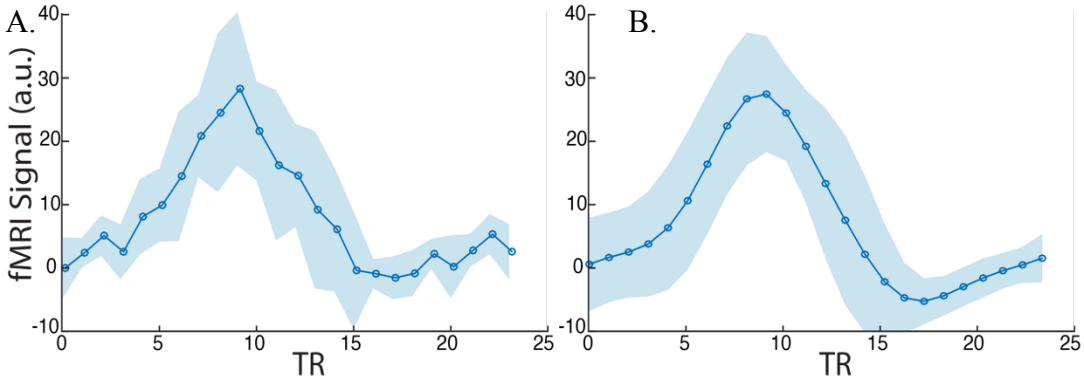

Figure 3.8: Validation of dynamic phantom biomimetic capabilities.

The dynamic phantom was programmed to physically simulate a biological hemodynamic response function within an fMRI task. Region of interest was a triangle straddling a single gel-gel interface, covering a total of 35 voxels. **(A)** Average window (raw data) following a programmed "stimulus." **(B)** For visualization purposes, the same window was band-pass filtered between 0.01 and 0.1 Hz.

CHAPTER 4

4. Signal Fluctuation Sensitivity Quantifies Temporal Fidelity for Resting-State Functional MRI

Preface

Portions of this chapter have been reproduced from the manuscript:

Daniel James DeDora, S. Nedic, P. Katti, S. Arnab, J. Polimeni, L.L. Wald, A. Takahashi, K. Van Dijk, R. Buckner, H.H. Strey, L.R. Mujica-Parodi, "Signal Fluctuation Sensitivity Quantifies Temporal Fidelity for Resting-State Functional MRI.", *In preparation.*

The authors listed in the above manuscript have contributions towards the data reported in this chapter.

4.1 Introduction

Neuroimaging with functional magnetic resonance imaging (fMRI) has proved to be an indispensible tool in addressing the explosion of interest in human brain connectivity and its relationship to brain-based disease. However, one significant consequence of fMRI's transition from mapping the areas of the brain most "active" under a task, towards the characterization of brain connections and circuits, is a radical and largely unacknowledged shift in what is considered *signal* versus *noise*.

During fMRI's first decade, researchers almost exclusively used stimulus presentation (*task*) to evoke *blood oxygen level dependent* (*BOLD*) activity in subjects. To identify the relationship between different brain regions and their functional roles, tasks included one or more experimental conditions, as well as a baseline measure absent of stimuli (*rest*). FMRI time-series were then fitted to an ideal expected hemodynamic shape for each condition (*canonical hemodynamic response function*, or *HRF*). Once fitted, trials for each condition were averaged and used to statistically compare hemodynamic amplitudes for each condition (*contrasts*) across subjects. Contrasts that met statistical thresholds were then represented as activity, producing activation maps.

The fitting, averaging, and subtraction approach used to analyze task-based data was primarily driven by the assumption that fMRI time-series had signal to noise ratios (SNR) too poor to preserve most of the dynamic information contained in the neuronal response. In the late 1990's, however, several influential papers (Biswal, Van Kylen et al. 1997, Raichle, MacLeod et al. 2001, Greicius, Krasnow et al. 2003, Salvador, Suckling et al. 2005) showed for the first time that the resting brain showed strong and reliable correlations between unfitted fMRI time-series; more recently, the relationship between correlation-derived networks, and the neuronal events that underlie them, has been identified using combined fMRI with electrophysiological recordings of local field potentials (Logothetis, Eschenko et al. 2012). The fMRI community quickly responded, and today *connectivity* studies—which map connections between brain nodes as defined by correlations between their time-series—comprise over 20% of human neuroimaging studies published every year(Bandettini 2014). Connectivity analyses include not only those that access the well-established *default mode network* (DMN), but also those obtained by correlations with a pre-defined region (*seed-based*) as well as those that describe graph-theoretic features of the connectome (*complex network analyses*) (Bassett and Bullmore 2006). Together, connectivity studies have contributed a wealth of new human brain data on aging (Damoiseaux, Beckmann et al. 2008), psychiatric (Greicius, Flores et al. 2007) and neurological (Bettus, Guedj et al. 2009) disorders, and injury (Mayer, Mannell et al. 2011). Resting-state fMRI protocols are easily standardized, require minimal patient compliance, and permit exploratory analyses; as such, they would appear to be well positioned for both clinical neurodiagnostics as well as large-scale international bio-repositories established for epidemiological research.

However, the transition from *activation maps* to *connections between nodes* not only produced a conceptual shift with respect to the role of functional neuroimaging, but also radically increased analytic dependence upon dynamic information contained within the time-series. The standard measure for establishing the quality of task-based data has been the *contrast-to-noise ratio (CNR)*, defined as the contrast (mean activation level acquired during task minus the mean activation level acquired during rest) divided by the standard deviation of the

time-series (Bandettini and Cox 2000). For task-free designs (such as resting-state), CNR cannot be computed, and thus is often replaced by the *temporal signal-to-noise ratio* (*tSNR*), defined as the mean of the time-series divided by its standard deviation (Kruger, Kastrup et al. 2001). Intuitively, both CNR and tSNR compare the amplitude of a signal against a background of undesired physiological, thermal, and scanner noise present in all fMRI studies. This manner of conceptualizing what is 'signal' versus what is 'noise' makes perfect sense within the context of activation maps, in which a task activates the brain reliably more under one condition (signal) than another (noise)(Murphy, Bodurka et al. 2007). However, for correlational analyses, *the gray matter fluctuations themselves are the signal*. Thus, for most connectivity studies, tSNR would appear to do exactly the opposite of what one would wish, as it penalizes sensitivity to the fluctuations (standard deviation of the time-series) upon which correlational analyses are based. Indeed, several recent studies have reported little correspondence between resting-state tSNR and the detection of stable functional networks (Smith, Beckmann et al. 2013, Welvaert and Rosseel 2013, Gonzalez-Castillo, Handwerker et al. 2014, Molloy, Meyerand et al. 2014).

For correlational analyses, rather than relegate time-series fluctuations to the category of noise (as per tSNR), we want to distinguish relevant fluctuations that are *neurobiologically significant* (e.g., emanating from BOLD signal consequent to neuronal response) from nuisance fluctuations that are *neurobiologically insignificant* (e.g., physiological, scanner, and motion artifact). The dissociation between the two can be characterized by *signal fluctuation sensitivity (SFS)*, which we define as:

Eqn. 1

$$SFS = \frac{< \mu_{voxel} >_{ROI}}{< \mu_{voxel} >_{global}} \times \frac{< \sigma_{voxel} >_{ROI}}{< \sigma_{voxel} >_{nuisance}}$$

In the first term, we average over mean (μ) voxel-specific values acquired for fMRI time-series in a *region of interest* (*ROI*) in the numerator, and for the entire brain (*global*) in the denominator. In the second term, we average over the standard deviation (σ) of fMRI time-series from each voxel obtained from a *region of interest* (*ROI*) in the numerator, and from a region in which BOLD signals are not expected, but in which physiological, scanner, and motion artifacts are still present, (*nuisance*) in the denominator. Prior work suggests that time-series obtained from cerebrospinal fluid (CSF) meet criteria for the *nuisance* denominator (Wald 2012).

In order to establish the validity of SFS in quantifying the degree to which fMRI accurately captures true BOLD fluctuations, we first need know the 'ground truth' for those fluctuations. To establish that ground truth, we designed a *dynamic phantom*, which provides user-controlled—and thus known—dynamic BOLD-like inputs to which fMRI-derived outputs can be compared. After validating SFS's relationship to the dynamic integrity of the BOLD-like signal, we then demonstrate SFS's ability to predict detection sensitivity to functional connectivity in human data, across three sets of representative acquisition parameters. Collectively, this work has powerful and direct practical applications to all functional MRI studies that utilize dynamic analyses.

4.2 Methods

4.2.1 Overview of the dynamic phantom for fMRI

Novel fMRI methods are typically validated with human imaging data. However, human data lack a "ground truth," in that researchers attempt to interpret an *output* (changes in fMRI signal) without direct knowledge of the *input* (i.e., neural-activity-triggered hemodynamics). Simulations could address this challenge by modeling input-output fidelity in the presence of physiological and scanner noise, but models can be susceptible to bias and often over-simplify the complexities of fMRI noise (Renvall and Hari 2009, Erhardt, Allen et al. 2012). Static phantoms are useful for quantifying scanner stability, but cannot be used to test dynamic fidelity. Therefore, we designed a novel dynamic phantom capable of producing tightly controlled changes in fMRI signal. In this way, we produced input-output mappings for three different scanners at three different sampling rates each, and tested whether SFS and tSNR predicted fidelity in the absence of confounding effects (such as physiological noise). The phantom design and validation data are detailed in **Figure 4.1**.

4.2.1.1 Design of the phantom

The dynamic phantom comprises two concentric cylinders coupled with a pneumatic motor and fiber optic feedback system. The outer cylinder contains a "baseline" agarose gel (2.27% w/w), while the inner cylinder is longitudinally divided with both (*i*) a baseline gel matching the outer cylinder and (*ii*) an "active" gel with slightly lower concentration of agarose (2.21% w/w). The longitudinally divided inner cylinder produces dynamic fMRI signal via rotation about its long axis via a novel fMRI-compatible pneumatic motor to drive rotation of the inner cylinder. The phantom receives image signals from the fMRI, and rotates only between image acquisitions to avoid motion artifacts. As the phantom rotates, position is monitored continuously through a fiber-optic feedback system. As the fMRI acquires each image, the phantom reads out its position, which serves as a 1:1 "input" for input-output mapping. During phantom validation, the phantom was programmed to produce fMRI signals according to a simple event-related protocol. See *Chapter 2* for fMRI scanning details regarding phantom validation. As expected, the dynamic phantom produced tightly controlled changes in fMRI signal (**Figure 4.1D**) in the presence of scanner noise. Thus, we utilized the phantom to develop and validate *SFS.*

First, we programmed the phantom to the mimic resting-state oscillations observed in human fMRI (van den Heuvel, Stam et al. 2008). We scanned the phantom in three different fMRI scanners, including a 3 Tesla magnet (3T) with a 32-channel headcoil (a fairly common setup), a 3T magnet with a 64-channel headcoil (a human connectome scanner), and a 7T magnet with a 32-channel headcoil (high-field scanner). The phantom was scanned at three different sampling rates (TR) within each scanner for ten minutes each; in total, we performed nine scans with the phantom. Scan parameters for each session can be found in **Table 4.1**.

The dynamic phantom is longitudinally divided into four chambers, and rotates about the long axis orthogonally to the main field (see **Figure 4.1D** for an example fMRI image). Due to the lack of confounding effects within the dynamic phantom, we exclusively used raw data in our analysis – i.e., no preprocessing was performed; however, the first 10 points of each dataset were removed to allow for steady state to be achieved. *Input-output fidelity was measured as the correlation between phantom position measurements and fMRI signal.* We computed SFS, tSNR, and fidelity for each time-series. For the *region of interest* (*ROI*) fluctuations, we extracted the average time-series from the four quadrants of the inner cylinder (corresponding to the four

chambers) with an automated masking procedure using MATLAB software developed in-house. We repeated this for six slices positioned in the center of the phantom (n = 24 time-series per scan). For the *nuisance* fluctuations, we extracted the time-series from the outer cylinder of the phantom, which does not activate. We then computed SFS based on the definition:

$$SFS_{Dynamic\ Phantom} = \frac{< \mu_{voxel} >_{inner\ cylinder}}{< \mu_{voxel} >_{global}} \times \frac{< \sigma_{voxel} >_{inner\ cylinder}}{< \sigma_{voxel} >_{outer\ cylinder}}$$

4.2.2 Human scanning and analyses

4.2.2.1 Acquisition

In an effort to represent a wide variety of task-free scanning paradigms, we collected three sets of human data (n = 12 subjects each) in the three scanners previously utilized for the phantom studies (3T 32 channel, 3T 64 channel, and 7T 32 channel) under three different sampling rates (2000ms, 1080ms, 802ms). As mentioned, these three scanners and sampling rates are a representation of a (*i*) standard acquisition paradigm (acquisition A), (*ii*) a Human Connectome Project (Harvard-MGH) paradigm (acquisition B), and a (*iii*) fast TR at high field paradigm (acquisition C), respectively. All subjects were age matched (μ_A = = 25.6 ± 3.7; μ_B = 23.3 ± 4.2; μ_C = 25.7 ± 3.6; p = 0.34, Kruskall-Wallis test). Acquisition A and acquisition C participants were exclusively male, while acquisition B had nine males and three females. Specific scanner parameters for these three studies are highlighted in Table 1. Anterior to posterior phase encoding was used in all scans. Scanner A acquisition lasted 5 minutes, while scanner B (originally 6.2 minutes) and scanner C (originally 10 minutes) data were truncated to match this duration. We removed the first ten seconds of data for all datasets. All participants were instructed to lie quietly with eyes open in the scanner without moving for the duration of the scan. A fixation cross was displayed for each scan.

4.2.2.2 Preprocessing

We followed the standard SPM 8 pipeline for realignment, coregistration to a structural image, and normalization to Montreal Neurological Institute (MNI) space. We examined both unsmoothed and smoothed data, because smoothing is considered standard procedure in most functional neuroimaging. We utilized a 4-mm (2 voxel) FWHM Gaussian smoothing kernel. Slice time correction was performed on acquisition A data, since the sampling rate was considerably slower than the other two scanners (TR = 2000ms vs. 1080ms and 802ms). Field map correction was performed on acquisition A and acquisition C. Scrubbing was performed to remove the influence of motion, with scan-to-scan global signal deviation from the mean > 3 and scan-to-scan composite motion > 0.5mm as thresholds for removal(Power, Barnes et al. 2012). The mean percentage of data points removed between all three groups was 2.22%, with no subjects having more than 9% of data scrubbed. Data were then imported into the Conn Toolbox for confound correction, which included time series detrending, regression of six motion variables (three translation vectors and three rotation vectors), regression of white matter and cerebrospinal fluid signals and temporal band-pass filtering between 0.01–0.1 Hz.

4.2.2.3 Computation of SFS, tSNR, amplitude of low frequency fluctuations, and regional homogeneity.

We used MATLAB to compute voxel-wise SFS and tSNR. SFS was computed as the mean signal of a voxel of interest (before confound regression, but after scrubbing) multiplied by the ratio between the standard deviation of the voxel of interest and the average standard deviation

of the cerebrospinal fluid (after confound regression). Cerebrospinal fluid mask was computed using an eroded apriori probabilistic map of CSF provided in SPM8 ($P > 0.6$) to ensure minimal contributions from neural sources. tSNR was computed voxel-wise as the mean (before confound regression, but after scrubbing) divided by the standard deviation of a signal (after confound regression).

Both amplitude of low frequency fluctuations (ALFF) and regional homogeneity (27-voxel KCC-ReHo) were computed from confound-corrected data, using the REST toolbox (Song, Dong et al. 2011). Resulting subject-specific voxel-wise ReHo and ALFF maps were standardized by dividing each voxel's value by the mean value of the whole brain. ALFF measures the total power of the low frequency components of a signal, which underlie resting-state connectivity analyses. ReHo is a measure of local connectivity. Thus, ALFF is a single-voxel measure, while ReHo is a measure of local synchronization of neighboring voxels.

To test whether tSNR or SFS were predictive of these established resting-state measures, we computed within-subject correlations between (*i*) SFS and ALFF, (*ii*) SFS and ReHo, (*iii*) tSNR and ALFF, and (*iv*) tSNR and ReHo for voxels belonging to the well-established *default mode network* (DMN) regions: medial prefrontal cortex (mPFC), posterior cingulate cortex (PCC), and left and right lateral parietal cortices (LLP and RLP). These regions were defined as 10-mm radius spheres centered on previously established coordinates, intersected with a SPM8 brain mask to ensure only brain voxels were included (Fox, Snyder et al. 2005). For the extraction of ROI-based SFS and tSNR values, we used the four aforementioned DMN masks, as well as a probabilistic gray matter mask from SPM8 ($P > 0.6$). We obtained subcortical ROI masks from the atlas included in CONN14p, which derived these from FSL Harvard-Oxford subcortical atlas.

4.3 Results

4.3.1 The Dynamic Phantom data suggest that SFS predicts input-output fidelity of fMRI time-series.

Temporal fidelity directly correlated with SFS for each of the nine scans (**Figure 4.2**; **Table 4.2**; mean $r = 0.56 \pm 0.12$; mean $p = 0.01$) and inversely correlated with tSNR for each of the nine scans (**Figure 4.2**; **Table 4.2**; mean $r = -0.58 \pm 0.17$; mean $p = 0.03$). Thus, when the scanner was most sensitive in capturing dynamic inputs, SFS was maximized while tSNR was minimized, and vice-versa. Given that researchers typically optimize acquisition parameters for fMRI connectivity studies by trying to maximize tSNR, the fact that doing so would appear to produce the least detection power has significant consequences for the neuroimaging community. Yet, the Dynamic Phantom is a well-defined system that differs from the brain significantly in the composition of its *ROI* and *nuisance* areas, as well as with respect to potential confounds from physiological noise. Therefore, the next step was to directly test the implications of our Dynamic Phantom SFS results for human connectivity studies.

4.3.2 SFS predicts resting state features in humans

We first tested whether SFS and tSNR would predict resting-state features on a single-subject level – a critical aspect of clinical neuroimaging (i.e., for diagnostics, pre-surgical localization, etc.). We performed region-specific correlations within the default mode network (DMN), revealing robust and significant positive relationships between SFS and ReHo (median $r = 0.62$, p's $<< 0.001$*; by acquisition set: $r_A = 0.61$, $r_B = 0.63$, $r_C = 0.60$; see **Figure 4.3** for median by

subject). In contrast, we found a negative correlation between tSNR and ReHo for all four DMN regions (median r = -0.36, p's << 0.01; by acquisition set: r_A = -0.49, r_B = -0.34, r_C = -0.26; see **Figure 4.3** for median by subject). Smoothing magnified this effect, where SFS positively predicted ReHo (median r = 0.78, all p's << 0.001; by acquisition set: r_A = 0.75, r_B = 0.81, r_C = 0.79) and tSNR negatively predicted ReHo (median r = -0.78, all p's << 0.001; by acquisition set: r_A = -0.77, r_B = -0.76, r_C = -0.80)

While ReHo is a measure of between-voxel connectivity, ALFF is a single-voxel measure that estimates the total power of the low frequency component of an fMRI signal, as these low frequency fluctuations are the basis of resting-state connectivity (Biswal, Yetkin et al. 1995). Thus, we expected the relationship between ALFF and SFS/tSNR (both single voxel measures) to be even more robust than the relationship between SFS and ReHo. Indeed, a strong positive relationship between ALFF and SFS was found (median r = 0.90, all p's << 0.001; by acquisition set: r_A = 0.93, r_B = 0.86, r_C = 0.85), whereas tSNR was negatively correlated with ALFF (median r = -0.80, all p's << 0.001; by acquisition set: r_A = -0.85, r_B = -0.79, r_C = -0.75). Again, smoothing magnified this effect for both SFS (median r = 0.96, all p's << 0.001; by acquisition set: r_A = 0.97, r_B = 0.95, r_C = 0.96), and tSNR (median r = -0.88, all p's << 0.001; by acquisition set: r_A = -0.88, r_B = -0.88, r_C = -0.88).

4.3.3 SFS and tSNR values between acquisition sets

The purpose of signal-to-noise ratio assessments, for any measurement, is to provide accurate feedback by which parameters can be tuned to optimize performance, as well as to aid in the interpretation and artifact-correction of results. Our three representative acquisition strategies illustrate clearly the practical importance of using SFS, and not tSNR, when optimizing fMRI studies for analyses that depend critically upon temporal fidelity. We compared SFS and tSNR values between acquisition paradigms for the *default mode network*, subcortical regions critical to the emotion and reward circuits, and global gray matter. To better represent realistic optimization studies, which normally utilize smoothing, we present results from 4-mm smoothed data. To directly compare SFS and tSNR values between acquisition sets, we extracted average values from seven ROIs, including the *default mode network*, *amygdala*, *caudate*, *hippocampus*, and average subcortical (each defined from FSL Harvard-Oxford Atlas ROIs included in CONN toolbox; *average subcortical* includes *bilateral accumbens*, *amygdala*, *caudate*, *hippocampus*, *pallidum*, *putamen*, and *thalamus*), as well as for all gray matter (using SPM8 probabilistic gray matter mask thresholded at P > 0.6). As shown in **Figure 4.4**, SFS identifies the advantages of increasingly temporal resolution, as well as the costs and benefits of increasing head-coil channels vs. field strength as a strategy to recovery signal loss from accelerated acquisition. In general, the ultra-dense head-coil strategy employed by *Acquisition B* optimizes over preserving temporal fidelity in cortical regions, whereas the ultra-high-field strategy employed by *Acquisition C* optimizes over preserving temporal fidelity in subcortical regions. TSNR provides a very different story: showing the greatest stability in *Acquisition A*, diminished performance in *Acquisition C*, and the worst performance in *Acquisition B*. Which strategy is optimal, for any particular study, therefore depends critically upon the scientific questions to be asked: not only with respect to the regions of interest implicated, but also the types of analyses to be performed.

4.4 DISCUSSION

Functional neuroimaging has ushered in a new era of brain research, in which time-series dynamics play an increasingly large role. As such, we need to reconsider whether fMRI

optimization paradigms that rely solely on maximizing stability might actually be leading us astray by minimizing detection of the very signal fluctuations upon which resting-state analyses are based. Here we propose a new measure—*Signal Fluctuation Sensitivity* (*SFS*)—that distinguishes between neurobiologically relevant fluctuations of interest, and nuisance fluctuations due to physiological or scanner artifact. We demonstrate that SFS positively—and tSNR negatively—correlates with temporal fidelity in a Dynamic Phantom, as well as with the detection power of local functional networks in humans, across three sets representative acquisition parameters previously optimized for clinical fMRI studies.

Our design of the Dynamic Phantom was motivated by the need to rigorously test temporal fidelity in response to known dynamic inputs, neither of which is possible using human data nor static phantoms. While we could have simulated input-output fidelity in the presence of physiological and scanner noise, models can be susceptible to bias and often over-simplify the complexities of fMRI noise (Renvall and Hari 2009, Erhardt, Allen et al. 2012). The empirical approach defined here captures actual scanner noise, and thus is more accurate in evaluating the utility of SFS to clinical neuroimaging.

While the phantom produced precise input-output mappings, the brain is not a well-defined system, and long-range brain connectivity is not yet reliable enough to provide a gold standard against which a new method can be compared. Thus, we used a more conservative measure of local-connectivity (*regional homogeneity – ReHo (Zang, Jiang et al. 2004)*), as well as a single voxel measure of resting-state signals (*amplitude of low frequency fluctuations – ALFF (Yu-Feng, Yong et al. 2007)*), for our evaluation of detection sensitivity for resting-state data. ReHo is correlated with task-activations and may be related to neurovascular coupling (Yuan, Di et al. 2013). Both ALFF and ReHo have been widely used to study resting-state brain activity, with clinical applications to Parkinson's Disease (Wu, Long et al. 2009), Alzheimer's Disease (Liu, Wang et al. 2008), and psychiatric illnesses (Han, Wang et al. 2011). Thus, we were able to show that, by optimizing for dynamic fidelity instead of temporal stability, SFS can have direct practical applications for clinical neuroimaging results.

In developing SFS for humans, one important decision is the optimal location for the acquisition of *nuisance* fluctuations. We chose *cerebrospinal fluid*, rather than surrounding air, white matter, or whole brain, because time-series from the cerebrospinal fluid contain the greatest proportion of nuisance variance of the three brain tissues (Wald 2012), including motion, scanner variance, and some physiological effects. Moreover, unlike white matter (Gawryluk, Mazerolle et al. 2014) and the global signal, the eroded CSF masks used here are unlikely to contain neurobiologically-relevant fluctuations of interest. Another consideration in the computation of SFS is that gray matter contains significantly more physiological noise contributions (heart-rate and respiration) than other tissues. Fluctuations within gray matter that are related to non-neural physiological noise may influence SFS computations. Therefore, it is important to employ proper preprocessing and physiological noise reduction schemes (such as confound correction in CONN) to reduce the influence of physiological noise.

Although we have emphasized the application of SFS to correlational analyses (connectivity, complex network) due to their increasing prevalence within the field, it is important to note that other types of dynamic analyses will also be much better served by optimization to SFS than tSNR. This category of approaches includes analyses based upon power spectra, complexity, and calculation of transfer functions (e.g., *ALFF*, *power spectrum scale invariance*, *entropic analyses*, *dynamic causal modeling*), for which temporal fidelity is

critical. However, this is not to suggest that CNR and tSNR do not continue to be useful and accurate measures in answering particular questions. TSNR is a measure of signal stability and is proportional to field strength, voxel size, and sampling rate (Kruger, Kastrup et al. 2001, Triantafyllou, Hoge et al. 2005); thus, in static phantoms, tSNR can be used to quantify and minimize scanner-related noise. If the primary aim of a study is to show contrast between two conditions, then CNR, and not SFS, is correct. For dynamic and nonlinear analytic methods (including task-free analyses), CNR is not directly measurable, thus classical tSNR is frequently cited as a surrogate (Van Dijk, Sabuncu et al. 2012, Smith, Beckmann et al. 2013). However, the relationship between tSNR during rest and task activation is inconsistent (Murphy, Bodurka et al. 2007), and gray matter regions with the lowest tSNR at rest also show the greatest activation during tasks (Yan, Zhuo et al. 2009). As with so many zero-sum decisions in fMRI acquisition, it is important to realize that we optimize over one parameter at the expense of the other. Therefore, just as tuning of acquisition parameters benefits enormously from knowing *a priori* the region of interest to be targeted, knowing *a priori* the type of analysis to be performed will permit researchers decide whether to optimize for stability (tSNR) or for dynamics (SFS).

4.5 Figures, Captions, and Tables.

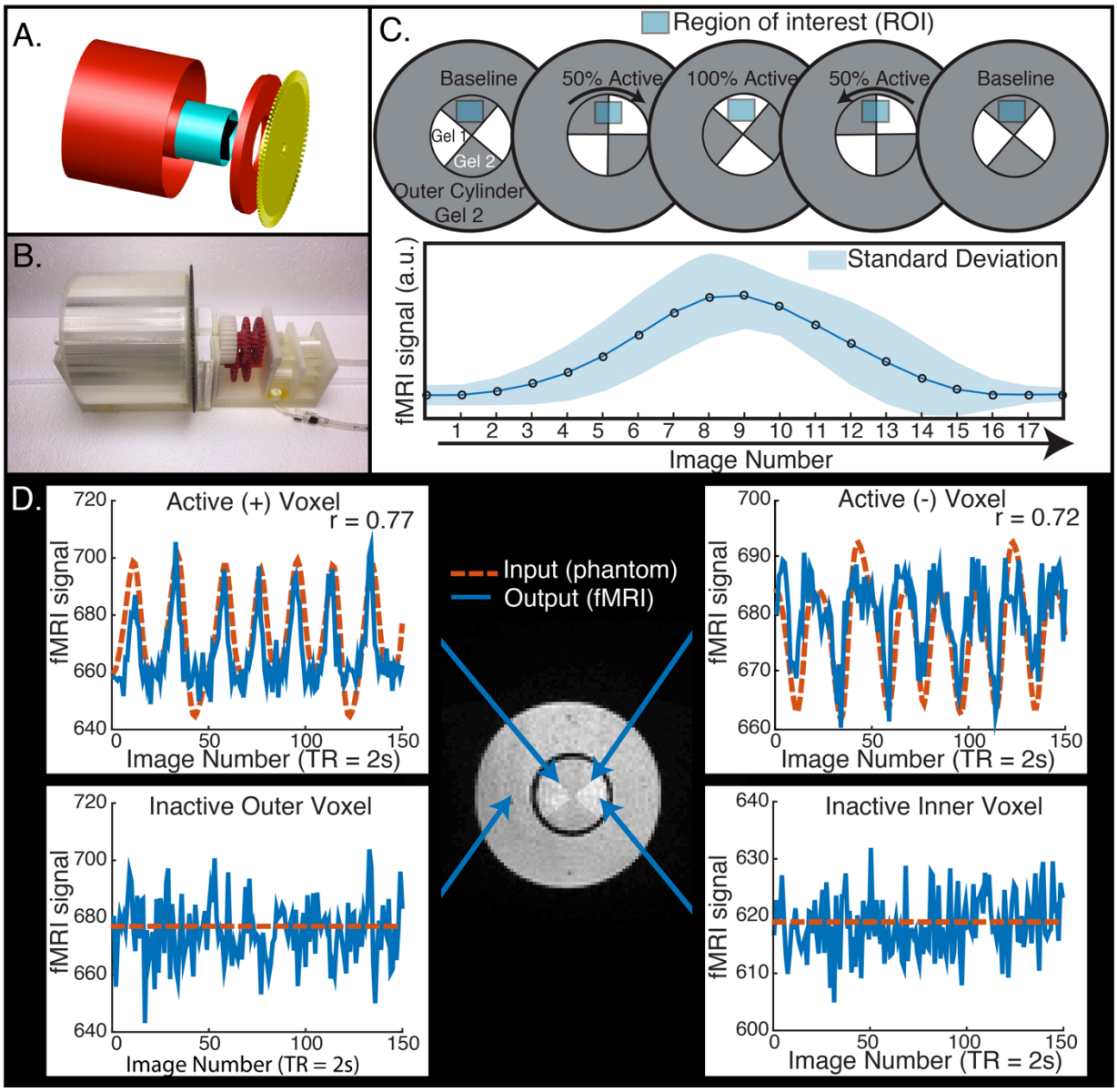

Figure 4.1: Design and validation of the dynamic phantom

The dynamic phantom produces tightly controlled changes in functional MRI signal, establishing a "ground truth" for quantifying input-output fidelity. **(A and B)** The dynamic phantom comprises concentric cylinders filled with agarose gels. The inner cylinder is coupled to an fMRI-compatible pneumatic motor and fiber optic feedback system. **(C)** The inner cylinder is longitudinally compartmentalized into four chambers. One of two calibrated agarose gels with different concentrations is contained in each; the gels are in direct contact. The outer cylinder contains a single agarose gel. Precisely-timed rotation of the inner cylinder between images produces dynamic changes in fMRI signal (bottom panel of C). **(D)** The top two panels demonstrate "active" voxels within the inner cylinder of the phantom along the gel-gel interfaces; these voxels exhibit strong input-output fidelity. The bottom two panels show that the

inactive outer cylinder and inactive inner cylinder voxels are indistinguishable. For validation of phantom performance, a simple event-related design is pictured in D. During the phantom scanning for SFS experiments, the phantom utilized a more complex input mimicking human resting-state data (**Figure 4.7**).

Figure 4.2: Fidelity vs. SFS and tSNR in the dynamic phantom

The dynamic phantom results suggest that resting-state signal to noise (SFS) better predicts fidelity than classical temporal signal to noise (tSNR). SFS predicts input-output fidelity (mean $r = 0.626$, $p < 0.01$), but tSNR inversely correlates with fidelity (mean $r = -0.671$, $p < 0.01$). These results suggest that SFS is more informative for dynamic signals than classical tSNR. Groups presented here match the scanning parameters presented in the subsequent human data – acquisition A represents data from a 3 Tesla magnet with a 32-channel headcoil (TR = 2000ms), acquisition B represents data from a 3 Tesla magnet with a 64-channel headcoil (TR = 1080ms), and acquisition C represents data from a 7 Tesla magnet with a 32-channel headcoil (TR = 802ms). Table 2 details the results from all nine dynamic phantom scans.

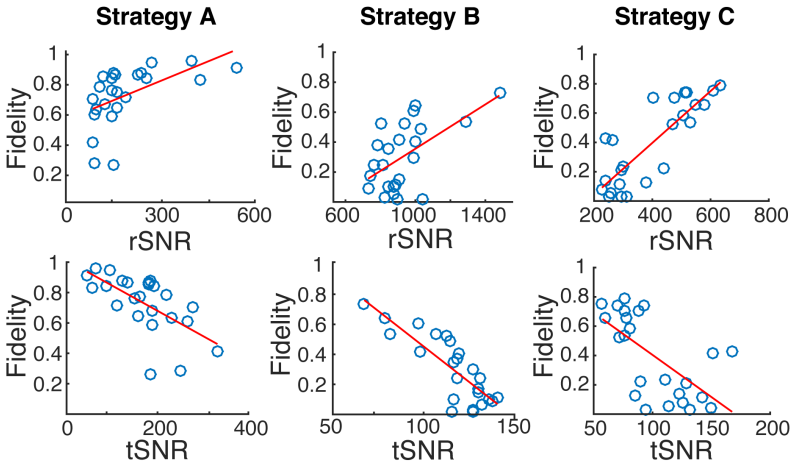

Figure 4.3: Signal fluctuation sensitivity (SFS) positively correlates with local neural synchrony across the default mode network, while classical tSNR negatively correlates with the same measure.

SFS strongly predicts regional homogeneity (a well-established measure of neural synchrony in fMRI) on an unsmoothed single-subject level across the *medial prefrontal cortex* (*mPFC*), *posterior cingulate cortex* (*PCC*), and *right and left lateral parietal lobes* (*RLP* and *LLP*), whereas tSNR inversely correlates with ReHo. Scatter plots are produced from a single representative subject, but *group r represents the average correlation between SFS/tSNR and ReHo between all 36 subjects in three scanners.* For each dataset, n = 12 participants took part in a five-minute rest scan. Images produced using BrainNet Viewer (https://www.nitrc.org/projects/bnv/).

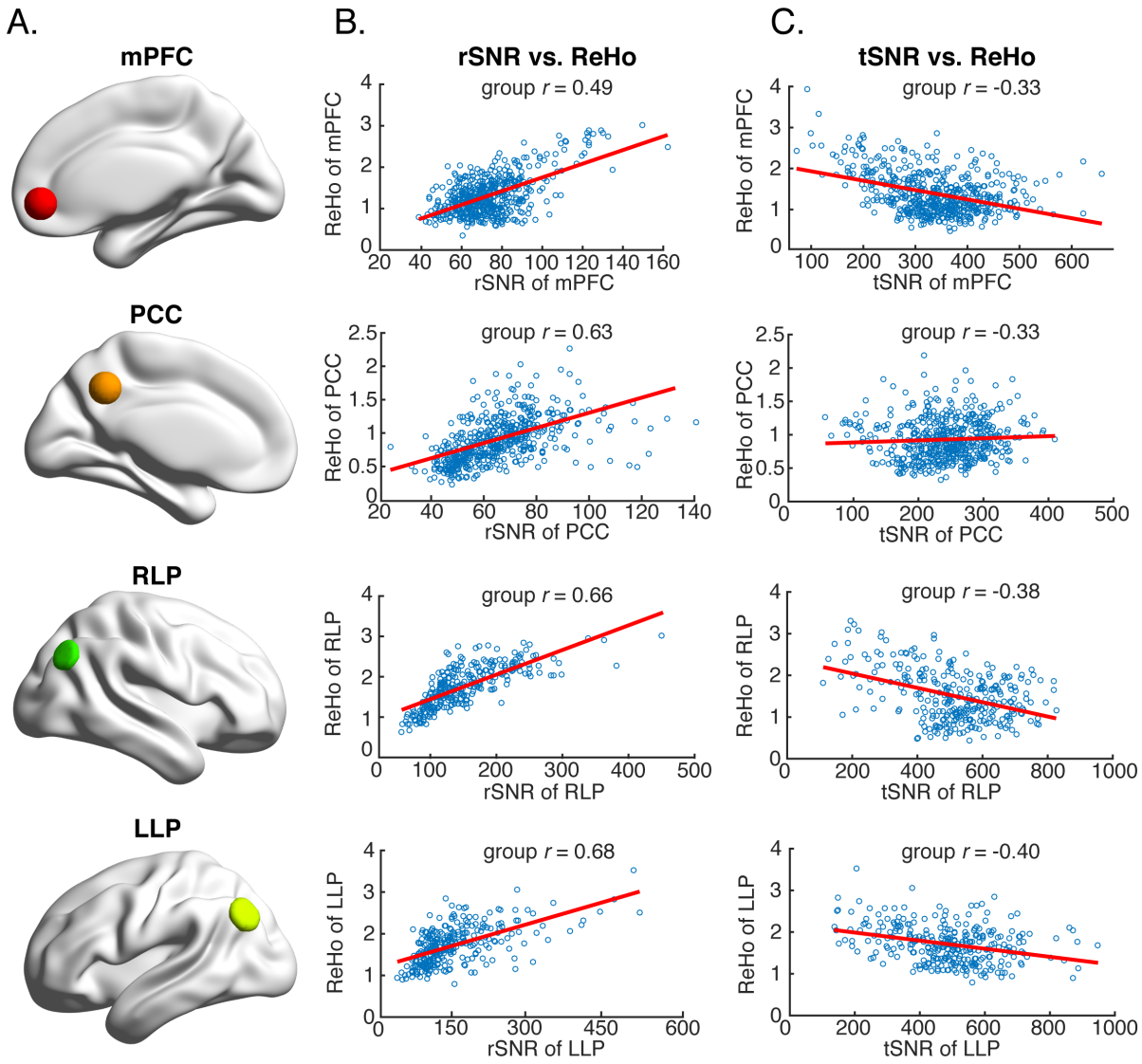

Figure 4.4: SFS distributions across the brain reveal differences in sensitivity between acquisition strategies.

As before, acquisition A represents data from a 3 Tesla magnet with a 32-channel headcoil (TR = 2000ms), acquisition B represents data from a 3 Tesla magnet with a 64-channel headcoil (TR = 1080ms), and acquisition C represents data from a 7 Tesla magnet with a 32-channel headcoil (TR = 802ms). (A) Full brain SFS maps for each acquisition demonstrate that cortical (especially prefrontal and parietal/visual) SFSs are robust across all acquisitions. Acquisition B shows more uniform cortical SFS than A or C, while acquisition C shows greater subcortical SFS than A or C. (B) SFS values across acquisition strategies averaged within several regions, including the DMN, subcortical regions, and gray matter. In general, acquisition A offered the lowest SFS. Overall gray matter SFS was highest in acquisition B, while subcortical SFS was highest in acquisition C. (C) Acquisition A demonstrated the highest tSNR for all regions, followed by acquisition C and acquisition B. These values were derived from preprocessed and smoothed resting-state data (n = 12 per group, 5 minutes of data). *p < 0.05, **p < 0.01, ***p < 0.001

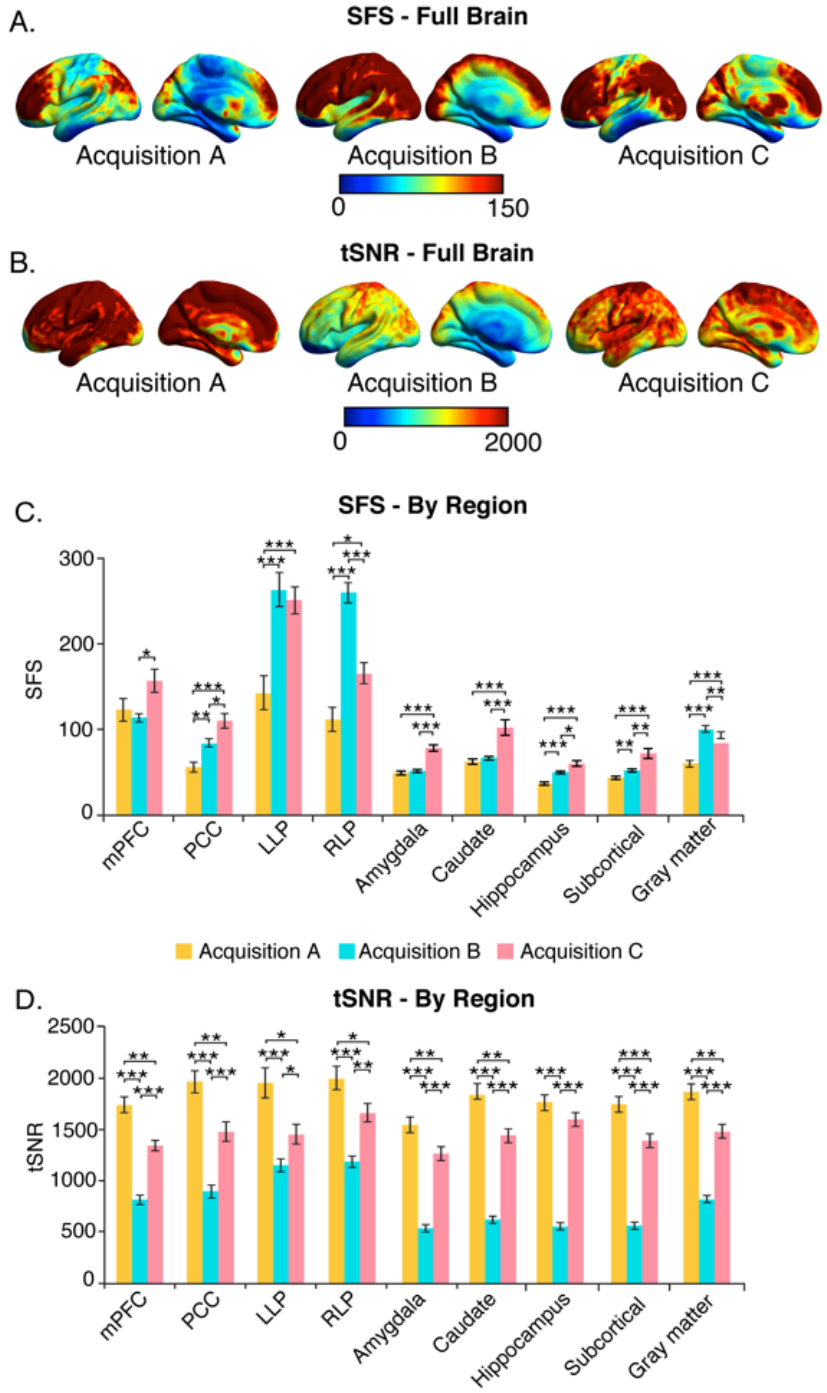

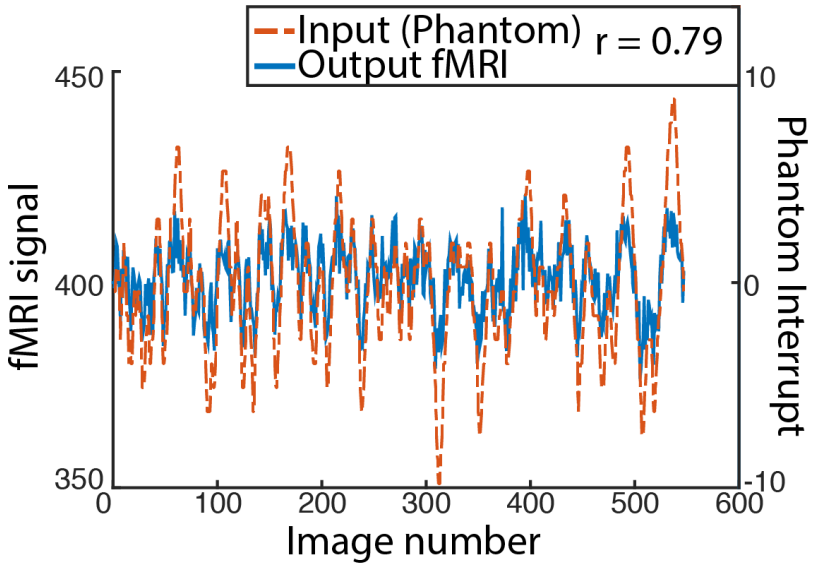

Figure 4.5: Pink noise waveform for phantom input.

To accurately mimic human resting-state fluctuations in the dynamic phantom, we utilized a complex waveform as shown above (dotted line). The 10-minute input function originated from our previous neuroimaging data and was subsequently programmed into the phantom. The Dynamic Phantom "inputs" (*Phantom Interrupt* axis) are derived from position tracking during rotation. A representative output fMRI signal is superimposed (*fMRI signal* axis), as acquired under *Acquisition B:* 3T magnet, 64 Channel head-coil, at TR = 1080 ms (see Table 1). This waveform was used for all nine phantom fMRI scans described here.

Scan Number	Main Field	Head Coil Channels	TR (ms)	TE	Resolution	Slices
1*	3	32	2000	30	2x2x2	69
2	3	32	1080	30	2x2x2	60
3	3	32	802	30	2x2x2	55
4	3	64	2000	30	2x2x2	62
5*	3	64	1080	30	2x2x2	68
6	3	64	824	30	2x2x2	65
7	7	32	2000	20	2x2x1.5	86
8	7	32	1010	20	2x2x1.5	84
9*	7	32	802	20	2x2x1.5	85

Table 4.1: ***Scan parameters for the nine dynamic phantom scans.***

We tested three scanners at three TRs with the dynamic phantom. *Highlighted rows indicate scans for which we collected corresponding human data, where scan 1 corresponds to acquisition A, scan 5 corresponds to acquisition B, and scan 9 corresponds to acquisition C.

	TR	3T 32Ch	3T 64Ch	7T 32Ch
	2000	0.525	0.539	0.439
SFS	**1080**	0.643	0.568	0.566
	802	0.442	0.512	0.837
	2000	–0.629	–0.611	–0.238*
tSNR	**1080**	–0.776	–0.823	–0.583
	802	–0.501	–0.450	–0.638

Table 4.2: SFS predicts fidelity.

SFS positively predicted input-output fidelity in all nine dynamic phantom scans, whereas tSNR inversely correlated with fidelity. All p's < 0.03. * *n.s.*

ACKNOWLEDGEMENTS

I want to thank my advisor, Dr. Lilianne Mujica-Parodi, and Dr. Helmut Strey for their guidance and help. I also want to thank my committee members – Dr. Terry Button and Dr. Larry Wald. I want to thank Dr. Ji Ook Cha for his collaboration, and Dr. Josh Carlson and Denis Rubin for their frequent assistance. I would like to thank my undergraduate team – Alex Calabro, Shafique Arnab, and Pratha Katti – for their help. We would like to thank Sheeba Arnold Anteraper, PhD, Kin Foon Wong, PhD, Jonathan Polimeni, PhD, Atsushi Takahashi, PhD, and Kimberly Burke for their assistance in scanning and troubleshooting. I would also like to thank Jaime Ide, PhD, for his helpful discussions.

I would like to thank the National Science Graduate Research Fellowship for their support. I would like to thank the Center for the integration of medicine and innovative technology (CIMIT) for supporting our Glucometer work (not present here). I would also like to thank the Center for Inclusive Education (CIE) for the Turner Fellowship, which supported my final year of studies.

REFERENCES:

Almeida, J. R., A. Versace, A. Mechelli, S. Hassel, K. Quevedo, D. J. Kupfer and M. L. Phillips (2009). "Abnormal amygdala-prefrontal effective connectivity to happy faces differentiates bipolar from major depression." Biol Psychiatry **66**(5): 451-459.

American Psychiatric Association. and American Psychiatric Association. Task Force on DSM-IV. (2000). Diagnostic and statistical manual of mental disorders : DSM-IV-TR. Washington, DC, American Psychiatric Association.

Anderson, J. S., B. A. Zielinski, J. A. Nielsen and M. A. Ferguson (2013). "Complexity of low-frequency blood oxygen level-dependent fluctuations covaries with local connectivity." Hum Brain Mapp.

Aron, A. R., P. C. Fletcher, E. T. Bullmore, B. J. Sahakian and T. W. Robbins (2003). "Stop-signal inhibition disrupted by damage to right inferior frontal gyrus in humans." Nat Neurosci **6**(2): 115-116.

Bach, D. R., B. Seymour and R. J. Dolan (2009). "Neural activity associated with the passive prediction of ambiguity and risk for aversive events." J Neurosci **29**(6): 1648-1656.

Bandettini, P. A. (2014). "Neuronal or hemodynamic? Grappling with the functional MRI signal." Brain Connect **4**(7): 487-498.

Bandettini, P. A. and R. W. Cox (2000). "Event-related fMRI contrast when using constant interstimulus interval: theory and experiment." Magn Reson Med **43**(4): 540-548.

Barbaro, B., R. Vitale, V. Valentini, S. Illuminati, F. M. Vecchio, G. Rizzo, M. A. Gambacorta, C. Coco, A. Crucitti, R. Persiani, L. Sofo and L. Bonomo (2011). "Diffusion-Weighted Magnetic Resonance Imaging in Monitoring Rectal Cancer Response to Neoadjuvant Chemoradiotherapy." Int J Radiat Oncol Biol Phys.

Barbas, H. and D. N. Pandya (1989). "Architecture and intrinsic connections of the prefrontal cortex in the rhesus monkey." J Comp Neurol **286**(3): 353-375.

Barry, R. L., L. M. Klassen, J. M. Williams and R. S. Menon (2008). "Hybrid two-dimensional navigator correction: a new technique to suppress respiratory-induced physiological noise in multi-shot echo-planar functional MRI." Neuroimage **39**(3): 1142-1150.

Bassett, D. S. and E. Bullmore (2006). "Small-world brain networks." Neuroscientist **12**(6): 512-523.

Beckmann, C. F. and S. M. Smith (2004). "Probabilistic independent component analysis for functional magnetic resonance imaging." IEEE Trans Med Imaging **23**(2): 137-152.

Behrens, T. E., H. J. Berg, S. Jbabdi, M. F. Rushworth and M. W. Woolrich (2007). "Probabilistic diffusion tractography with multiple fibre orientations: What can we gain?" Neuroimage **34**(1): 144-155.

Bettus, G., E. Guedj, F. Joyeux, S. Confort-Gouny, E. Soulier, V. Laguitton, P. J. Cozzone, P. Chauvel, J. P. Ranjeva, F. Bartolomei and M. Guye (2009). "Decreased basal fMRI functional connectivity in epileptogenic networks and contralateral compensatory mechanisms." Hum Brain Mapp **30**(5): 1580-1591.

Birn, R. M. (2012). "The role of physiological noise in resting-state functional connectivity." Neuroimage **62**(2): 864-870.

Birn, R. M., M. D. Cornejo, E. K. Molloy, R. Patriat, T. B. Meier, G. R. Kirk, V. A. Nair, M. E. Meyerand and V. Prabhakaran (2014). "The influence of physiological noise correction on test-retest reliability of resting-state functional connectivity." Brain Connect **4**(7): 511-522.

Bishop, S., J. Duncan, M. Brett and A. D. Lawrence (2004). "Prefrontal cortical function and anxiety: controlling attention to threat-related stimuli." Nat Neurosci **7**(2): 184-188.

Bishop, S. J. (2009). "Trait anxiety and impoverished prefrontal control of attention." Nat Neurosci **12**(1): 92-98.

Biswal, B., F. Z. Yetkin, V. M. Haughton and J. S. Hyde (1995). "Functional connectivity in the motor cortex of resting human brain using echo-planar MRI." Magn Reson Med **34**(4): 537-541.

Biswal, B. B., J. Van Kylen and J. S. Hyde (1997). "Simultaneous assessment of flow and BOLD signals in resting-state functional connectivity maps." NMR Biomed **10**(4-5): 165-170.

Blaimer, M., F. Breuer, M. Mueller, R. M. Heidemann, M. A. Griswold and P. M. Jakob (2004). "SMASH, SENSE, PILS, GRAPPA: how to choose the optimal method." Top Magn Reson Imaging **15**(4): 223-236.

Bozic, M., L. K. Tyler, D. T. Ives, B. Randall and W. D. Marslen-Wilson (2010). "Bihemispheric foundations for human speech comprehension." Proc Natl Acad Sci U S A **107**(40): 17439-17444.

Brash, P. D., J. Foster, W. Vennart, P. Anthony and J. E. Tooke (1999). "Magnetic resonance imaging techniques demonstrate soft tissue damage in the diabetic foot." Diabet Med **16**(1): 55-61.

Brown, G. G., J. E. Perthen, T. T. Liu and R. B. Buxton (2007). "A primer on functional magnetic resonance imaging." Neuropsychol Rev **17**(2): 107-125.

Bruning, R., K. Seelos, T. Yousry, J. Scheidler, H. Exner, U. Porn, M. Reiser and B. R. Rosen (1999). "Echo-planar magnetic resonance imaging (EPI) with high-resolution matrix in intra-axial brain tumors." Eur Radiol **9**(7): 1392-1396.

Bullmore, E. T., M. J. Brammer, S. Rabe-Hesketh, V. A. Curtis, R. G. Morris, S. C. Williams, T. Sharma and P. K. McGuire (1999). "Methods for diagnosis and treatment of stimulus-correlated motion in generic brain activation studies using fMRI." Hum Brain Mapp **7**(1): 38-48.

Bullmore, E. T., S. Rabe-Hesketh, R. G. Morris, S. C. Williams, L. Gregory, J. A. Gray and M. J. Brammer (1996). "Functional magnetic resonance image analysis of a large-scale neurocognitive network." Neuroimage **4**(1): 16-33.

Buxton, R. B., E. C. Wong and L. R. Frank (1998). "Dynamics of blood flow and oxygenation changes during brain activation: the balloon model." Magn Reson Med **39**(6): 855-864.

Carlson, J. M., T. Greenberg and L. R. Mujica-Parodi (2010). "Blind rage? Heightened anger is associated with altered amygdala responses to masked and unmasked fearful faces." Psychiatry Res **182**(3): 281-283.

Cha, J., J. M. Carlson, D. J. Dedora, T. Greenberg, G. H. Proudfit and L. R. Mujica-Parodi (2014). "Hyper-reactive human ventral tegmental area and aberrant mesocorticolimbic

connectivity in overgeneralization of fear in generalized anxiety disorder." J Neurosci **34**(17): 5855-5860.

Cha, J., T. Greenberg, J. M. Carlson, D. J. Dedora, G. Hajcak and L. R. Mujica-Parodi (2014). "Circuit-wide structural and functional measures predict ventromedial prefrontal cortex fear generalization: implications for generalized anxiety disorder." J Neurosci **34**(11): 4043-4053.

Cheng, H., Q. Zhao, G. R. Duensing, W. A. Edelstein, D. Spencer, N. Browne, C. Saylor and M. Limkeman (2006). "SmartPhantom--an fMRI simulator." Magn Reson Imaging **24**(3): 301-313.

Cheng, H., Q. Zhao, D. Spencer, G. R. Duensing and W. A. Edelstein (2004). A fMRI Study of the SMARTPHANTOM. Proceedings of the International Society of Magnetic Resonance in Medicine.

Christoffersson, J. O., L. E. Olsson and S. Sjoberg (1991). "Nickel-doped agarose gel phantoms in MR imaging." Acta Radiol **32**(5): 426-431.

Churchill, N. W. and S. C. Strother (2013). "PHYCAA+: an optimized, adaptive procedure for measuring and controlling physiological noise in BOLD fMRI." Neuroimage **82**: 306-325.

Churchill, N. W., G. Yourganov, R. Spring, P. M. Rasmussen, W. Lee, J. E. Ween and S. C. Strother (2012). "PHYCAA: data-driven measurement and removal of physiological noise in BOLD fMRI." Neuroimage **59**(2): 1299-1314.

Clauset, A., C. R. Shalizi and M. E. J. Newman (2009). "Power-Law Distributions in Empirical Data." Siam Review **51**(4): 661-703.

Damoiseaux, J. S., C. F. Beckmann, E. J. Arigita, F. Barkhof, P. Scheltens, C. J. Stam, S. M. Smith and S. A. Rombouts (2008). "Reduced resting-state brain activity in the "default network" in normal aging." Cereb Cortex **18**(8): 1856-1864.

Daunizeau, J., K. J. Friston and S. J. Kiebel (2009). "Variational Bayesian identification and prediction of stochastic nonlinear dynamic causal models." Physica D **238**(21): 2089-2118.

DeLaPaz, R. L. (1994). "Echo-Planar Imaging." Radiographics.

Depue, B. E., T. Curran and M. T. Banich (2007). "Prefrontal regions orchestrate suppression of emotional memories via a two-phase process." Science **317**(5835): 215-219.

Dreiss, C. A., T. Cosgrove, N. J. Benton, D. Kilburn, M. A. Alam, R. G. Schmidt and G. V. Gordon (2007). "Effect of crosslinking on the mobility of PDMS filled with polysilicate nanoparticles: Positron lifetime, rheology and NMR relaxation studies." Polymer **48**(15): 4419-4428.

Drobnjak, I., D. Gavaghan, E. Suli, J. Pitt-Francis and M. Jenkinson (2006). "Development of a functional magnetic resonance imaging simulator for modeling realistic rigid-body motion artifacts." Magn Reson Med **56**(2): 364-380.

Ebrahimi, B., S. D. Swanson and T. E. Chupp (2010). "A Microfabricated Phantom for Quantitative MR Perfusion Measurements: Validation of Singular Value Decomposition Deconvolution Method." IEEE Trans Biomed Eng **57**(11).

Eippert, F., R. Veit, N. Weiskopf, M. Erb, N. Birbaumer and S. Anders (2007). "Regulation of emotional responses elicited by threat-related stimuli." Hum Brain Mapp **28**(5): 409-423.

Erhardt, E. B., E. A. Allen, Y. Wei, T. Eichele and V. D. Calhoun (2012). "SimTB, a simulation toolbox for fMRI data under a model of spatiotemporal separability." Neuroimage **59**(4): 4160-4167.

First, M. B., R. L. Spitzer, M. Gibbon and J. B. W. Williams (2002). "Structured clinical interview for DSM-IV-TR axis I disorders, research version, patient edition." New York: Biometrics Research, New York State Psychiatric Institute.

Fischer, G. S., I. Iordachita, C. Csoma, J. Tokuda, S. P. Dimaio, C. M. Tempany, N. Hata and G. Fichtinger (2008). "MRI-Compatible Pneumatic Robot for Transperineal Prostate Needle Placement." IEEE ASME Trans Mechatron **13**(3): 295-305.

Fitzgerald, D. A., M. Angstadt, L. M. Jelsone, P. J. Nathan and K. L. Phan (2006). "Beyond threat: amygdala reactivity across multiple expressions of facial affect." Neuroimage **30**(4): 1441-1448.

Fox, M. D., A. Z. Snyder, J. L. Vincent, M. Corbetta, D. C. Van Essen and M. E. Raichle (2005). "The human brain is intrinsically organized into dynamic, anticorrelated functional networks." Proc Natl Acad Sci U S A **102**(27): 9673-9678.

Freire, L. and J. F. Mangin (2001). "Motion correction algorithms may create spurious brain activations in the absence of subject motion." Neuroimage **14**(3): 709-722.

Friedman, L. and G. H. Glover (2006). "Report on a multicenter fMRI quality assurance protocol." J Magn Reson Imaging **23**(6): 827-839.

Friedman, L., G. H. Glover, D. Krenz and V. Magnotta (2006). "Reducing inter-scanner variability of activation in a multicenter fMRI study: role of smoothness equalization." Neuroimage **32**(4): 1656-1668.

Friedman, L., H. Stern, G. G. Brown, D. H. Mathalon, J. Turner, G. H. Glover, R. L. Gollub, J. Lauriello, K. O. Lim, T. Cannon, D. N. Greve, H. J. Bockholt, A. Belger, B. Mueller, M. J. Doty, J. He, W. Wells, P. Smyth, S. Pieper, S. Kim, M. Kubicki, M. Vangel and S. G. Potkin (2008). "Test-retest and between-site reliability in a multicenter fMRI study." Hum Brain Mapp **29**(8): 958-972.

Friedman, L., Q. Zhao, H. Cheng, R. Duensing, G. D. N. and G. H. Glover (2004). Multi-center fMRI Calibration with SMARTPHANTOM. 12th Annual Meeting of the International Society for Magnetic Resonance Imaging (ISMRM), Kyoto, Japan.

Friston, K. (2009). "Causal modelling and brain connectivity in functional magnetic resonance imaging." PLoS Biol **7**(2): e33.

Friston, K., J. Ashburner, C. D. Frith, J. B. Poline, J. D. Heather and R. S. Frackowiak (1995). "Spatial registration and normalization of images." Hum Brain Mapp **3**(3).

Friston, K. J., C. Buechel, G. R. Fink, J. Morris, E. Rolls and R. J. Dolan (1997). "Psychophysiological and modulatory interactions in neuroimaging." Neuroimage **6**(3): 218-229.

Friston, K. J., L. Harrison and W. Penny (2003). "Dynamic causal modelling." Neuroimage **19**(4): 1273-1302.

Friston, K. J., S. Williams, R. Howard, R. S. Frackowiak and R. Turner (1996). "Movement-related effects in fMRI time-series." Magn Reson Med **35**(3): 346-355.

Fruehauf, H., D. Menne, M. A. Kwiatek, Z. Forras-Kaufman, E. Kaufman, O. Goetze, M. Fried, W. Schwizer and M. Fox (2011). "Inter-observer reproducibility and analysis of gastric volume measurements and gastric emptying assessed with magnetic resonance imaging." Neurogastroenterol Motil **23**(9): 854-861.

Gawryluk, J. R., E. L. Mazerolle and R. C. D'Arcy (2014). "Does functional MRI detect activation in white matter? A review of emerging evidence, issues, and future directions." Front Neurosci **8**: 239.

Glover, G. H., T. Q. Li and D. Ress (2000). "Image-based method for retrospective correction of physiological motion effects in fMRI: RETROICOR." Magn Reson Med **44**(1): 162-167.

Gonzalez-Castillo, J., D. A. Handwerker, M. E. Robinson, C. W. Hoy, L. C. Buchanan, Z. S. Saad and P. A. Bandettini (2014). "The spatial structure of resting state connectivity stability on the scale of minutes." Front Neurosci **8**: 138.

Greenberg, T., J. M. Carlson, J. Cha, G. Hajcak and L. R. Mujica-Parodi (2011). "Neural reactivity tracks fear generalization gradients." Biol Psychol.

Greenberg, T., J. M. Carlson, J. Cha, G. Hajcak and L. R. Mujica-Parodi (2013). "Neural reactivity tracks fear generalization gradients." Biol Psychol **92**(1): 2-8.

Greenberg, T., J. M. Carlson, J. Cha, G. Hajcak and L. R. Mujica-Parodi (2013). "Ventromedial prefrontal cortex reactivity is altered in generalized anxiety disorder during fear generalization." Depress Anxiety **30**(3): 242-250.

Greicius, M. D., B. H. Flores, V. Menon, G. H. Glover, H. B. Solvason, H. Kenna, A. L. Reiss and A. F. Schatzberg (2007). "Resting-state functional connectivity in major depression: abnormally increased contributions from subgenual cingulate cortex and thalamus." Biol Psychiatry **62**(5): 429-437.

Greicius, M. D., B. Krasnow, A. L. Reiss and V. Menon (2003). "Functional connectivity in the resting brain: a network analysis of the default mode hypothesis." Proc Natl Acad Sci U S A **100**(1): 253-258.

Greve, D. N., G. G. Brown, B. A. Mueller, G. Glover, T. T. Liu and N. Function Biomedical Research (2013). "A survey of the sources of noise in fMRI." Psychometrika **78**(3): 396-416.

Greve, D. N., B. A. Mueller, T. Liu, J. A. Turner, J. Voyvodic, E. Yetter, M. Diaz, G. McCarthy, S. Wallace, B. J. Roach, J. M. Ford, D. H. Mathalon, V. D. Calhoun, C. G. Wible, G. G. Brown, S. G. Potkin and G. Glover (2011). "A novel method for quantifying scanner instability in fMRI." Magn Reson Med **65**(4): 1053-1061.

Griswold, M. A., P. M. Jakob, R. M. Heidemann, M. Nittka, V. Jellus, J. Wang, B. Kiefer and A. Haase (2002). "Generalized autocalibrating partially parallel acquisitions (GRAPPA)." Magn Reson Med **47**(6): 1202-1210.

Haans, J. J., I. M. de Zwart, P. H. Eilers, J. H. Reiber, J. Doornbos, A. de Roos and A. A. Masclee (2011). "Gastric volume changes in response to a meal: Validation of magnetic resonance imaging versus the barostat." J Magn Reson Imaging.

Han, Y., J. Wang, Z. Zhao, B. Min, J. Lu, K. Li, Y. He and J. Jia (2011). "Frequency-dependent changes in the amplitude of low-frequency fluctuations in amnestic mild cognitive impairment: a resting-state fMRI study." Neuroimage **55**(1): 287-295.

Hansen, L. K., J. Larsen, F. A. Nielsen, S. C. Strother, E. Rostrup, R. Savoy, N. Lange, J. Sidtis, C. Svarer and O. B. Paulson (1999). "Generalizable patterns in neuroimaging: how many principal components?" Neuroimage **9**(5): 534-544.

He, B. J. (2011). "Scale-free properties of the functional magnetic resonance imaging signal during rest and task." J Neurosci **31**(39): 13786-13795.

He, B. J., J. M. Zempel, A. Z. Snyder and M. E. Raichle (2010). "The temporal structures and functional significance of scale-free brain activity." Neuron **66**(3): 353-369.

Hennigan, K., K. D'Ardenne and S. M. McClure (2015). "Distinct midbrain and habenula pathways are involved in processing aversive events in humans." J Neurosci **35**(1): 198-208.

Hettema, J. M., B. Kettenmann, V. Ahluwalia, C. McCarthy, W. R. Kates, J. E. Schmitt, J. L. Silberg, M. C. Neale, K. S. Kendler and P. Fatouros (2012). "Pilot multimodal twin imaging study of generalized anxiety disorder." Depress Anxiety **29**(3): 202-209.

Huettel, S., A. W. Song and G. McCarthy (2004). Functional Magentic Resonance Imaging. Sunderland, Sinauer Associates.

Hutton, C., O. Josephs, J. Stadler, E. Featherstone, A. Reid, O. Speck, J. Bernarding and N. Weiskopf (2011). "The impact of physiological noise correction on fMRI at 7 T." Neuroimage **57**(1): 101-112.

Jabbour, A., T. F. Ismail, N. Moat, A. Gulati, I. Roussin, F. Alpendurada, B. Park, F. Okoroafor, A. Asgar, S. Barker, S. Davies, S. K. Prasad, M. Rubens and R. H. Mohiaddin (2011). "Multimodality imaging in transcatheter aortic valve implantation and post-procedural aortic regurgitation: comparison among cardiovascular magnetic resonance, cardiac computed tomography, and echocardiography." J Am Coll Cardiol **58**(21): 2165-2173.

Jaffar, M. A., Q. Ain and T. S. Choi (2011). "Tumor detection from enhanced magnetic resonance imaging using fuzzy curvelet." Microsc Res Tech.

Jo, H. J., S. J. Gotts, R. C. Reynolds, P. A. Bandettini, A. Martin, R. W. Cox and Z. S. Saad (2013). "Effective Preprocessing Procedures Virtually Eliminate Distance-Dependent Motion Artifacts in Resting State FMRI." J Appl Math **2013**.

Josephs, O. and R. N. Henson (1999). "Event-related functional magnetic resonance imaging: modelling, inference and optimization." Philos Trans R Soc Lond B Biol Sci **354**(1387): 1215-1228.

Kim, M. J. and P. J. Whalen (2009). "The structural integrity of an amygdala-prefrontal pathway predicts trait anxiety." J Neurosci **29**(37): 11614-11618.

Kruger, G., A. Kastrup and G. H. Glover (2001). "Neuroimaging at 1.5 T and 3.0 T: comparison of oxygenation-sensitive magnetic resonance imaging." Magn Reson Med **45**(4): 595-604.

Kruggel, F., D. Y. von Cramon and X. Descombes (1999). "Comparison of filtering methods for fMRI datasets." Neuroimage **10**(5): 530-543.

L, W., F. H. D, B. H. I and L. J (2012). "A systematic review of resting-state functional-MRI studies in major depression." J Affect Disord **142**(1-3): 6-12.

Lauterbur, P. (1973). "Image formation by induced local interactions: examples employing nuclear magnetic resonance." Nature.

LeDoux, J. (2003). "The emotional brain, fear, and the amygdala." Cell Mol Neurobiol **23**(4-5): 727-738.

Li, B., K. J. Friston, J. Liu, Y. Liu, G. Zhang, F. Cao, L. Su, S. Yao, H. Lu and D. Hu (2014). "Impaired frontal-basal ganglia connectivity in adolescents with internet addiction." Sci Rep **4**: 5027.

Li, S. P., A. R. Padhani and A. Makris (2011). "Dynamic contrast-enhanced magnetic resonance imaging and blood oxygenation level-dependent magnetic resonance imaging for the assessment of changes in tumor biology with treatment." J Natl Cancer Inst Monogr **2011**(43): 103-107.

Li, Y., S. Reza and M. K. Limkeman (2007). "Phantom calibration method for improved temporal characterization of hemodynamic response in event-related fMRI." Neuroimage **35**(2): 566-576.

Lissek, S., A. L. Biggs, S. J. Rabin, B. R. Cornwell, R. P. Alvarez, D. S. Pine and C. Grillon (2008). "Generalization of conditioned fear-potentiated startle in humans: experimental validation and clinical relevance." Behav Res Ther **46**(5): 678-687.

Lissek, S., S. Rabin, R. E. Heller, D. Lukenbaugh, M. Geraci, D. S. Pine and C. Grillon (2010). "Overgeneralization of conditioned fear as a pathogenic marker of panic disorder." Am J Psychiatry **167**(1): 47-55.

Lissek, S., S. J. Rabin, D. J. McDowell, S. Dvir, D. E. Bradford, M. Geraci, D. S. Pine and C. Grillon (2009). "Impaired discriminative fear-conditioning resulting from elevated fear responding to learned safety cues among individuals with panic disorder." Behav Res Ther **47**(2): 111-118.

Liu, Y., K. Wang, C. Yu, Y. He, Y. Zhou, M. Liang, L. Wang and T. Jiang (2008). "Regional homogeneity, functional connectivity and imaging markers of Alzheimer's disease: a review of resting-state fMRI studies." Neuropsychologia **46**(6): 1648-1656.

Logothetis, N. K., O. Eschenko, Y. Murayama, M. Augath, T. Steudel, H. C. Evrard, M. Besserve and A. Oeltermann (2012). "Hippocampal-cortical interaction during periods of subcortical silence." Nature **491**(7425): 547-553.

Luk, G., D. W. Green, J. Abutalebi and C. Grady (2011). "Cognitive control for language switching in bilinguals: A quantitative meta-analysis of functional neuroimaging studies." Lang Cogn Process **27**(10): 1479-1488.

Lutti, A., D. L. Thomas, C. Hutton and N. Weiskopf (2013). "High-resolution functional MRI at 3 T: 3D/2D echo-planar imaging with optimized physiological noise correction." Magn Reson Med **69**(6): 1657-1664.

Ma, L., J. L. Steinberg, K. A. Cunningham, S. D. Lane, L. A. Kramer, P. A. Narayana, T. R. Kosten, A. Bechara and F. G. Moeller (2014). "Inhibitory Behavioral Control: A Stochastic Dynamic Causal Modeling Study Using Network Discovery Analysis." Brain Connect.

Matsumura, S., I. Aoki, T. Saga and K. Shiba (2011). "A tumor-environment-responsive nanocarrier that evolves its surface properties upon sensing matrix metalloproteinase-2 and initiates agglomeration to enhance T2 relaxivity for magnetic resonance imaging." Mol Pharm **8**(5): 1970-1974.

Mayer, A. R., M. V. Mannell, J. Ling, C. Gasparovic and R. A. Yeo (2011). "Functional connectivity in mild traumatic brain injury." Hum Brain Mapp **32**(11): 1825-1835.

McKeown, M. J., T. P. Jung, S. Makeig, G. Brown, S. S. Kindermann, T. W. Lee and T. J. Sejnowski (1998). "Spatially independent activity patterns in functional MRI data during the stroop color-naming task." Proc Natl Acad Sci U S A **95**(3): 803-810.

McKeown, M. J., S. Makeig, G. G. Brown, T. P. Jung, S. S. Kindermann, A. J. Bell and T. J. Sejnowski (1998). "Analysis of fMRI data by blind separation into independent spatial components." Hum Brain Mapp **6**(3): 160-188.

McKeown, M. J. and T. J. Sejnowski (1998). "Independent component analysis of fMRI data: examining the assumptions." Hum Brain Mapp **6**(5-6): 368-372.

McLean, C. P., A. Asnaani, B. T. Litz and S. G. Hofmann (2011). "Gender differences in anxiety disorders: prevalence, course of illness, comorbidity and burden of illness." J Psychiatr Res **45**(8): 1027-1035.

McLellan, A. J., S. C. McKenzie and A. J. Taylor (2011). "Cardiac Magnetic Resonance Imaging Predicts Recovery of Left Ventricular Function in Acute Onset Cardiomyopathy." Heart Lung Circ.

McRobbie, D. W., E. A. Moore, M. J. Graves and M. R. Prince, Eds. (2007). MRI from Picture to Proton.

McRobbie, D. W., E. A. Moore, M. J. Graves and M. R. Prince (2011). MRI: From Picture to Proton, Cambridge University Press.

Metzner, A., D. Kivelitz, B. Schmidt, A. Fuernkranz, E. Wissner, R. R. Tilz, M. Konstantinidou, A. Rillig, Y. Yoshiga, S. Mathew, F. Ouyang and K. H. Kuck (2011). "Impact of pulmonary vein anatomy assessed by cardiac magnetic resonance imaging on endoscopic pulmonary vein isolation in consecutive patients." Europace.

Miezin, F. M., L. Maccotta, J. M. Ollinger, S. E. Petersen and R. L. Buckner (2000). "Characterizing the hemodynamic response: effects of presentation rate, sampling procedure, and the possibility of ordering brain activity based on relative timing." Neuroimage **11**(6 Pt 1): 735-759.

Mikkelsen, K. B. and T. E. Lund (2013). "Sampling rate dependence of correlation at long time lags in BOLD fMRI measurements on humans and gel phantoms." Front Physiol **4**: 106.

Molloy, E. K., M. E. Meyerand and R. M. Birn (2014). "The influence of spatial resolution and smoothing on the detectability of resting-state and task fMRI." Neuroimage **86**: 221-230.

Motzkin, J. C., C. L. Philippi, R. C. Wolf, M. K. Baskaya and M. Koenigs (2015). "Ventromedial prefrontal cortex is critical for the regulation of amygdala activity in humans." Biol Psychiatry **77**(3): 276-284.

Mujica-Parodi, L. R., J. M. Carlson, J. Cha and D. Rubin (2014). "The fine line between 'brave' and 'reckless': Amygdala reactivity and regulation predict recognition of risk." Neuroimage.

Mujica-Parodi, L. R., J. M. Carlson, J. Cha and D. Rubin (2014). "The fine line between 'brave' and 'reckless': Amygdala reactivity and regulation predict recognition of risk." Neuroimage **103C**: 1-9.

Mujica-Parodi, L. R., M. Korgaonkar, B. Ravindranath, T. Greenberg, D. Tomasi, M. Wagshul, B. Ardekani, D. Guilfoyle, S. Khan, Y. Zhong, K. Chon and D. Malaspina (2009). "Limbic dysregulation is associated with lowered heart rate variability and increased trait anxiety in healthy adults." Hum Brain Mapp **30**(1): 47-58.

Murphy, K., J. Bodurka and P. A. Bandettini (2007). "How long to scan? The relationship between fMRI temporal signal to noise ratio and necessary scan duration." Neuroimage **34**(2): 565-574.

Nakanishi, M., M. Chuma, S. Hige, T. Omatsu, H. Yokoo, K. Nakanishi, T. Kamiyama, K. Kubota, H. Haga, Y. Matsuno, Y. Onodera, M. Kato and M. Asaka (2011). "Relationship Between Diffusion-Weighted Magnetic Resonance Imaging and Histological Tumor Grading of Hepatocellular Carcinoma." Ann Surg Oncol.

Ochsner, K. N. and J. J. Gross (2005). "The cognitive control of emotion." Trends Cogn Sci **9**(5): 242-249.

Ochsner, K. N., J. A. Silvers and J. T. Buhle (2012). "Functional imaging studies of emotion regulation: a synthetic review and evolving model of the cognitive control of emotion." Ann N Y Acad Sci **1251**: E1-24.

Ogawa, S., T. M. Lee, A. R. Kay and D. W. Tank (1990). "Brain magnetic resonance imaging with contrast dependent on blood oxygenation." Proc Natl Acad Sci U S A **87**(24): 9868-9872.

Olsrud, J., A. Nilsson, P. Mannfolk, A. Waites and F. Stahlberg (2008). "A two-compartment gel phantom for optimization and quality assurance in clinical BOLD fMRI." Magn Reson Imaging **26**(2): 279-286.

Petryka, J., J. Misko, A. Przybylski, M. Spiewak, L. A. Malek, K. Werys, L. Mazurkiewicz, K. Gepner, P. Croisille, M. Demkow and W. Ruzyllo (2011). "Magnetic resonance imaging assessment of intraventricular dyssynchrony and delayed enhancement as predictors of response to cardiac resynchronization therapy in patients with heart failure of ischaemic and non-ischaemic etiologies." Eur J Radiol.

Power, J. D., K. A. Barnes, A. Z. Snyder, B. L. Schlaggar and S. E. Petersen (2012). "Spurious but systematic correlations in functional connectivity MRI networks arise from subject motion." Neuroimage **59**(3): 2142-2154.

Power, J. D., B. L. Schlaggar and S. E. Petersen (2015). "Recent progress and outstanding issues in motion correction in resting state fMRI." Neuroimage **105**: 536-551.

Qiu, Y., W. E. Kwok and J. P. Hornak (2014). "A method of switching the signal in an MRI phantom based on trace ion currents." J Magn Reson **245**: 171-176.

Radiology, A. C. o. (2005). "Phantom Test Guidance."

Radulescu, A. and L. R. Mujica-Parodi (2014). "Network connectivity modulates power spectrum scale invariance." Neuroimage **90**: 436-448.

Radulescu, A. R. and L. R. Mujica-Parodi (2009). "A principal component network analysis of prefrontal-limbic functional magnetic resonance imaging time series in schizophrenia patients and healthy controls." Psychiatry Res **174**(3): 184-194.

Raichle, M. E., A. M. MacLeod, A. Z. Snyder, W. J. Powers, D. A. Gusnard and G. L. Shulman (2001). "A default mode of brain function." Proc Natl Acad Sci U S A **98**(2): 676-682.

Raj, D., A. W. Anderson and J. C. Gore (2001). "Respiratory effects in human functional magnetic resonance imaging due to bulk susceptibility changes." Phys Med Biol **46**(12): 3331-3340.

Renvall, V. (2009). "Functional magnetic resonance imaging reference phantom." Magn Reson Imaging **27**(5): 701-708.

Renvall, V. and R. Hari (2009). "Transients may occur in functional magnetic resonance imaging without physiological basis." Proc Natl Acad Sci U S A **106**(48): 20510-20514.

Renvall, V., R. Joensuu and R. Hari (2006). "Functional phantom for fMRI: a feasibility study." Magn Reson Imaging **24**(3): 315-320.

Rheinheimer, S., B. Stieltjes, F. Schneider, D. Simon, S. Pahernik, H. U. Kauczor and P. Hallscheidt (2011). "Investigation of renal lesions by diffusion-weighted magnetic resonance imaging applying intravoxel incoherent motion-derived parameters-Initial experience." Eur J Radiol.

Rodd, J. M., I. S. Johnsrude and M. H. Davis (2012). "Dissociating frontotemporal contributions to semantic ambiguity resolution in spoken sentences." Cereb Cortex **22**(8): 1761-1773.

Rubin, D., T. Fekete and L. R. Mujica-Parodi (2013). "Optimizing complexity measures for FMRI data: algorithm, artifact, and sensitivity." PLoS One **8**(5): e63448.

Sagaspe, P., S. Schwartz and P. Vuilleumier (2011). "Fear and stop: a role for the amygdala in motor inhibition by emotional signals." Neuroimage **55**(4): 1825-1835.

Salvador, R., J. Suckling, M. R. Coleman, J. D. Pickard, D. Menon and E. Bullmore (2005). "Neurophysiological architecture of functional magnetic resonance images of human brain." Cereb Cortex **15**(9): 1332-1342.

Smith, S. M., C. F. Beckmann, J. Andersson, E. J. Auerbach, J. Bijsterbosch, G. Douaud, E. Duff, D. A. Feinberg, L. Griffanti, M. P. Harms, M. Kelly, T. Laumann, K. L. Miller, S. Moeller, S. Petersen, J. Power, G. Salimi-Khorshidi, A. Z. Snyder, A. T. Vu, M. W. Woolrich, J. Xu, E. Yacoub, K. Ugurbil, D. C. Van Essen, M. F. Glasser and W. U.-M. H. Consortium (2013). "Resting-state fMRI in the Human Connectome Project." Neuroimage **80**: 144-168.

Song, X. W., Z. Y. Dong, X. Y. Long, S. F. Li, X. N. Zuo, C. Z. Zhu, Y. He, C. G. Yan and Y. F. Zang (2011). "REST: a toolkit for resting-state functional magnetic resonance imaging data processing." PLoS One **6**(9): e25031.

Stoianovici, D., A. Patriciu, D. Petrisor, D. Mazilu and L. Kavoussi (2007). "A New Type of Motor: Pneumatic Step Motor." IEEE ASME Trans Mechatron **12**(1): 98-106.

Strawn, J. R., S. M. Bitter, W. A. Weber, W. J. Chu, R. M. Whitsel, C. Adler, M. A. Cerullo, J. Eliassen, S. M. Strakowski and M. P. DelBello (2012). "Neurocircuitry of generalized anxiety disorder in adolescents: a pilot functional neuroimaging and functional connectivity study." Depress Anxiety **29**(11): 939-947.

Thavendiranathan, P., S. Liu, S. Datta, M. Walls, A. Nitinunu, T. Van Houten, N. A. Tomson, L. Vidmar, B. Georgescu, Y. Wang, S. Srinivasan, N. De Michelis, S. V. Raman, T. Ryan and M.

A. Vannan (2011). "Automated Quantification of Mitral Inflow and Aortic Outflow Stroke Volumes by Three-Dimensional Real-Time Volume Color-Flow Doppler Transthoracic Echocardiography: Comparison with Pulsed-Wave Doppler and Cardiac Magnetic Resonance Imaging." J Am Soc Echocardiogr.

Tokuda, J., S. E. Song, G. S. Fischer, Iordachita, II, R. Seifabadi, N. B. Cho, K. Tuncali, G. Fichtinger, C. M. Tempany and N. Hata (2012). "Preclinical evaluation of an MRI-compatible pneumatic robot for angulated needle placement in transperineal prostate interventions." Int J Comput Assist Radiol Surg **7**(6): 949-957.

Tolkunov, D., D. Rubin and L. Mujica-Parodi (2010). "Power spectrum scale invariance quantifies limbic dysregulation in trait anxious adults using fMRI: adapting methods optimized for characterizing autonomic dysregulation to neural dynamic time series." Neuroimage **50**(1): 72-80.

Triantafyllou, C., R. D. Hoge, G. Krueger, C. J. Wiggins, A. Potthast, G. C. Wiggins and L. L. Wald (2005). "Comparison of physiological noise at 1.5 T, 3 T and 7 T and optimization of fMRI acquisition parameters." Neuroimage **26**(1): 243-250.

Triantafyllou, C., R. D. Hoge and L. L. Wald (2006). "Effect of spatial smoothing on physiological noise in high-resolution fMRI." Neuroimage **32**(2): 551-557.

Triantafyllou, C., J. R. Polimeni and L. L. Wald (2011). "Physiological noise and signal-to-noise ratio in fMRI with multi-channel array coils." Neuroimage **55**(2): 597-606.

Uludag, K., B. Muller-Bierl and K. Ugurbil (2009). "An integrative model for neuronal activity-induced signal changes for gradient and spin echo functional imaging." Neuroimage **48**(1): 150-165.

van den Heuvel, M. P., C. J. Stam, M. Boersma and H. E. Hulshoff Pol (2008). "Small-world and scale-free organization of voxel-based resting-state functional connectivity in the human brain." Neuroimage **43**(3): 528-539.

Van Dijk, K. R., M. R. Sabuncu and R. L. Buckner (2012). "The influence of head motion on intrinsic functional connectivity MRI." Neuroimage **59**(1): 431-438.

van Houdt, P. J., P. P. Ossenblok, P. A. Boon, F. S. Leijten, D. N. Velis, C. J. Stam and J. C. de Munck (2010). "Correction for pulse height variability reduces physiological noise in functional MRI when studying spontaneous brain activity." Hum Brain Mapp **31**(2): 311-325.

Vanderhasselt, M. A., S. Kuhn and R. De Raedt (2012). "'Put on your poker face': neural systems supporting the anticipation for expressive suppression and cognitive reappraisal." Soc Cogn Affect Neurosci.

Wald, L. L. (2012). "The future of acquisition speed, coverage, sensitivity, and resolution." Neuroimage **62**(2): 1221-1229.

Watson, D., K. Weber, J. S. Assenheimer, L. A. Clark, M. E. Strauss and R. A. McCormick (1995). "Testing a tripartite model: I. Evaluating the convergent and discriminant validity of anxiety and depression symptom scales." J Abnorm Psychol **104**(1): 3-14.

Weisskoff, R. M., J. R. Baker, J. W. Belliveau, T. L. Davis, K. K. Kwong, M. S. Cohen and B. R. Rosen (1993). Power Spectrum Analysis of Functionally-Weighted MR Data: What's in the Noise? Society of Magnetic Resonance in Medicine. New York, New York.

Welvaert, M. and Y. Rosseel (2012). "How ignoring physiological noise can bias the conclusions from fMRI simulation results." Journal of Neuroscience Methods **211**.

Welvaert, M. and Y. Rosseel (2013). "On the definition of signal-to-noise ratio and contrast-to-noise ratio for FMRI data." PLoS One **8**(11): e77089.

Westlye, L. T., A. Bjornebekk, H. Grydeland, A. M. Fjell and K. B. Walhovd (2011). "Linking an anxiety-related personality trait to brain white matter microstructure: diffusion tensor imaging and harm avoidance." Arch Gen Psychiatry **68**(4): 369-377.

Woolrich, M. W., B. D. Ripley, M. Brady and S. M. Smith (2001). "Temporal autocorrelation in univariate linear modeling of FMRI data." Neuroimage **14**(6): 1370-1386.

Wu, T., X. Long, Y. Zang, L. Wang, M. Hallett, K. Li and P. Chan (2009). "Regional homogeneity changes in patients with Parkinson's disease." Hum Brain Mapp **30**(5): 1502-1510.

Yan, L., Y. Zhuo, Y. Ye, S. X. Xie, J. An, G. K. Aguirre and J. Wang (2009). "Physiological origin of low-frequency drift in blood oxygen level dependent (BOLD) functional magnetic resonance imaging (fMRI)." Magn Reson Med **61**(4): 819-827.

Yendiki, A., P. Panneck, P. Srinivasan, A. Stevens, L. Zollei, J. Augustinack, R. Wang, D. Salat, S. Ehrlich, T. Behrens, S. Jbabdi, R. Gollub and B. Fischl (2011). "Automated probabilistic reconstruction of white-matter pathways in health and disease using an atlas of the underlying anatomy." Front Neuroinform **5**: 23.

Yu-Feng, Z., H. Yong, Z. Chao-Zhe, C. Qing-Jiu, S. Man-Qiu, L. Meng, T. Li-Xia, J. Tian-Zi and W. Yu-Feng (2007). "Altered baseline brain activity in children with ADHD revealed by resting-state functional MRI." Brain and Development **29**(2): 83-91.

Yuan, J. L., S. K. Wang, X. J. Guo and W. L. Hu (2011). "Acute infarct of the corpus callosum presenting as alien hand syndrome: evidence of diffusion weighted imaging and magnetic resonance angiography." BMC Neurol **11**(1): 142.

Yuan, R., X. Di, E. H. Kim, S. Barik, B. Rypma and B. B. Biswal (2013). "Regional homogeneity of resting-state fMRI contributes to both neurovascular and task activation variations." Magn Reson Imaging **31**(9): 1492-1500.

Zang, Y., T. Jiang, Y. Lu, Y. He and L. Tian (2004). "Regional homogeneity approach to fMRI data analysis." Neuroimage **22**(1): 394-400.

Zarahn, E., G. K. Aguirre and M. D'Esposito (1997). "Empirical analyses of BOLD fMRI statistics. I. Spatially unsmoothed data collected under null-hypothesis conditions." Neuroimage **5**(3): 179-197.

Zhao, Q., K. D. White, T. Conway, M. K. and B. Crosson (2006). Test-Retest Reliability of fMRI using SmartPhantom. Proceedings of the International Society of Magnetic Resonance in Medicine.